

THESIS FOR THE DEGREE OF DOCTOR OF PHILOSOPHY

Application of the Boundary Element Method to combustion noise and half-space problems

HAIKE BRICK

Department of Civil and Environmental Engineering
Division of Applied Acoustics, Vibroacoustic Group
CHALMERS UNIVERSITY OF TECHNOLOGY
Göteborg, Sweden, 2009

**Application of the Boundary Element Method to combustion noise and
half-space problems**

HAIKE BRICK

ISBN 978-91-7385-331-6

© HAIKE BRICK, 2009

Doktorsavhandlingar vid Chalmers tekniska högskola

Ny serie nr. 3012

ISSN 0346-718X

Department of Civil and Environmental Engineering

Division of Applied Acoustics, Vibroacoustic Group

Chalmers University of Technology

SE-412 96 Göteborg, Sweden

Telephone + 46 (0) 31-772 2200

Printed by

Chalmers Reproservice

Göteborg, Sweden, 2009

Application of the Boundary Element Method to combustion noise and half-space problems

HAIKE BRICK

Department of Civil and Environmental Engineering

Division of Applied Acoustics, Vibroacoustic Group

Chalmers University of Technology

Abstract

The Boundary-Element-Method (BEM) is a powerful and established tool in computational acoustics. This thesis aims at an enhancement of the method towards combustion noise and half-space problems.

First, it is directly coupled to an incompressible Large Eddy Simulation (LES) to calculate the sound radiation of open flames. Compared to other hybrid methods in this area, the coupling of an incompressible LES and BEM is a computationally efficient concept. The incompressible approach enormously reduces the complexity of the LES of the source domain, and the BEM requires only the solution of a boundary integral along a control surface around the source region to predict the sound field in the acoustic domain. The thesis provides a theoretical discussion on the general applicability of this approach. It is applied to calculate the sound power of two open jet flames, which was also experimentally determined. A good agreement between measurement and simulation could be obtained regarding one of the flames. Reasons for the strong deviations considering the other flame are identified and possible correction strategies are outlined.

Second, a specialised half-space BEM was developed to account for the presence of an infinite boundary plane in the acoustic domain. Half-space problems are of great importance in acoustics, since realistic problems are seldom located in the unbounded three-dimensional space. Often a flat ground, which is characterised by its acoustic impedance, confines the acoustical domain. The presence of an infinite plane and the associated additional discretisation effort weakens the advantages of the classical BEM. One possible remedy is to use a Green's function, which automatically satisfies the boundary condition at the plane. In this thesis several Green's functions are reviewed and tested for their applicability in a BEM formulation. The successful implementation of an appropriate Green's function is verified by several test cases. The horn effect of the tyre-road interface has been chosen as practical benchmark problem. The excellent agreement of the simulated and measured horn effect in case of a rigid plane as well as in case of a mineral wool layer validates the developed half-space BEM.

Keywords: Hybrid approach, Kirchhoff's surface, incompressible Large Eddy Simulation, impedance plane, Green's function, horn effect, tyre-road interface

List of publications

This thesis is based on the work contained in the following appended papers, referred to by Roman numerals in the text:

COMBUSTION NOISE

- Paper I** H. Brick, R. Piscoya, M. Ochmann & P. Költzsch, “Modelling of combustion noise with the Boundary Element Method and Equivalent Source Method.”, *Proc. of 33rd International Congress and Exposition on Noise Control—internoise 2004*, Prague, Czech Republic, Aug. 22–25, 2004.
- Paper II** F. Flemming, A. Nauert, A. Sadiki, J. Janicka, H. Brick, R. Piscoya, M. Ochmann & P. Költzsch, “A hybrid approach for the evaluation of the radiated noise from a turbulent non-premixed jet flame based on Large Eddy Simulation and Equivalent Source & Boundary Element Methods.”, *Proc. of the 12th International Congress on Sound and Vibration—ICSV12*, Lisbon, Portugal, July 11–14, 2005.
- Paper III** H. Brick, R. Piscoya, M. Ochmann & P. Költzsch, “Prediction of the Sound Radiated from Open Flames by Coupling a Large Eddy Simulation and a Kirchhoff-Method.”, *Proc. of the 4th EAA European Congress on Acoustics—Forum Acusticum*, Budapest, Hungary, Aug. 29–Sept. 2, 2005.
- Paper IV** R. Piscoya, H. Brick, M. Ochmann & P. Költzsch, “Equivalent source method and boundary element method for calculating combustion noise.”, *Acta Acustica united with Acustica*, 94(4):514–527, 2008.

HALF-SPACE

- Paper V** M. Ochmann & H. Brick, “Acoustical radiation and scattering above an impedance plane.”, In: S. Marburg, B. Nolte (editors): *Computational Acoustics of Noise Propagation in Fluids. Finite and Boundary Element Methods*. Chapter 17, 459–494, Springer-Verlag, Berlin, 2008.
- Paper VI** H. Brick & M. Ochmann, “A half-space BEM for the simulation of sound propagation above an impedance plane.”, *Proc. of Acoustics’08—Paris, France, June 29–July 04, 2008*.

The part of the work done by H. Brick in all Papers amounts from 50% to 90%.

Other publications

The following papers are not included in the thesis due to an overlap in content or a content going beyond the scope of this thesis:

- R. Piscoya, H. Brick & M. Ochmann, “Determination of the Far Field Sound Radiation from Flames Using the Dual Reciprocity Boundary Element Method.”, *Acta Acustica united with Acustica*, 95(3):448–460, 2009.
- R. Piscoya, H. Brick, M. Ochmann & P. Költzsch, “Modelling of the Sound Radiation from Flames by means of Acoustic Equivalent Sources.”, In: A. Schwarz, J. Janicka (editors): *Combustion Noise*. Chapter 4, 93–127, Springer-Verlag, Berlin, 2009.
- H. Brick & M. Ochmann, “Point-source-scattering from tyre-like structures above an impedance plane.”, *NAG/DAGA '09—International Conference on Acoustics*, Rotterdam, Netherlands, March 23–26, 2009.
- R. Piscoya, H. Brick, M. Ochmann & P. Költzsch, “Numerical aspects of the prediction of the far field radiation from flames using an integral method.”, *The 2nd International Conference on Jets, Wakes and Separated Flows—ICJWSF-2008*, Berlin, Germany, Sept. 16–19, 2008.
- H. Brick & M. Ochmann, “Entwicklung einer Halbraum-BEM zur Simulation der Schallausbreitung über einer Impedanzebene.”, *34. Jahrestagung für Akustik—DAGA '08*, pp. 587–588, Dresden, Germany, March 10–13, 2008.
- H. Brick, R. Piscoya, M. Ochmann & P. Költzsch, “Comparison of the sound radiation of open flames simulated by a hybrid approach using LES and ESM.”, *11. CEAS-ASC / AIAA-TAC Workshop on “Combustion Noise”*, Lisboa, Portugal, Sept. 27–28, 2007.
- W. Kropp & H. Brick, “Spatially varying interlayer stiffness.”, *33. Jahrestagung für Akustik—DAGA '07*, Stuttgart, Germany, March 19–22, 2007.
- H. Brick, R. Piscoya, M. Ochmann & P. Költzsch, “Berechnung der Schallabstrahlung von Flammen mit Diskretisierungsmethoden.”, *32. Jahrestagung für Akustik—DAGA '06*, Braunschweig, Germany, March 20–23, 2006.
- H. Brick, R. Piscoya, M. Ochmann & P. Költzsch, “A hybrid LES-BEM method for the calculation of combustion noise above an infinite plane.”, *The 6th*

European Conference on Noise Control—Euronoise 2006, Tampere, Finland, May 30–June 1, 2006.

- H. Brick, R. Piscoya, M. Ochmann & P. Költzsch, “Hybride LES/Kirchhoff-Methode zur Berechnung des Verbrennungsgeräusches von freien Flammen.”, *31. Jahrestagung für Akustik—DAGA '05*, München, Germany, March 14–17, 2005.
- R. Piscoya, H. Brick, M. Ochmann & P. Költzsch, “Numerical aspects of the equivalent source method applied to combustion noise.”, *12th International Congress on Sound and Vibration—ICSV12*, Lisbon, Portugal, July 11–14, 2005.
- H. Brick & M. Ochmann, “Eine BEM-Toolbox zur Berechnung der Schallabstrahlung schwingender Strukturen vor Hindernissen und über absorbierendem Boden.”, *29. Jahrestagung für Akustik—DAGA '03*, Aachen, Germany, March 18–20, 2003.
- H. Brick & M. Ochmann & E. Brenck, “Simulation of the sound radiation from wheel-like structures using the boundary element method.”, *The 3rd EAA European Congress on Acoustics—Forum Acusticum*, Sevilla, Spain, Sept. 16–20, 2002.

Acknowledgements

This thesis presents the major part of the research I have conducted since I started working in the field of computational acoustics several years ago. The first research project “Virtual optimisation of noise control measures” focussed on the effectiveness of noise barriers on impedance ground and was the basis for my way into the Boundary Element Method. Afterwards I participated in the combustion noise project “Modelling of the sound radiation from flames by means of acoustic equivalent sources”, which later incorporated the Boundary Element Method. Unfortunately I failed to focus my research on a single subject during the past few years, therefore both of these interesting research projects are included in the thesis. The Boundary Element Method links the two projects.

There are many people whom I have to thank. First of all I am indebted to my supervisor Martin Ochmann from the Beuth Hochschule für Technik Berlin. I much appreciate his profound knowledge in computational acoustics, especially BEM, and his unerring mathematical point of view. I am also grateful to Wolfgang Kropp from the Division of Applied Acoustics of the Chalmers University of Technology, Göteborg, who accepted me as an external Ph.D. student and often encouraged me with his valuable advice. I was also very fortunate to have the opportunity to work with Peter Költzsch as one of his last co-workers at the Technical University of Dresden before his retirement, and I am thankful for that brief, yet fruitful, collaboration. I am much obliged to my colleagues at the Beuth Hochschule für Technik for their support, and especially to Rafael Piscoya for the vast number of discussions and all the years of collective and effective work. Furthermore, I would like to extend my thanks to the students who have helped me with the development of the BemLab code, especially Elfriede Brenck, Christian Föllmer and Christian Steuck. The work included in this thesis was financially supported by the German Research Foundation DFG through the research group “Combustion Noise” FOR 486 and German Federal Ministry of Education and Research (BMBF), managed by the “Arbeitsgemeinschaft industrieller Forschungsvereinigungen ‘Otto von Guericke’ e. V.” (AiF).

A huge bunch of virtual flowers I give to Henk Jonas, who has patiently accompanied me through the ups and downs of research and family life and the combination of both. Finally, I must mention our two wonderful children, Hendrike and Hilbert, who gave me plenty of love and joy while I was doing my research work.

Haike Brick
Berlin, October 2009

Contents

1. Introduction	1
1.1. Thesis aim	1
1.2. Thesis structure	2
1.3. Overview of appended papers and additional thesis results	3
2. Boundary Element Method in acoustics	7
2.1. History and Applications	7
2.2. Governing equations	8
2.3. Numerical implementation	11
3. BEM for calculating combustion noise	15
3.1. Background	15
3.1.1. Introduction to combustion noise	15
3.1.2. Research group “Combustion Noise”	17
3.2. Object of study: turbulent, non-premixed jet flames	20
3.3. The hybrid approach	21
3.3.1. Coupling of BEM and LES: A discussion	22
3.3.2. Location of the Kirchhoff’s surface	26
3.3.3. Determination of an average sound power spectrum	27
3.3.4. Downsampling of the surface data	36
3.3.5. Input data correction	40
3.4. Application of the CHIEF method	53
3.4.1. The interior sound field of the cylinders	53
3.4.2. Testing CHIEF point positions	55
3.5. Inclusion of ground effects	58

4. Half-space BEM	61
4.1. The half-space Green's function	62
4.2. Green's functions in presence of an impedance plane	65
4.2.1. Literature review	65
4.2.2. Approximate solution	66
4.2.3. Exact solutions	67
4.2.4. Comparison of exact solutions	71
4.2.5. Limiting cases of a soft or rigid impedance plane	75
4.3. Discretised plane versus half-space BEM	77
4.4. Computation of the horn effect	80
4.4.1. Configuration	80
4.4.2. Tyre model	81
4.4.3. Numerical treatment of the horn geometry	84
4.4.4. Influence of the impedance plane	86
4.4.5. Validation of the model by measurement data	87
5. Conclusions and further work	91
5.1. Combustion noise	91
5.2. Half-space BEM	93
5.3. Future work	94
Bibliography	97
Appendices	
A. Interior sound field of a cylinder	107
B. Derivation of the sound intensity spectral density	111
C. Monopole source above an infinite plane	113
D. Gauss-Laguerre Quadrature	115

List of Figures

2.1. Domain definition.	10
3.1. Percentage of people annoyed by noise.	16
3.2. Position of project 4 within the research group “Combustion Noise”.	20
3.3. Principal sketch of a non-premixed, turbulent jet flame.	21
3.4. Hybrid approach for a) open flame; b) enclosed flame.	23
3.5. Density and temperature at different Kirchhoff’s surfaces, HD-flame.	27
3.6. Density and temperature at different Kirchhoff’s surfaces, H3-flame.	28
3.7. Measured and simulated sound power spectrum, HD-flame.	29
3.8. Generic boundary value problem.	31
3.9. Coherence of the two pressure signals of an intensity probe.	32
3.10. Average intensity spectra.	33
3.11. Average sound power spectra, H3-flame.	34
3.12. Coherence of the velocity data, H3-flame.	36
3.13. Velocity distribution in axial direction x at $t = 0.081s$	37
3.14. Velocity distribution in axial direction x at $t = 0.245s$	38
3.15. Velocity distribution in radial direction r at $t = 0.081s$	38
3.16. L_W : pointwise vs. filtered data sampling.	39
3.17. L_W : complete vs. downsampled data set.	39
3.18. L_W of the outflow cap: complete vs. downsampled data set.	40
3.19. Graphical depiction of the PCA of a matrix \mathbf{X}	41
3.20. Relative variance plot, test example.	43
3.21. Normal velocity $v_n^{j,k}$ at one node of the sphere.	44
3.22. Original and reconstructed correlated signal components.	45
3.23. Relative variance spectrum σ_k^2 of the test example data.	46
3.24. Relative variance plot, H3/HD-flame.	47
3.25. Complete relative variance spectra, H3/HD-flame.	47

3.26. L_W for different principal components, H3-flame and HD-flame. . .	48
3.27. Schematic sketch of the control surface enclosing the flame.	50
3.28. First interior modes of a cylinder.	54
3.29. Efficiency of several CHIEF point settings.	57
3.30. CHIEF point positions.	57
3.31. Real and image Kirchhoff's surface in presence of a reflecting plane.	58
3.32. Directivity of the sound field – HD-flame.	59
3.33. L_W of the HD-flame depending on the ground.	59
4.1. Geometry of the radiation and scattering problem in a half-space. . .	62
4.2. Notation in the half-space setting.	64
4.3. Condition for the Weyl-van der Pol formula.	67
4.4. Sound field above an impedance plane.	73
4.5. Sound field close to an impedance plane.	74
4.6. Simulation error depending on the size of the elements.	78
4.7. Simulation error with or without symmetry plane.	78
4.8. Sound pressure level at the field points.	79
4.9. Position of tyre, source and field point in the half-space setting. . .	80
4.10. Horn geometry and dimensioning.	81
4.11. Cross section of the square and rounded tyre model.	82
4.12. Maximum frequency of the surface elements of the tyre.	82
4.13. Dependence of ΔL_H on the setup parameters.	83
4.14. Sound pressure on the refined surface mesh.	84
4.15. Sound pressure at the surface mesh of the tyre.	85
4.16. ΔL_H depending on the integration technique.	85
4.17. ΔL_H at different receiver positions.	86
4.18. Frequency response of Z_p and N_{laguerre}	87
4.19. ΔL_H depending on the impedance of the plane.	88
4.20. Comparison of calculated and measured ΔL_H	89
4.21. Comparison of calculated and measured ΔL_H , setup b.	89
A.1. Geometry of a cylinder.	107
C.1. Geometry of a monopole source above a plane S_p	113
D.1. Checksum for the zeros of the Laguerre polynomials.	116

List of Tables

4.1. Measurement parameters, sound field above impedance plane.	71
4.2. Setup parameters for discretised plane models.	77
4.3. Setup parameters, tyre above impedance plane.	81
4.4. Measurement parameters, horn effect above impedance plane.	88
A.1. First zeros χ_{mi} of the Bessel function $J_m(x)$	109
A.2. Cut-on frequencies f_{mi} of the 10. Kirchhoff's surface – HD-flame. .	109
D.1. Zeros and weights of the Laguerre polynomials.	120

List of Symbols

δ	Dirac delta function		
γ	$j k_0/Z_p$ [m^{-1}]	j	imaginary unit
γ_{xy}	coherence	$\Im\{\}$	imaginary part
ω	angular frequency = $2\pi f$ [Hz]	$\Re\{\}$	real part
ϕ	polar angle [rad], velocity potential [m^2s^{-1}]		
π	3.1415927...	c_0	sound speed in Ω [m/s]
ρ	density [kg/m^3], horizontal distance [m]	e	2.7183...
ρ_0	density in $\Omega = 1.21 kg/m^3$	f	frequency [Hz]
σ	standard deviation	$g(\vec{x}, \vec{y})$	Green's function
σ^2	variance	i, j	indices, $i, j \in \mathbb{N}$
θ_0	angle [rad]	k, l	indices, $k, l \in \mathbb{N}$
$\varphi(\vec{x})$	source function	k_0	wavenumber in $\Omega = \omega/c_0$ [m^{-1}]
ξ_1, ξ_2	local coordinates at S [m]	m, n	indices, $m, n \in \mathbb{N}$
G_{xy}	cross-spectrum	p	sound pressure [Pa]
Y_p	normalised admittance = $1/Z_p$	p_0	reference value = $2 \cdot 10^{-5}$ Pa
Γ	Gamma function	r	distance [m]
Ω	acoustic domain, $\Omega \subset V$	t	time [s]
		v_n	normal velocity [m/s]
		w	weight factors for Gaussian integration
G	matrix of the single layer	x, y, z	cartesian coordinates [m]
H	matrix of the double layer	z'	dummy variable of integration
I_N	identity matrix of size N	$N(\vec{x}, \sigma^2)$	normal distribution
p	p at the collocation points (vector)	A_{src}	source strength [N/m]
v	v_n at the collocation points (vector)	E	error
		H_0	Hankel function

J	Jacobian determinant	$\langle \tilde{f}(t) \rangle$	time average of $\tilde{f}(t)$
$J_m(x)$	Bessel function	∇	gradient
L	length [m]	∇^2	Laplacian = $\sum_{i=1}^3 \partial^2 / \partial x_i^2$
$L[\]$	differential operator	\bar{x}	expected value of a random variable x
$L_n^{(\alpha)}$	Laguerre polynomials	\tilde{f}	time-domain function
L_p	sound pressure level [dB]	$\vec{x} \cdot \vec{y}$	dot product of \vec{x} and \vec{y}
L_W	sound power level [dB]	*	complex conjugate
Ma	Mach number	$f'(x)$	$\partial f(x) / \partial x$
N, M	numbers, $N, M \in \mathbb{N}$	$n!$	faculty of n , $n \in \mathbb{N}$
P_W	sound power [W]	$ x $	modulus = $\sqrt{xx^*}$
R_{eff}	effective flow resistivity [kPa s/m ²]	$ \vec{x} $	Euclidian norm of \vec{x}
R_p	reflection coefficient	\vec{n}	normal vector
Re	Reynold's number	\vec{u}	velocity vector [m/s]
S	surface	\vec{v}	velocity vector [m/s]
T	temperature [K], time interval [s]	\vec{x}	observation point, $\vec{x} = (x, y, z) \in V$
V	vector space \mathbb{R}^3	\vec{y}	source point, $\vec{y} = (x_s, y_s, z_s) \in V$
Z	impedance [Ns/m ³]	\vec{I}	sound intensity [Wm ⁻²], intensity spectral density [Wm ⁻² Hz ⁻¹]
Z_p	normalised impedance = $Z / (\rho_0 c_0)$		
$\hat{f}(\omega)$	transfer function		

Chapter 1

Introduction

1.1. Thesis aim

With the increasing capability of computers, especially personal computers, numerical solutions for a wide range of engineering problems become more and more important and available. They are desired as prediction tools, which should replace the prototyping process.

The Boundary Element Method (BEM) is one of the numerical methods applied in the field of computational acoustics. It is a well established technique to solve academic as well as industrial acoustic radiation and scattering problems. Unlike the Finite Element Method (FEM), it only requires a discretisation of the boundary of the acoustic domain, which makes it very practical and easy to build the simulation model. On the other hand the resulting matrices are fully populated and asymmetric, which limits the size of the models that can be analysed. For many standard problems, commercial codes are available, such as Virtual.Lab [1], VNoise [2] and FastBEM Acoustics [3]. But nevertheless, development is still in progress as the agile participation of researchers in recent conferences and the high number of currently published papers on this topic show. The main focus lays on coupling strategies to other numerical methods, fluid-structure interaction, time domain formulations, inverse boundary element techniques and eigenvalue analysis. Much effort is invested in reducing the computational complexity by fast solution techniques, e.g. Fast Multipole Method (FMM), and the development of specialised approaches, e.g. half-space formulations.

The thesis is devoted to two of the current research needs in BEM. First, it deals with the coupling of the BEM to another numerical method, namely

to an incompressible Large Eddy Simulation (LES), for the calculation of the sound radiation of open, turbulent, non-premixed jet flames. For this hybrid approach a direct BEM formulation is used, where the boundary conditions are prescribed by the velocity data computed by the LES. Such hybrid approaches take advantages of the highly specialised and elaborated techniques, which are available for different governing processes in different domains. The coupling of the methods is a very sensible step, which is crucial for the accuracy and reliability of the complete hybrid approach. The combination of incompressible LES and BEM is a comparatively less expensive approach for the determination of the noise emission from flames. It is interesting to see that it is possible to obtain a good sound field prediction by this coupling strategy, but it is also important to identify error sources and the scope of validity of the method. The thesis aims for a clarification of the influence of the coupling parameters on the accuracy of the overall results as well as for an investigation of possible input data correction techniques.

Second, the thesis addresses the reduction of the computational complexity by implementing an appropriate half-space formulation into a direct BEM code to model the sound propagation above an impedance plane. Outdoor sound propagation depends strongly on the acoustic characteristics of the ground. The effect of a fully reflective, rigid ground on the sound field can be easily modelled by a BEM model. The modelling of the effect of a ground of finite impedance like grassland or open porous asphalt is a much more complex, but necessary task. For example, the design of low-noise road surfaces needs an accurate prediction of the influence of the non-rigid road surface on the overall rolling noise. In the thesis several half-space formulations are reviewed and tested for the use within the BEM, the implementation of an appropriate formulation into a BEM code is discussed and the accurate prediction of the horn effect of the tyre-road interface is presented. Considering this second aspect, the thesis contributes to the development of effective simulation tools for outdoor sound propagation.

1.2. Thesis structure

The thesis is devoted to the use of the BEM for the simulation of sound radiation and scattering problems in different research fields. Therefore this introduction is followed by a review of the BEM. The chapter “*Boundary Element Method in acoustics*” includes an overview of the history of the BEM in the field of computational acoustics, the derivation of the governing equation and the presentation of its numerical implementation.

The third chapter “*BEM for calculating combustion noise*” is related to the combustion noise project, i.e. to the coupling of BEM and LES to calculate the sound radiation of turbulent flames. In Section 3.1 the combustion noise problem is briefly introduced and the research project and its integration in the German research group “Combustion Noise” is presented. The objects of the study—open, turbulent, non-premixed jet flames—are introduced in Section 3.2. Section 3.3 starts with a theoretical discussion on the validity of the present hybrid approach. It continues with an analysis of several coupling parameters and their influence on the accuracy of the approach, such as the location of the coupling interface, the downsampling of the LES data, and the determination of an average sound power spectrum. Emphasis is placed in Section 3.3.5 on the correction of the input data for the BEM by a Principal Component Analysis of the velocity data and a splitting technique, that is based on the Helmholtz theorem. Section 3.4 describes the application of the CHIEF method—a regularisation method relating to the non-uniqueness problem of the BEM—to the present flame model. In Section 3.5 the influence of a rigid and soft ground on the sound radiation of the flames is studied. The theme of that last section is explored further in the next chapter.

In the fourth Chapter “*Half-space BEM*” the expansion of a direct BEM to half-space problems with an infinite impedance plane is presented. The available half-space Green’s functions are surveyed in sections 4.1 and 4.2. In Section 4.3 the accuracy and performance of the developed half-space BEM formulation is compared with a classical discretisation of a portion of the impedance plane. Finally, in Section 4.4 the half-space BEM is successfully applied to the simulation of the horn effect of the tyre–road interface for a rigid as well as for a soft impedance of the road surface.

The thesis is completed in Chapter 5 by conclusions and ideas for further research.

1.3. Overview of appended papers and additional thesis results

Combustion Noise

All papers relating to the combustion noise project address the coupling of the BEM to an incompressible LES to compute the sound radiation of turbulent, non-premixed jet flames. As a whole they represent the progress of the research project, while each paper focuses on a special topic. Beside the BEM, most papers include also the application of the Equivalent Source Method (ESM) to the combustion noise problem, which was the subject of my colleague’s work.

Paper I is the first publication on the topic of the thesis. It deals mainly with the influence of the artificial turbulence of the LES on the sound field. The artificial turbulence is an inflow boundary condition of the LES to generate enough turbulence in the low-Mach number flow. This boundary condition highly disturbs the acoustic simulation. It can be remedied by setting the velocity data at the inflow disc of the Kirchhoff's surface to zero.

Paper II is a joint paper with our cooperation partners at the Technical University Darmstadt, who provided the LES data. In this paper an overview of the applied LES can be found as well as a validation of the flow field simulation. The acoustic simulation and its validation are also included in the paper, but they are described much more in detail in Paper III.

Paper III emphasis the acoustic part of the coupling strategy BEM-LES. The paper includes the description of the sound power measurements of the isothermal and reactive flow. The noise level due to the combustion processes in the reactive flow exceeds the pure flow noise level of the isothermal flow many times over. An interesting detail is the study on the influence of the Reynolds number Re on the sound radiation of one of the flames. The normalisation of the measured sound power level to Re^4 reveals the strong correspondence of the flame with an aerodynamic monopole source.

Paper IV is the concluding journal paper of the combustion noise project regarding the coupling of the BEM and ESM with a LES. The paper covers many aspects of the pre-processing of the LES data and meshes for the use within BEM and ESM. The input velocity data are analysed and the validation of the results of the BEM and ESM simulations by the measurement data is discussed in detail.

Half-Space

Paper V is a comprehensive publication about the half-space BEM. The first part of the paper is mainly a contribution of Martin Ochmann. It presents the full derivation of the appropriate half-space Green's function, which was later implemented in the BEM. The second part deals with the numerical point of view. The implementation of two Green's function into the BEM code BEMLAB is discussed along with a study of the numerical properties of the Green's functions and their derivatives. Applied quadrature techniques are presented. Several academic test case verify the accuracy of the developed half-space BEM.

Paper VI includes a further test case, which is employed to investigate the accuracy and performance of the half-space BEM in comparison to the use of a discretised portion of the infinite plane within an indirect BEM. It can be shown that the quality of the half-space BEM solution is much higher than that of the comparable indirect BEM model, while the costs depend strongly on the characteristics of the impedance plane.

Additional thesis work

The thesis also presents the results of preliminary and additional studies, which were not published in the Papers.

Concerning the Combustion Noise theme, the hybrid approach, which is presented in Paper I–IV, is supported by a theoretical discussion on its validity. Some additional aspects of the hybrid approach are thoroughly studied, such as the determination of a mean sound power spectrum, the influence of the spatial downsampling of the LES data on the simulation results, and possibilities for an input data correction. The CHIEF method was closely examined before its application to the flame model, and the results of this study are presented.

The Papers V–VI on the half-space problem are completed by a detailed review on the available Green's functions for sound propagation above an impedance plane. Approximate as well as exact solutions are presented along with a discussion on their applicability within a direct BEM formulation. The calculation of the horn effect of the tyre–road interface represents an advanced benchmark problem for the developed half-space BEM. The computation details and the results are given, which successfully validate the extension of the classical BEM to half-spaces with finite impedance boundary conditions.

Chapter 2

Boundary Element Method in acoustics

The Boundary Element Method (BEM) is a numerical technique for solving various types of partial differential equations that describe physical phenomena in engineering, such as fluid mechanics, electromagnetics, fracture mechanics, elastomechanics, and acoustics. The governing differential equations are formulated as integral equations along the domain boundaries. By means of the BEM, the field parameters at the boundaries are found, which fit the given boundary conditions. A constraint of the method is the availability of an appropriate Green's function for the given initial and boundary value problem.

2.1. History and Applications

The first publications on BEM have been made around forty years ago. A historical review on the development and use of the Boundary Element Method is given in [4–6], a comprehensive bibliography can be found at [7]. The corner stones of the method are certainly the works of Fredholm [8] and correlated works on integral equations in mathematical physics. The numerical implementation of Fredholm type of integral equations started in 1960s in fields of research, which involved infinite domains, such as potential theory [9, 10] and acoustics, especially concerning scattering problems in underwater acoustics [11, 12]. These initial works were soon followed by an increasing number of publications in different research fields, also on the application of boundary integral equations to acoustic radiation problems [13, 14]. In this time, the term boundary element method was not used, but the applied theoretical and numerical scheme complies with what was later called this way. In the following a lot of research work

was done and numerous papers contributed to the development of an efficient and universal boundary integral formulation of the Helmholtz-Integral equation, e.g. [15–22]. Probably, the term “Boundary Element Method” has been established by the First International Conference on Boundary Element Methods in Engineering in 1978 [23]. It can be noticed, that from that time onward this term is also used in the field of acoustics. Up to now the BEM has become an integral part of computational acoustics and an widely-used engineering tool for the prediction of radiated and scattered sound fields in an homogeneous medium. Textbooks have been published, which focus on the theoretical background and the implementation of the BEM in acoustics as [6, 24–26]. Few commercial codes are available, which covers the most standard problems, such as Sysnoise in Virtual.Lab [1], VNoise [2] and FastBEM Acoustics [3].

Meanwhile, the BEM has been applied to a variety of acoustic problems. The classical application area is the solution of sound radiation and scattering problems in the frequency domain for exterior as well as for interior problems, cf. examples at [1–3]. The Fast Multipole Method [27] is a comparatively young technique, which allows the use of huge BEM models and makes the BEM even more attractive in this area. Whereas the BEM in the frequency domain yields the solution for stationary problems, the BEM in the time domain is well suited for the analysis of transient processes [24, Ch. 8], [26, Ch. 18]. Other applications areas are the eigenvalue analysis [6], the inverse BEM for sound source identification [26, Ch. 20] and the multi-domain BEM to solve problems with two or more acoustic media [26, Ch. 13]. The solution of coupled field problems by a coupling of BEM with other numerical methods is another very active research field [25, Ch. 11-13], [26, Ch. 19], [28].

2.2. Governing equations

The derivation of the Helmholtz-Integral equation, which forms the basis of the acoustic BEM, is strongly connected with the concept of Green’s functions. The presented derivation is based on the mathematical fundamentals in [29, Ch. 5].

The governing equation for the propagation of sound waves in an homogeneous medium at rest is the Helmholtz equation

$$L[p] = \nabla^2 p(\vec{x}) + k_0^2 p(\vec{x}) = -\varphi(\vec{x}) \quad (2.1)$$

where $L[\]$ denotes the differential operator. $p(\vec{x})$ is the sound pressure at the spatial point $\vec{x} = (x, y, z)$, which lies in the domain Ω . ∇^2 is the Laplacian operator,

$k_0 = \omega/c_0$ is the wavenumber with $\omega = 2\pi f$, f is the frequency and c_0 the speed of sound in the acoustic domain. $\varphi(\vec{x})$ represents a spatially distributed source function due to harmonic acoustic sources in Ω . The harmonic time dependence of the sound pressure is assumed as $\tilde{p}(\vec{x}, t) = p(\vec{x})e^{j\omega t}$. The Green's function $g(\vec{x}, \vec{y})$ of $L[p(\vec{x})]$ is defined by the expression

$$L[g] = \nabla^2 g(\vec{x}, \vec{y}) + k_0^2 g(\vec{x}, \vec{y}) = -\delta(\vec{x} - \vec{y}), \quad (2.2)$$

with $\delta(\vec{x} - \vec{y})$ as Dirac delta function, i.e. the Green's function $g(\vec{x}, \vec{y})$ is the solution for a point source at $\vec{y} = (x_s, y_s, z_s)$. Additionally, $p(\vec{x})$ is given by

$$p(\vec{x}) = \int_{\Omega} g(\vec{x}, \vec{y}) \varphi(\vec{y}) dx_s dy_s dz_s. \quad (2.3)$$

The Green's function for the unbounded three-dimensional space, which fulfils Eqs. (2.2) and (2.3) is

$$g(\vec{x}, \vec{y}) = \frac{e^{-jk_0 r}}{4\pi r} \quad (2.4)$$

with $r = \|\vec{x} - \vec{y}\| = \sqrt{(x - x_s)^2 + (y - y_s)^2 + (z - z_s)^2}$ representing the distance between \vec{x} and \vec{y} . Also, solution (2.4) fulfils Sommerfeld's radiation condition [30]

$$\lim_{r \rightarrow \infty} r \left(\partial \frac{g(\vec{x}, \vec{y})}{\partial r} - j k_0 g(\vec{x}, \vec{y}) \right) = 0, \quad (2.5)$$

which ensures that Eq. (2.4) represents a sound source and not a sound sink.

Since L is linear and self-adjoint, Green's second theorem can be applied to Eqs. (2.1) and (2.2)

$$\begin{aligned} & \int_{\Omega} \left(L[p(\vec{y})]g(\vec{x}, \vec{y}) - L[g(\vec{x}, \vec{y})]p(\vec{y}) \right) dx_s dy_s dz_s \\ & = \int_S \left(p(\vec{y}) \frac{\partial g(\vec{x}, \vec{y})}{\partial \vec{n}_y} - g(\vec{x}, \vec{y}) \frac{\partial p(\vec{y})}{\partial \vec{n}_y} \right) dS_y, \end{aligned} \quad (2.6)$$

where $\partial p(\vec{y})/\partial n_y$ is the directional derivative of $p(\vec{y})$ in the direction of the inward pointing normal vector \vec{n}_y at the surface interval dS_y . The boundary S has to be piecewise smooth and must enclose the acoustic domain entirely. Fig. 2.1 illustrates the definition of the S , \vec{n}_y and Ω . The boundary S divides the unbounded three-dimensional space V in two complementary domains, the exterior domain Ω_e and the interior domain Ω_i . The acoustic domain Ω in Eq. (2.6) is either $\Omega_e \cup S$ or $\Omega_i \cup S$, i.e. the boundary belongs to the domain of interest. The choice is done by the definition of the normal direction at S . In the

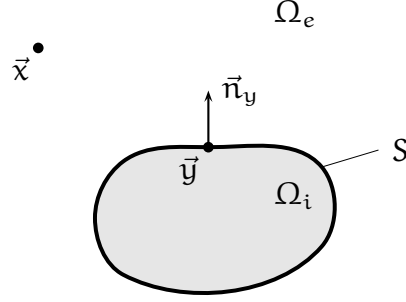


Figure 2.1.: Definition of the domain Ω_e and Ω_i , the domain boundary S and the normal vector \vec{n}_y for an exterior problem.

context of this work, an inward pointing normal vector is defined as to point into the acoustic domain. The radiation and scattering problems, which are examined in this thesis, are exterior problems. Thus, \vec{n}_y points into Ω_e as shown in Fig. 2.1 and $\Omega = \Omega_e \cup S$.

The first volume integral term at the left hand side of Eq. (2.6) represents the effect of the acoustic sources, which are distributed in Ω_e , at the point \vec{x} , i.e. it represents the incident sound field $p_{\text{inc}}(\vec{x})$,

$$p_{\text{inc}}(\vec{x}) = \int_{\Omega} \varphi(\vec{y}) g(\vec{x}, \vec{y}) dx_s dy_s dz_s. \quad (2.7)$$

where $\vec{y} \in \Omega$, but $\vec{x} \in V$. The evaluation of the second volume integral depends on the location of \vec{x} . Assuming \vec{x} is in Ω , but not at S , the integral yields

$$\int_{\Omega} L[g(\vec{x}, \vec{y})] p(\vec{y}) dx_s dy_s dz_s = p(\vec{x}), \quad \vec{x} \in \Omega_e. \quad (2.8)$$

since $L[g(\vec{x}, \vec{y})] = \delta(\vec{x} - \vec{y})$. Assuming \vec{x} is in Ω_i , the integral becomes

$$\int_{\Omega} L[g(\vec{x}, \vec{y})] p(\vec{y}) dx_s dy_s dz_s = 0, \quad \vec{x} \in \Omega_i, \quad (2.9)$$

since $L[g(\vec{x}, \vec{y})] = 0$ everywhere except $\vec{y} = \vec{x}$ and \vec{x} is not included in the integration domain. If \vec{x} on S , the singularity of $\delta(\vec{x} - \vec{y})$ is shifted to the integration boundary and such an integral is not defined. In order to remedy this ambiguity, the point \vec{x} is excluded from Ω_e by a tiny volume Ω_ϵ of radius ϵ around \vec{x} . The surface S_ϵ , which encloses Ω_ϵ , becomes an additional part of the domain

boundary. With that, Eq. (2.6) becomes

$$\begin{aligned} \int_{\Omega \setminus \Omega_\varepsilon} L[g(\vec{x}, \vec{y})]p(\vec{y}) \, dx_s \, dy_s \, dz_s &= 0 \\ &= \int_{S \cup S_\varepsilon} \left(p(\vec{y}) \frac{\partial g(\vec{x}, \vec{y})}{\partial \vec{n}_y} - g(\vec{x}, \vec{y}) \frac{\partial p(\vec{y})}{\partial \vec{n}_y} \right) dS_y + p_{\text{inc}}(\vec{x}). \end{aligned} \quad (2.10)$$

It can be shown [31, Ch. 2.12], that the limiting process $\varepsilon \rightarrow 0$ on a smooth surface yields

$$\lim_{\varepsilon \rightarrow 0} \int_{S_\varepsilon} \left(p(\vec{y}) \frac{\partial g(\vec{x}, \vec{y})}{\partial \vec{n}_y} - g(\vec{x}, \vec{y}) \frac{\partial p(\vec{y})}{\partial \vec{n}_y} \right) dS_y = -\frac{1}{2}p(\vec{x}). \quad (2.11)$$

If point \vec{x} is located in a non-smooth area of S like a corner, the limiting process leads to different coefficients of $p(\vec{x})$ due to different solid angles around \vec{x} [20]. Taking the case differentiation with respect to the position of \vec{x} into account and using the relation of normal velocity and pressure

$$v_n(\vec{x}) = -\frac{1}{j \omega \rho_0} \frac{\partial p(\vec{x})}{\partial \vec{n}_x}, \quad (2.12)$$

Eq. (2.6) yields the Helmholtz-Integral-Equation (HIE) for exterior problems, which is the basis for the BEM

$$C(\vec{x})p(\vec{x}) = - \int_S \left(p(\vec{y}) \frac{\partial g(\vec{x}, \vec{y})}{\partial \vec{n}_y} + j \omega \rho_0 v_n(\vec{y}) g(\vec{x}, \vec{y}) \right) dS_y + p_{\text{inc}}(\vec{x}) \quad (2.13)$$

with

$$C(\vec{x}) = \begin{cases} 1 & \vec{x} \text{ in the exterior domain } \Omega_e, \\ \frac{1}{2} & \vec{x} \text{ on the surface } S, \\ 0 & \vec{x} \text{ in the interior domain } \Omega_i. \end{cases} \quad (2.14)$$

2.3. Numerical implementation

For the numerical approach, the surface S is discretised into N surface elements. During a collocation process, the point \vec{x}_m , $m = 1, \dots, N$, is placed subsequently at the centres of the elements returning N equations in the form of Eq. (2.15) with $C(\vec{x}_m) = 1/2$,

$$\begin{aligned} \frac{1}{2}p(\vec{x}_m) &= \sum_{j=1}^N \int_{S_j} \left(p(\vec{y}) \frac{\partial g(\vec{x}_m, \vec{y})}{\partial \vec{n}_y} + j \omega \rho_0 v_n(\vec{y}) g(\vec{x}_m, \vec{y}) \right) dS_y \\ &\quad + p_{\text{inc}}(\vec{x}_m). \end{aligned} \quad (2.15)$$

In order to evaluate the integral on the surface intervals S_j a planar master element is introduced, which is fully described by its coordinates ξ_1 and ξ_2 with $-1 \leq \xi_1, \xi_2 \leq 1$. The real surface element is mapped onto a master element by linear shape functions $N_i(\xi_1, \xi_2)$. In [24, Ch. 4] the mapping is described in detail and shape functions for quadrilateral and triangular elements are listed. When using isoparametric elements the distribution of the boundary values p and v_n on S_j is described by the same shape functions as the geometry. After substituting ξ_1 and ξ_2 into Eq. (2.15), the integration is done along the surface of the master element and can be rewritten as

$$\begin{aligned} \int_{S_j} [\dots] dS_y &= \int_{-1}^1 \int_{-1}^1 \frac{\partial g(\vec{x}_m, \vec{y}_j(\xi_1, \xi_2))}{\partial \vec{n}_{y_j}} \underbrace{\sum_{i=1}^{n_j} p_i^j N_i(\xi_1, \xi_2)}_{p(\vec{y}_j(\xi_1, \xi_2))} J_j d\xi_1 d\xi_2 \\ &+ \int_{-1}^1 \int_{-1}^1 j \omega \rho_0 g(\vec{x}_m, \vec{y}_j(\xi_1, \xi_2)) \underbrace{\sum_{i=1}^{n_j} v_{n,i}^j N_i(\xi_1, \xi_2)}_{v_n(\vec{y}_j(\xi_1, \xi_2))} J_j d\xi_1 d\xi_2 \end{aligned} \quad (2.16)$$

n_j denotes the number of element vertices, i.e. $n_j = 3$ for triangular, $n_j = 4$ for quadrilateral elements. p_i^j and $v_{n,i}^j$ identify the boundary data at the i -th vertex of the j -th element. The Jacobian determinant J_j accommodates the difference of the domain dimensions due to the stretching of the original element. Usually, for ξ_1 and ξ_2 the roots of Legendre polynomials are chosen and the Gauss-Legendre quadrature [32, Eq. 25.4.29] is applied to evaluate the integrals in Eq. (2.16). Thereby, Eq. (2.16) becomes

$$\begin{aligned} \int_{S_j} [\dots] dS_y &= \sum_{k=1}^L \sum_{l=1}^L w_k w_l f_1(\xi_1^k, \xi_2^l) p(\vec{y}_j(\xi_1^k, \xi_2^l)) \\ &+ w_k w_l f_2(\xi_1^k, \xi_2^l) v_n(\vec{y}_j(\xi_1^k, \xi_2^l)) \end{aligned} \quad (2.17)$$

with

$$f_1 = \frac{\partial g(\vec{x}_m, \vec{y}_j(\xi_1^k, \xi_2^l))}{\partial \vec{n}_{y_j}} J_j, \quad (2.18)$$

$$f_2 = j \omega \rho_0 g(\vec{x}_m, \vec{y}_j(\xi_1^k, \xi_2^l)) J_j. \quad (2.19)$$

L is the total number of Gaussian points ξ^k and ξ^l , and w are the associated weights [32, Tab. 25.4]. The one point integration applied in BEMLAB is obtained by choosing $L = 1$ with $\vec{y}_j = \vec{y}_j(0, 0)$ as the centre of the j -th element and

$w^2 J_j = \Delta S_j$. By an additional use of constant elements, i.e. the boundary data are constant on the surface of the elements ($v_{n,i}^j = v_n^j \forall i \in \{1, \dots, n_j\}$), Eq. (2.16) reduces to

$$C(\vec{x}_m)p(\vec{x}_m) = \sum_{j=1}^N \left(p(\vec{y}_j) \frac{\partial g(\vec{x}_m, \vec{y}_j)}{\partial \vec{n}_{y_j}} + j \omega \rho_0 v_n(\vec{y}_j) g(\vec{x}_m, \vec{y}_j) \right) \Delta S_j + p_{\text{inc}}(\vec{x}_m). \quad (2.20)$$

Eq. (2.20) represents a rather rough but very fast evaluation of Eq. (2.15). It yields very good results as long as the surface discretisation is sufficiently fine, usually following the six-elements-per-wavelength rule. This approach is applied throughout the presented work. Considering constant elements, a continuity of sound pressure and velocity is not required at the interfaces of the elements, i.e. for one and the same vertex different values of p and v_n are allowed, depending on its element affiliation. Comparisons of the performance of constant (discontinuous) and continuous elements within a BEM formulation have shown, that constant elements perform more efficiently than continuous ones if the nodal points \vec{y}_j (ξ_1^k, ξ_2^l) are chosen to be the zeros of the Legendre polynomials as done in Eq. (2.17) [33, 34]. Another clear advantage of using constant elements is that they are well suited for an adaptive mesh refinement as implemented in Section 4.4.3. A Gauss-Legendre quadrature, Eq. (2.17), using $L > 1$ Gaussian points is applied in Section 4.4 of this thesis to evaluate the surface integrals on selected elements, which are very close to collocation points x_m due to the special model geometry. In this context an adapted integration technique is utilised with a further subdivision of S_j into smaller surface intervals S_{jk} . The Gauss-Legendre quadrature is then applied to the subintervals S_{jk} .

During the collocation process, the point x_m is placed at the centres of the surface elements. The choice of $L = 1$ but also of any other odd number leads to a singularity of the integrand in Eq. (2.20) or f_1, f_2 in Eq. (2.17) for $m = j$. Considering constant elements, the singularity can be easily resolved as described in Section 17.3.1 of Paper V, Eq. (17.65).

The resulting matrix equation for $p(\vec{x})$ reads

$$\mathbf{C}\mathbf{p} = \mathbf{H}\mathbf{p} + j \omega \rho_0 \mathbf{G}\mathbf{v} + \mathbf{p}_{\text{inc}}, \quad (2.21)$$

in which \mathbf{p} and \mathbf{v} are the pressure and normal velocity at the surface elements. The matrices \mathbf{H} and \mathbf{G} contain the kernel functions $\partial g(\vec{x}, \vec{y})/\partial \vec{n}_y$ and $g(\vec{x}, \vec{y})$ and $\mathbf{C} = 1/2 \mathbf{I}_N$ with \mathbf{I}_N as identity matrix.

The final set of equations depends on the boundary conditions. For a well-posed problem, only half of the boundary values are given as boundary conditions. In

case of Neumann boundary conditions, the normal velocity v_n is prescribed on the surface S , in case of Dirichlet boundary conditions the pressure p is prescribed at S . General or Robin boundary conditions are given by equation

$$\alpha p(\vec{x}) + \beta v_n(\vec{x}) = \zeta, \quad \vec{x} \in S. \quad (2.22)$$

Generally, the type of boundary condition can vary from element to element. After sorting the unknown and known parts of Eq. (2.21) to the left and right hand side, respectively, a set of equations of the form

$$\mathbf{Ax} = \mathbf{b} \quad (2.23)$$

is obtained, which solution \mathbf{x} provides the unknown boundary values on S . When both v_n and p are known on S , the pressure $p(\vec{x})$ at every point $\vec{x} \in V$ is given by Eqs. (2.17) or (2.20) by a numerical integration along S .

The BEM for exterior problems suffers from non-uniqueness of the problem at characteristic frequencies. Within the scope of this thesis, the CHIEF method [15] was implemented into the BEMLAB code. This procedure is described in detail in Section 3.4.

Chapter 3

BEM for calculating combustion noise

3.1. Background

3.1.1. Introduction to combustion noise

Noise is a major environmental health problem. In the Green Paper on Future Noise Policy of the European Commission from 1996 it is stated “that around 20% of the Union’s population or close on 80 million people suffer from noise levels that scientists and health experts consider to be unacceptable” and “an additional 170 million citizens are living in so-called ‘grey areas’ where noise levels are such to cause serious annoyance during daytime” [35]. Studies carried out in Sweden, Germany and elsewhere revealed that this situation did not change much in the last years. Fig. 3.1 shows the results of a poll in Germany for the years from 2000 to 2008 concerning the noise exposure of residents. Road traffic can be recognized as the main contributor to human noise annoyance. But also around 30% of the respondents have stated that they are annoyed by air traffic and industrial noise, revealing even an upward trend concerning industrial noise [37]. It is obvious, that there is a strong need for an improved noise control in these fields. To meet this demand in the area of air traffic, the Advisory Council for Aeronautics Research in Europe (ACARE) formulated the aim of a combined noise reduction of 10 dB per aircraft operation as the first goal until 2020, which requires amongst others a low noise powerplant architecture and improved numerical aeroacoustic simulation [38]. More accurate computation methods for aircraft noise and industrial noise were also identified as research needs along with the implementation of the EU directive 2002/49/EC relating to the assessment and management of environmental noise [39]. Since the noise

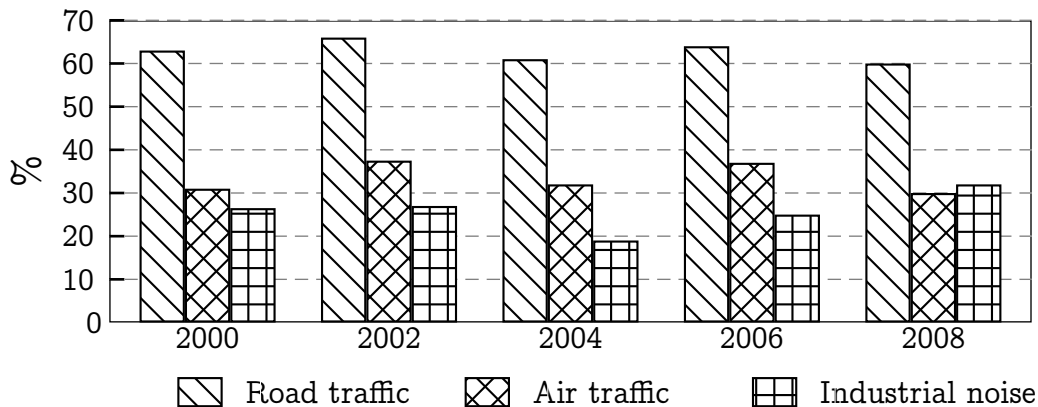


Figure 3.1.: Percentage of people annoyed by noise. Results of a poll in Germany [36, 37].

emission of combustion systems (combustion noise) is an integral part of air traffic and industrial noise, the understanding and control of combustion noise has become an important research area. The following aspects outline the need for research:

- The development of modern combustion chambers with reduced pollutant emissions, in particular oxides of nitrogen, are accompanied by an increase of noise emission [40, Ch. 7].¹
- Industrial flare systems represent a high-level noise source. Flare systems need a reliable and accurate prognosis model, since they can not be decommissioned due to safety reasons once they are put into operation [41].
- In view of the ACARE agenda a substantial reduction of the jet and fan noise of aircraft can be expected in the future. With the development of high-bypass turbofan engines, combustion noise will become a more and more important noise source [42].

The noise emission from combustion systems can be subdivided into the processes:

- Sound generation in the flame zone
- Sound propagation in the ambient inhomogeneous medium
- Sound radiation into the far field
- Interaction with the structure of the combustion chamber

¹The increasing interest in combustion noise is also indicated by the fact, that the first edition of [40] from 1983 did not contain the chapter “Combustion Noise” at all.

The sound generation mechanisms are split into direct and indirect combustion noise. The direct combustion noise relates mainly to the unsteady process of volumetric expansion in the reactive regions, i.e. on the fluctuating heat release rate. The indirect combustion noise is linked to temperature fluctuations, which pass through an inhomogeneous region of strong mean flow gradients as an exhaust or nozzles. A comprehensive review of the state of knowledge regarding combustion noise can be found in [43].

In the light of the increased significance of combustion noise and as a result of discussions within the German research network “Leiser Verkehr”, in which a need of a fundamental research concerning combustion noise was identified, the German research initiative “Combustion Noise” was founded.

3.1.2. Research group “Combustion Noise”

The research group “Combustion Noise” was founded in the year 2002 and was funded by the German Research Foundation (DFG) until 2008. The aim of the initiative was the development of techniques for the prediction and minimisation of combustion noise. The research initiative concentrated on the first three of the aforementioned elements of the noise emission of combustion systems, concerning both, direct and indirect combustion noise. One research focus was the flow field simulation with method from Computational Fluid Dynamics. Key simulation techniques were the Large Eddy Simulation (LES) and Unsteady Reynolds Averaged Navier-Stokes simulations (URANS) to model the flow field in the flame zone and provide input data for the acoustical simulation tools. A high resolution 3D-Direct Numerical Simulation was developed to provide verification data for the coarser LES and URANS methods. The second research focus laid on the modelling of the sound propagation in the inhomogeneous region close to the flame zone and in the homogeneous far field basing on the data of the CFD simulations. The applied methods were the Acoustic Perturbation Equations (APE), the Boundary Element Method (BEM) and Equivalent Source Method (ESM). The third research focus were the experimental investigations of the influence of different burner configurations on the sound radiation as well as the influence of boundary conditions. New experimental techniques were developed for the analysis of the local velocity measurements to validate a simplified spectral model for the fluctuating heat release in the flame zone. The development of an acoustical near field holography for an direct measurement of acoustic sources in combustion chambers has been in progress. Another two projects focussed on the numerical and experimental determination of indirect combustion noise in

enclosed combustion chambers. The main findings of the ten research projects of the Combustion Noise initiative are compiled in the joint project report [44]. A collection of scientific papers on recent research results of the projects were published in a special issue on combustion noise in the journal *Acta Acustica united with Acustica* 95(3) in May/June 2009.

The work presented in this thesis is related to the studies of project 4 of the research group: “Modelling of the sound radiation from flames by means of acoustic equivalent sources”. This project dealt with the sound propagation from the source region into the far field, where the radiated sound power of combustion systems has an effect on the overall human noise exposure.

3.1.2.1. Research project “Modelling of the sound radiation from flames by means of acoustic equivalent sources”

The aim of the fourth project was to investigate the application of the equivalent source method (ESM) to aero- and thermodynamic sound sources. The ESM is a powerful and established numerical method for the sound radiation of vibrating solid bodies. On the one hand the project focussed on a correct prediction of the far field sound radiation and on the other hand on a clarification of the connection between the acoustic characteristics of the far field (spectral sound power density, directivity) and physical quantities of the thermodynamical and fluid mechanical processes in the flame zone. Subtasks were studies relating to the general applicability of the ESM to thermo- and aerodynamical problems, matching of the physical measures at a control surface and the design and computational implementation of the method. Soon after the project start, the Boundary Element Method (BEM) was also included in the project scope. On the one hand, it should serve as a reference method from the area of computational acoustics and on the other hand, the BEM is well suited as an engineering tool. Whereas the ESM allows a physically motivated choice of the multipole source points according to Lighthill’s acoustic analogy, the BEM prescribes a set of monopole and dipole sources on a control surface enclosing the physical acoustical sources. The uncertainties of the ESM, i.e. the proper choice of source points and order of the equivalent multipoles and the high condition number of the resulting matrices are remedied by the stringent specification of a BEM model. Thus, in view of the development of predictions tools for a wider user range, the BEM is an appropriate module within a modelling chain for combustion noise.

Project 4 collaborated with the other projects in different ways. The main cooperating partners were

Project 1: Institute of Combustion Technology, DLR Stuttgart: “Numerical URANS simulations of combustion noise”,

Project 2: Institute for Chemical Technology and Engler-Bunte Institute, Division of Combustion Technology, University of Karlsruhe: “Measurement and simulation of noise emitted from swirl-burners with different burner exit geometries”,

Project 3: Institute for Energy and Powerplant Technology, Technical University of Darmstadt: “Modelling of noise sources in combustion processes via Large-Eddy-Simulation”,

Project 6: Institute of Thermodynamics, Technical University München: “Influence of boundary conditions on the noise emission of turbulent pre-mixed swirl flames”,

Project 7: Institute of Aerodynamics, RWTH Aachen University: “Simulation of combustion noise in the near field of premixed and diffusion flames”.

The input data for the acoustical methods ESM and BEM were provided by the CFD groups, namely project 2 and 3. The acoustic measurement data of the noise emission of open, non-premixed, turbulent jet flames, determined in cooperation with project 3, served as validation data for several partners, such as project 1, 3 and 7 [45, 46]. Project 6 was extensively advised regarding the setup of an acoustical measurement environment. The position of project 4 within the research group is illustrated in Fig. 3.2. The arrows indicate the flow of data and information. Certainly, a scientific exchange took place with all project partners at the regular meetings and conferences. Project 4 was located at the Technical University of Dresden, Institut für Akustik und Sprachkommunikation, and the Beuth Hochschule für Technik Berlin, formerly Technische Fachhochschule Berlin. While the work of project 4 covered various aspects, the thesis is limited to what is indicated by the centre line of Fig. 3.2. The focus lays on the coupling of an incompressible LES with the BEM to determine the far sound field, namely the radiated sound power level of open, non-premixed, turbulent jet flames. The numerical results are compared to measurement data.

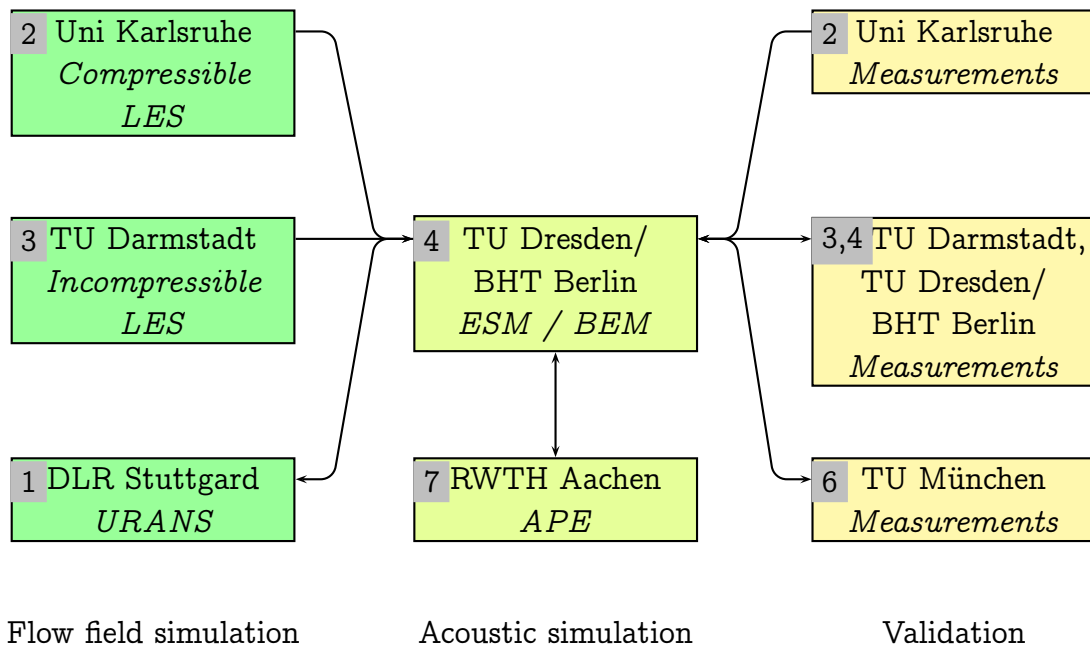


Figure 3.2.: Position of project 4 within the research group “Combustion Noise”.

3.2. Object of study: turbulent, non-premixed jet flames

As the title of this section indicates, there are a lot of different flame types. The basic flame types are distinguished by their premixedness and flow type [47, Ch. 1.3]. In non-premixed flames fuel and the oxidizer are mixed during the combustion process itself, i.e. combustion and mixture occur simultaneously. Due to safety reasons non-premixed flames are mostly used in industrial burners. The flow field can be laminar or turbulent depending on the characteristic Reynolds number of the flow field. Non-premixed and turbulent combustion systems can be found in many practical applications, such as aircraft turbines and diesel engines. Jet flames are open flames, where the fuel exits from a pipe into the surrounding air or the laminar co-flow. Fig. 3.3 shows a principal sketch of a jet flame. Jet flames are not of much practical importance, but they have the advantage of being the reactive counterpart of non-reactive jets, which were thoroughly investigated in the past, both numerically and experimentally. This is mainly an issue for the CFD simulation, which must be able to reliably predict the aerodynamic and chemical processes in the flame. The cooperation partners at the Institute

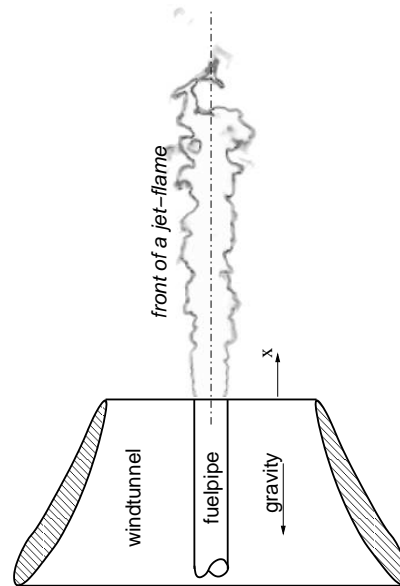


Figure 3.3.: Principal sketch of a non-premixed, turbulent jet flame (from [48, Fig. 6.1, p. 57]).

for Energy and Powerplant Technology, Technical University Darmstadt, could provide Large-Eddy-Simulations of H_2/N_2 jet flames, i.e. the fuel is hydrogen H_2 , which is diluted by nitrogen N_2 . These flames were studied in detail at this institute for several years [48–52].

The investigated jet flames are named HD and H3. The H3-flame is a benchmark flame of the TNF workshop [53]. Parameters of the two flames can be found in Table 1 of Paper II. The paper also provides a brief description of the LES approach, snap-shots of the flame front etc. and presents the validation of the LES results. The fuel of the HD-flame is highly diluted to slow down the chemical reactions. Therefore it is a “hardly” burning flame, but numerically very stable. The H3-flame is characterised by higher temperatures, density gradients and expansion rates and, therefore, causes more numerical problems [48, Ch. 6.2].

3.3. The hybrid approach

Currently, the acoustic far field produced by turbulent flames cannot be determined only by a CFD simulation because the computational cost would be enormous. Instead, hybrid methods, in which the turbulent reactive flow in the source region and the acoustic far field are computed separately, are more effec-

tive and require less computational time and resources. Hybrid methods have been widely used in the area of aeroacoustics to determine the sound radiation from non-reacting turbulent flows [54, 55]. There are few publications on hybrid approaches for the computation of combustion noise. Klein has investigated the coupling of a steady state CFD combustion calculation with an integral expression for the governing noise sources [56, 57]. The ‘‘Combustion Noise’’ research group developed further hybrid approaches. Flemming et al. have combined the incompressible LES of the H3-flame and other turbulent flames with a wave propagation solver implemented in the CLAWPACK package to obtain the sound field in the vicinity of the flame zone [46, 52]. The far field is obtained by an extrapolation via a scaling factor. Bui et al. have coupled the same incompressible LES of the H3-flame with reactive acoustic perturbation equations for the prediction of the generated sound field [45, 58]. In [59] Zhang et al. have employed Lighthill’s acoustic analogy to evaluate the acoustic source of the flame of a premixed swirl burner. The reacting flow field was modelled by a compressible LES.

In this thesis the Boundary Element Method (BEM) is presented as an acoustic continuation of the source-region simulation, which is performed by an incompressible LES. So far, the BEM has been used in aeroacoustic hybrid approaches for aeroacoustic analyses of lifting bodies (wings and rotors) [60, 61], of a circular cylinder in a cross flow [62] and of noise from engine inlets [63].

3.3.1. Coupling of BEM and LES: A discussion

In the present approach, the computational domain is divided into two regions, the combustion zone, where the Navier-Stokes equations are solved by an incompressible LES, and the radiation zone, where the BEM is applied to solve the homogeneous Helmholtz equation (Fig. 3.4). The homogeneous Helmholtz equation reads

$$\nabla^2 \varphi - \frac{1}{c_0^2} \frac{\partial^2 \varphi}{\partial t^2} = 0 \quad (3.1)$$

with φ as acoustic quantity satisfying the wave equation in the acoustic domain. The interface between the two regions is named Kirchhoff’s surface [64]. It must enclose all sound sources and non-linear effects, i.e. the acoustic field can be assumed as linear outside the Kirchhoff’s surface. This coupling approach was not indisputable within the research community. The main point of contention was and is the use of the velocity data of an incompressible LES as input data for the subsequent BEM calculation. A more common concept is the use of a three-zonal approach for the calculation of combustion noise [65]. The zones are the

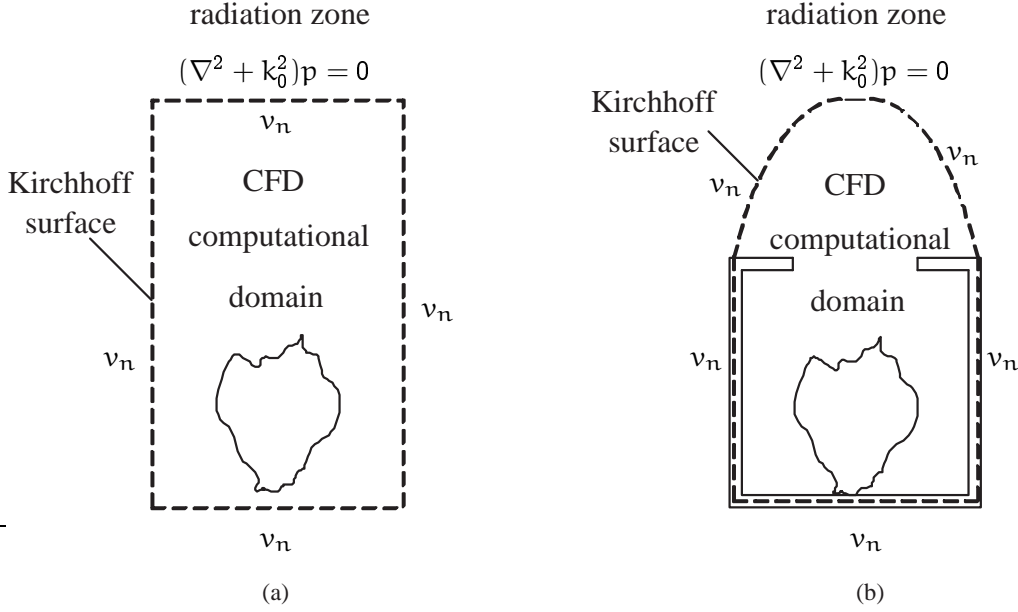


Figure 3.4.: Hybrid approach for a) open flame; b) enclosed flame.

source zone, the propagation zone and the far field. The source zone is governed by the full Navier-Stokes equations, either compressible or incompressible. The governing equation of the propagation zone is a convective wave equation over varying mean flow, which is solved numerically. The source terms of the convective wave equation are derived from the numerical solutions in the source zone. Propagation and source zone are required to overlap. The far field is governed by the homogeneous wave equation and is attached to the propagation zone. A two-zonal approach, where the source zone is directly coupled to the far field, is assumed to require the solution of the compressible Navier-Stokes equations, which should provide the correct acoustic pressure and velocity data at the zonal interface. This concept bases on the model of three basic modes of fluctuation within a flow: the vorticity mode, the sound mode and the entropy mode [66, 67]. The vorticity mode, which is linked to an incompressible flow is solenoidal and decoupled from the sound mode as long as the Mach number of the flow is low. An incompressible simulation is only able to reproduce the vorticity mode. Therefore, the acoustic waves, which are produced in the source zone, are not transported to the Kirchhoff's surface and a direct coupling of an incompressible LES and BEM as proposed in this work yields reliable results only by chance. These are the objections.

The works of Flemming et al. [46, 52] and Bui et al. [45, 58] follow the three-zonal approach, but a complete solution for the third zone, the acoustic far field, could not be achieved. Instead the sound field is evaluated only at individual field points in the propagation zone. An overall measure as the radiated sound power of the turbulent flames is not available. Concerning the two-zonal approach, there have been only few numerical studies done on the sound generation from open turbulent flames, which bases on a compressible CFD simulation. Zhang et al. [59] has extracted noise sources of a swirl flame following Lighthill's acoustic analogy out of a compressible LES. Zhao et al. used a compressible direct numerical simulation (DNS) for the prediction of the acoustic far field dilatation. Measurable acoustic quantities as sound pressure or intensity are not obtained. A complete two-zonal approach, which provides a reliable prediction of the acoustic far field, has not been published yet. This is mainly due to the high computational effort of a compressible simulation, the difficulty to realise non-reflecting boundary conditions [68] and that most compressible methods become inefficient at low Mach numbers [69, Ch. 10.1].

The approach in this thesis follows a modified two-zonal concept, namely the direct coupling of an incompressible simulation of the source zone and an acoustic far field method. Commonly, an incompressible flow is considered to be characterised by a constant density. The equation for the conservation of mass reads

$$\frac{\partial \rho}{\partial t} + \operatorname{div}(\rho \vec{v}) = 0 \quad (3.2)$$

or in another form after expanding the divergence term

$$\frac{1}{\rho} \frac{D\rho}{Dt} + \operatorname{div} \vec{v} = 0. \quad (3.3)$$

D/Dt denotes the substantial derivative with respect to the time t , $D\rho/Dt = \partial\rho/\partial t + \vec{v} \cdot \nabla\rho$. Assuming $\rho = \text{const}$ leads to a simplified form of Eq. (3.3), namely $\operatorname{div} \vec{v} = 0$. The resulting velocity field is divergence-free and does not contain any source of sound. However, the simplification $\rho = \text{const}$ can not be applied for reactive or mixing flows. But it is not a necessary condition for incompressibility. More generally speaking, a fluid is incompressible “when the density of an element of the fluid is not affected by changes in the pressure” [70, Ch. 2.2], i.e. $\partial\rho/\partial p = 0$. This is exactly the low-Mach-number approach of the incompressible LES for the turbulent jet flames. The missing equation of state, which would define the coupling of pressure and density, is replaced by a pressure correction. The pressure correction is an iterative process in which

a pressure parameter is adapted in such a way, that the resulting momentum $\rho\vec{v}$ fulfils Eq. (3.2) [48, Ch. 5.4]. Though a coupling of pressure and density is neglected, the conservation of mass, Eq. (3.2), remains one of the governing equations for the applied LES [48, Ch. 2.1.1]. Thus, the resulting velocity field has non-zero divergence, i.e. $\text{div}\vec{v} \neq 0$. According to [67] such a velocity field is due to mass sources in an incompressible flow and part of the sound mode. Fluctuating mass (or volume) sources are known as one of the basic sound-generating mechanisms [71, Ch. 3.6.1]. Unlike the not transported pressure waves, the velocity field with non-zero divergence does exist at the Kirchhoff's surface, which encloses the source zone. It represents the sound sources due to the combustion processes inside the source zone. The pressure as a pure correction parameter is not suited as coupling variable for an acoustic continuation of the flame zone. But the BEM requires only one acoustic parameter as boundary condition at the Kirchhoff's surface. The correct pressure is obtained by solving the Helmholtz equation at the boundary, i.e. the Kirchhoff's surface.

This argumentation is supported by the works of Strahle [72, 73], who identified violent density fluctuations inside the combustion region as sound generation mechanism

$$\rho(r, t) = \frac{1}{4\pi c_0^2 r} \frac{\partial^2}{\partial t^2} \int_V \rho_T \left(\vec{r}_0, t - \frac{r}{c_0} \right) dV(\vec{r}_0). \quad (3.4)$$

ρ_T are density fluctuation due to turbulent fluctuations and not due to the acoustic field. In [73] he showed the correspondence between Eq. (3.4) and an expression for the far field density fluctuations as surface integral over the velocity fluctuation along a control surface A , which encloses the combustion zone,

$$\rho(r, t) = \frac{\rho_1}{4\pi c_0 r} \frac{\partial}{\partial t} \int_{S_1} v_{n,T} dS(\vec{r}_0), \quad (3.5)$$

where ρ_1 is the mean density in the region of burnt gas. He states, that "only velocity fluctuations (produced by strong interior density fluctuations) on the outer flame surface are responsible for significant sound output" [73]. In [74, Sec. 4] on the *Theory for simple premixed turbulent jet flames radiating to a free field* this finding is corroborated by the statement: "the flame induces noise by causing a fluctuation in the outward normal component of the velocity on A " (A is equal to S_1 in Eq. 3.5). Strahle's formulas were later slightly corrected by multiplying ρ_0/ρ_1 to ensure, that all acoustic sources are included [75, Ch. 13.2]. This corresponds to locating the enclosing control surface S_1 in a region, where the fluid density equals the density of the ambient medium ρ_0 .

The direct coupling of the incompressible LES and the BEM transcribes these conclusions into a numerical scheme, which is able to obtain the pressure field induced by the dilatation fluctuations at the control surface enclosing the combustion zone. The control surface (Kirchhoff's surface) must be located in the ρ_0 -region and the Helmholtz equation must be valid outside the control surface.

3.3.2. Location of the Kirchhoff's surface

The Kirchhoff's surface, the interface between the source region and the acoustic domain, has to be located in a homogeneous medium, where the temperature and density equal those of the environment to fulfil the homogeneous Helmholtz equation and to include all acoustic sources as it was discussed in the previous section. Several cylindrical Kirchhoff's surfaces were extracted from the given LES meshes, which vary in the radius of the lateral surface. This procedure is described in Section 4.1 of Paper IV. In Table II of the same paper the characteristics of the Kirchhoff's surface can be found. The first cylindrical control surface has the smallest radius, the tenth surface has the largest radius. Fig. 3.5 and Fig. 3.6 show the density and temperature distribution of the first, fifth and tenth Kirchhoff's surface around the HD- and H3-flame, respectively.

While the density as well as the temperature at the lateral surfaces of the smaller cylinders differ from those of the ambient medium ($\rho_0 = 1.21 \text{ kg/m}^3$ and $T_0 = 300 \text{ K}$), the lateral surfaces of the largest cylinders are located in the ambient, homogeneous medium. But the outflow caps intersect with the propagating flow, hence, they are still affected by the density and temperature fluctuations due to the combustion processes inside the control surface. The requirement of placing the Kirchhoff's surface in the homogeneous medium around the source region is violated at the outflow caps, which will disturb the calculation of the correct sound field outside the Kirchhoff's surface. However, regarding the different Kirchhoff's surfaces, the one with the largest radius best suits the location requirement, because at least its lateral surface is completely located in the homogeneous radiation zone.

In Section 6.2 of Paper IV the outflow area of the Kirchhoff's surfaces is identified as the main error source for the determination of the overall radiated sound power of the HD- and H3-flame (Fig. 15 of Paper IV). Its erroneous contribution to the sound field outside the Kirchhoff's surface might be caused, among other reasons, by the differing density and temperature distributions at this part of the control surfaces.

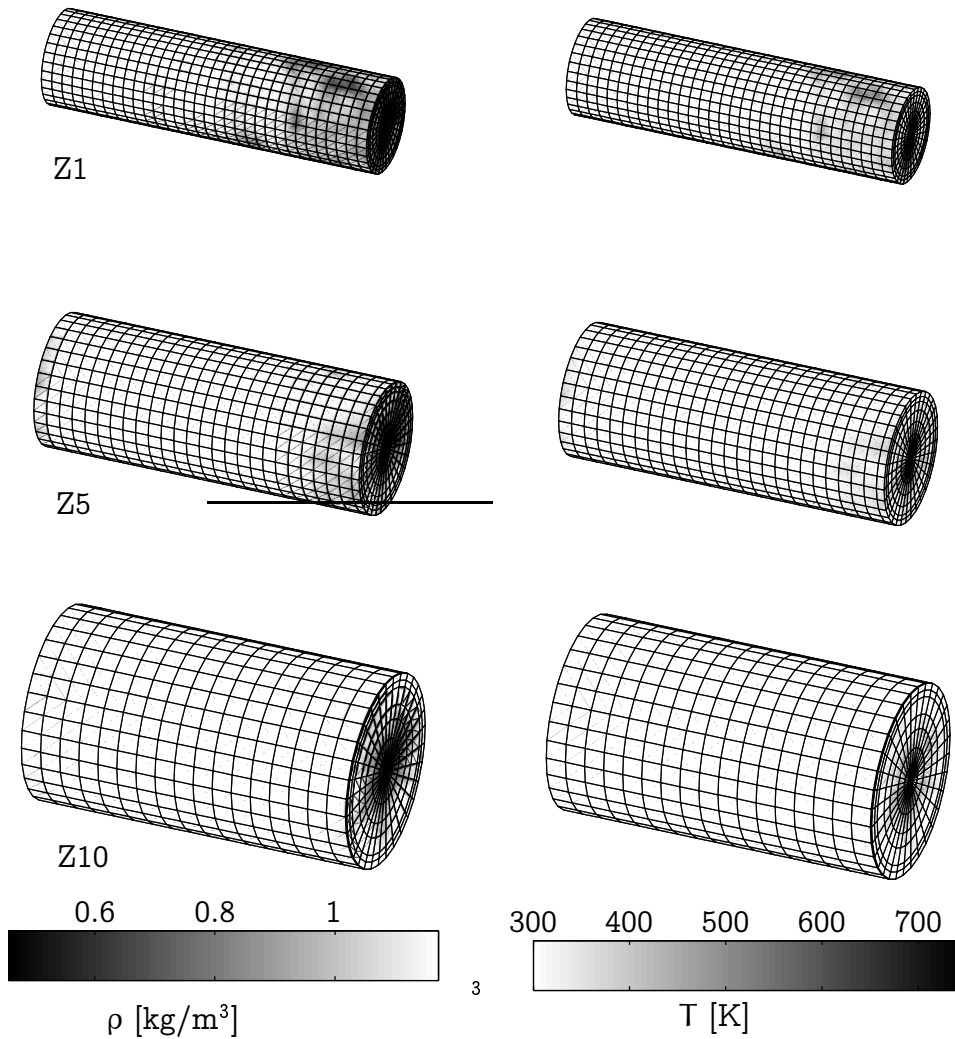


Figure 3.5.: Instantaneous density (ρ) and temperature distribution (T) at the first, fifth and tenth cylindrical control surfaces around the HD-flame.

3.3.3. Determination of an average sound power spectrum

The experimental determination of the sound power spectra of the flames bases on the measurement of the average sound intensity spectra on a control surface S_m , which encloses the burning flames.² The sound power P_W is then given by

²The measurements are described in detail in Section 5 of Paper IV.

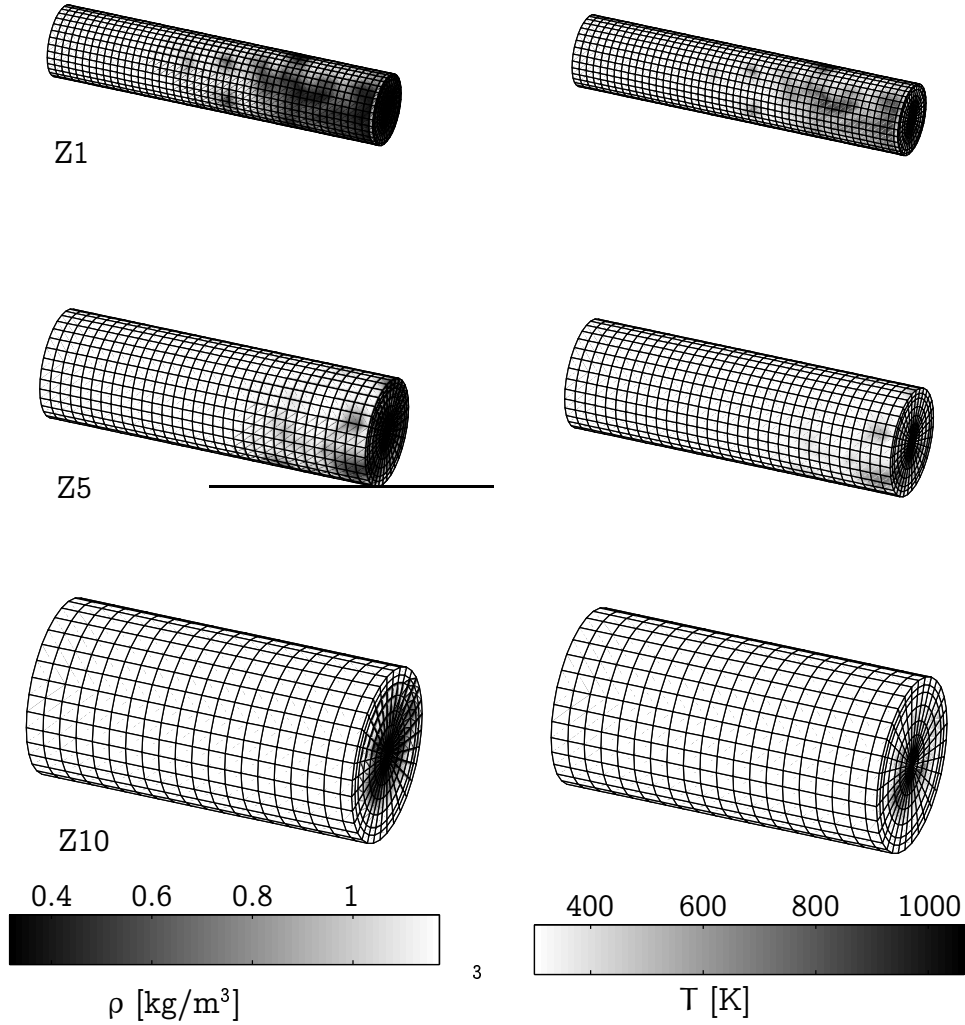


Figure 3.6.: Instantaneous density (ρ) and temperature distribution (T) at the first, fifth and tenth cylindrical control surfaces around the H3-flame.

the integral over the normal sound intensity along the control surface S ,

$$P_W = \int_S I_n dS. \quad (3.6)$$

The sound intensity spectra at the measurement points were obtained by an averaging of the measured spectra during 5 seconds. Concerning the numerical simulations, the time series of the velocity at the Kirchhoff's surface around the HD- and H3-flame, which were calculated by the LES, have a length of 0.17 s and

0.26 s, respectively. Using the complete time series as input data for the BEM calculation without any averaging leads to noisy sound power spectra. Fig. 3.7 exemplarily shows a non-averaged sound power spectra of the HD-flame. Obviously the numerical simulations also require an averaging process to reduce the spectral variance of the resulting power spectra.

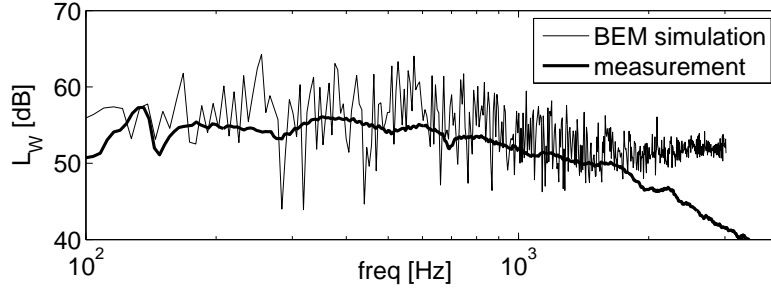


Figure 3.7.: Measured and simulated sound power spectrum of the HD-flame. The simulation results were obtained without any averaging.

The time-averaged sound intensity in stationary sound fields is defined as [76, p. 24 ff]

$$\tilde{I}_n = \langle \tilde{p}(t)\tilde{v}_n(t) \rangle = \lim_{T \rightarrow \infty} \frac{1}{T} \int_0^T \tilde{p}(t)\tilde{v}_n(t) dt, \quad (3.7)$$

By expressing Eq. (3.7) as cross-correlation function and using definitions of probability theory relating to stationary random signals, the corresponding function in the frequency domain can be derived as cross-spectral density ³ [77, Ch. 18.10]

$$I_n(\omega) = \lim_{T \rightarrow \infty} \frac{1}{T} p(\omega)v_n(\omega) \quad (3.8)$$

Eq. (3.8) denotes the intensity spectral density. The expected value considering N independent measurement sequences is similarly given in the time and in the frequency domain by

$$\bar{I}_n = \lim_{N \rightarrow \infty} \frac{1}{N} \sum_{i=1}^N \lim_{T^i \rightarrow \infty} \frac{1}{T^i} \int_0^{T^i} \tilde{p}^i(t)\tilde{v}_n^i(t) dt, \quad (3.9)$$

$$\bar{I}_n = \lim_{N \rightarrow \infty} \frac{1}{N} \sum_{i=1}^N \lim_{T^i \rightarrow \infty} \frac{1}{T^i} p^i(\omega)v_n^i(\omega). \quad (3.10)$$

³The derivation can be found in Appendix B.

The probability of each occurrence \tilde{I}_n^i and I_n^i is $p(\tilde{I}_n^i) = p(I_n^i) = 1/\forall i$. Eq. (3.10) shows that the mean intensity spectral density has to be determined by an averaging of the N individual intensity spectra $I_n^i(\omega)$, not by an averaging of the input velocity spectra. For this reason, the time series of the velocity data at the Kirchhoff's surface S were split into equidistant sequences and the spectral data of the normal velocity $v_n^i(\omega)$ of each sequence served as input data for a full BEM simulation to obtain the corresponding pressure distribution $p^i(\omega)$ on S and with that the intensity spectra I_n^i of the i th sequence. This procedure is described in Section 4.2 of Paper IV.

The matrix equations of a direct BEM calculation, Eqs. (2.21) and (2.23), show that the spectral velocity data of each sequence contribute to the vector \mathbf{b} in Eq. (2.23). Normally, the matrices \mathbf{H} and \mathbf{G} are not formed during a BEM calculation for memory reasons. In this case, for each of the N sequences the vector $\mathbf{b} = j\omega\rho_0\mathbf{G}\mathbf{v}$ has to be separately determined at each frequency step. Therefore, the calculation of an average frequency response of the radiated sound power requires much time.

In the following the use of mean transfer functions as input data for the BEM calculation will be investigated as alternative to the procedure, that were applied in Paper IV.

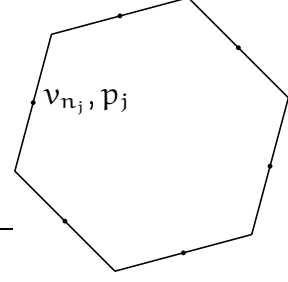
3.3.3.1. Use of mean transfer functions \hat{v}_n as input data for a BEM calculation

Background The normal velocity $v_{n,j}$ at the M elements of the BEM mesh can be represented as transfer function with respect to a reference velocity $v_{n,m}$ with $1 \leq j, m \leq M$. The reference element m is arbitrary, but not varying. With the use of these transfer functions $\hat{v}_{n,j}$ as input data in a BEM calculation the corresponding transfer function \hat{p}_j are obtained at the surface mesh. In a linear, time-invariant system the transfer functions do not change with time. Hence, it should be sufficient, to determine $\hat{v}_{n,j}$ and \hat{p}_j by one BEM calculation along with the mean of the square modulus of the reference velocity $\overline{|v_{n,m}|^2}$ to obtain the average intensity and sound power spectra. In this section, it will be investigated, if this procedure can be applied to the open flames to reduce the computational effort for the determination of the average spectra.

According to Eq. (3.8), the intensity spectrum on the j th element is given by

$$I_{n,j} = \lim_{T \rightarrow \infty} \frac{1}{T} p_j v_{n,j}^*. \quad (3.11)$$

Figure 3.8.: Generic boundary value problem. The surface of the structure is divided into M boundary elements. The normal velocity and the pressure at one j th element are denoted by $v_{n,j}$ and p_j with $1 < j < M$.



In Eq. (3.11) and the following formulas, the dependence on ω is omitted. Furthermore, the expression intensity spectral density is abbreviated as intensity spectrum. The pressure p_j at the j th surface element is determined by the prescribed velocity distribution at the Kirchhoff's surface

$$p_j = \sum_{k=1}^M H_{kj} v_{n,k}. \quad (3.12)$$

The transfer functions H_{kj} result from the BEM calculation and are not known *a priori*. Substituting $v_{n,j}$ in Eqs. (3.11) and (3.12) by the transfer functions $\hat{v}_{n,j}$

$$\hat{v}_{n,j} = \frac{v_{n,j}}{v_{n,m}} = \frac{v_{n,j} v_{n,m}^*}{|v_{n,m}|^2} \quad (3.13)$$

yields the following expression for the intensity spectrum on the element j

$$I_{n,j} = \lim_{T \rightarrow \infty} \frac{1}{T} |v_{n,m}|^2 \hat{v}_{n,j}^* \sum_{k=1}^M H_{kj} \hat{v}_{n,k}. \quad (3.14)$$

According to Eq. (3.10) the mean intensity spectrum is determined by

$$\overline{I_{n,j}} = \lim_{N \rightarrow \infty} \frac{1}{N} \sum_{i=1}^N \left(\lim_{T^i \rightarrow \infty} \frac{1}{T^i} |v_{n,m}^i|^2 \hat{v}_{n,j}^{i*} \sum_{k=1}^M H_{kj} \hat{v}_{n,k}^i \right). \quad (3.15)$$

As long as system is linear the transfer function $\hat{v}_{n,j}$ and the absolute value of the reference velocity $|v_{n,m}|^2$ are stochastically independent variables. Hence, the mean or expected value of their product equals the product of the expected values of the individual variables [78, Theorem (4.7)]. Applying this product rule to Eq. (3.15) yields

$$\overline{I_{n,j}} = \lim_{T \rightarrow \infty} \frac{1}{T} \overline{|v_{n,m}|^2} \overline{\hat{v}_{n,j}^*} \sum_{k=1}^M H_{kj} \overline{\hat{v}_{n,k}}. \quad (3.16)$$

Eq. (3.16) represents the possibility to determine the average intensity spectrum by using the mean transfer functions $\overline{\hat{v}_{n,j}}$ as input data for the BEM calculation and the mean square modulus of the reference velocity $\overline{|v_{n,m}|^2}$ as amplitude factor as long as the considered problem is linear. The N time intervals are assumed to have the same length, i.e. $T^i = T \forall i$.

Example In this paragraph Eq. (3.16) is tested with measurement data. The two pressure signals of an intensity probe, recorded during intensity measurements on a jet flame, serve as example data. Fig. 3.9 shows the spectral coherence $\gamma_{p_1 p_2}$ of the two pressure signals, which is given by

$$\gamma_{p_1 p_2} = \frac{G_{p_1 p_2} G_{p_1 p_2}^*}{G_{p_1 p_1} G_{p_2 p_2}}. \quad (3.17)$$

where $G_{p_i p_j}$ denotes the one-sided cross-spectra of the two pressure spectra p_i and p_j with $1 \leq i, j \leq 2$. The spectral coherence is close to 1 up to 1 kHz, but

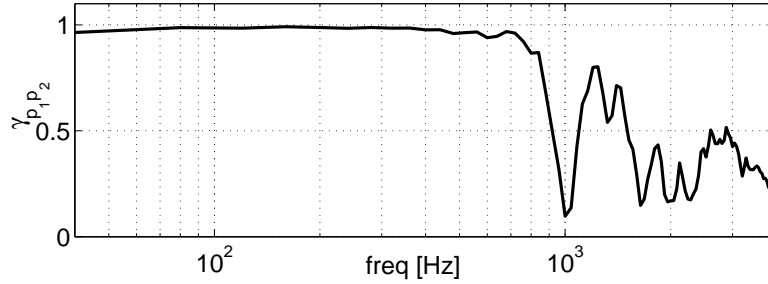


Figure 3.9.: Coherence $\gamma_{p_1 p_2}$ of the two pressure signals p_1 and p_2 of an intensity probe.

above 1 kHz the linear dependence of the pressure signal decreases. The one-sided real intensity spectrum in direction of the probe is given by

$$I_r = -\frac{\Im\{G_{p_1 p_2}\}}{\omega \rho_0 r} = -\frac{\Im\{p_1 p_2^*\}}{\omega \rho_0 r}. \quad (3.18)$$

The parameter r denotes the distance of the two microphones. The average intensity spectrum is given by

$$\overline{I}_r = -\frac{1}{\omega \rho_0 r} \Im\{\overline{p_1 p_2^*}\} = -\frac{1}{\omega \rho_0 r} \Im\left\{\overline{\frac{p_1}{p_2} |p_2|^2}\right\}. \quad (3.19)$$

Again, the ratio p_1/p_2 as well as the square modulus $|p_2|^2$ are stochastically independent. Therefore, the mean operator is multiplicative, and the average

intensity spectrum can be obtained by an separate averaging of the variables,

$$\overline{I}_r = -\frac{\mathfrak{J}\{\overline{p_1/p_2}\}}{\omega \rho_0 r} \overline{|p_2|^2}. \quad (3.20)$$

In Fig. 3.10 the average intensity spectra according to Eqs. (3.19) and (3.20) are shown basing on different numbers of averaging steps N . As shown in the lower

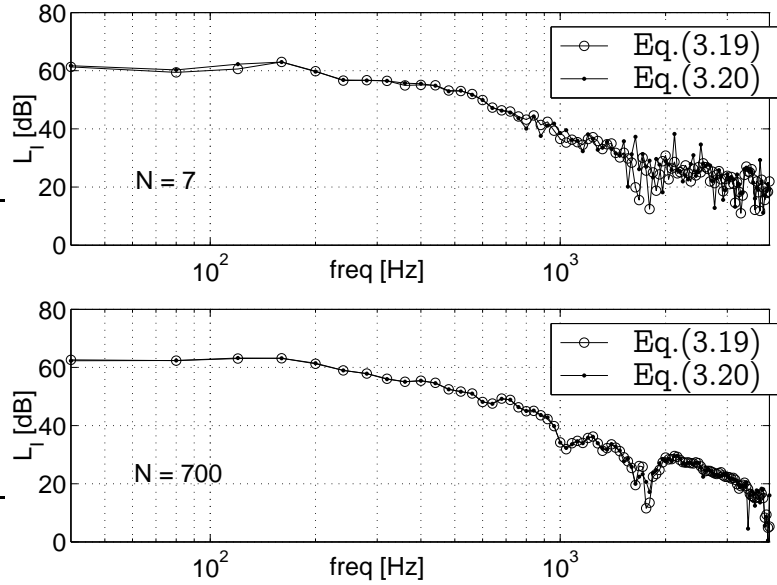


Figure 3.10.: Average intensity spectra according to Eqs. (3.19) and (3.20). *Upper plot:* Average over $N = 7$ spectra, *lower plot:* Average over $N = 700$ spectra.

plot of Fig. 3.10, both equations lead to the same average intensity spectrum provided that the number of averages is sufficient. Especially, in the frequency range of low coherence of the two pressure signals, more than 7 averages are required to minimize the spectral variance of the intensity spectrum. This example validates the separate averaging of the transfer functions and the amplitude spectra and therewith it confirms Eq. (3.20) as well as its equivalent Eq. (3.16).

Application to the H3-flame As discussed in the previous paragraphs, an average intensity spectrum can be obtained by an averaging of the individual intensity spectra relating to the different time data sequences, Eq. (3.8), as well as by the use of mean transfer functions $\overline{\hat{v}_{n,j}}$ as input data of the BEM calculation, Eq. (3.16). The advantage of the latter procedure is that the averaging is made

before the BEM calculation and only one BEM frequency run is necessary to get the averaged spectra. Fig. 3.11 shows both approaches for the calculation of the average sound power spectrum of the H3-flame. The sound power spectra were calculated from the first, fifth and tenth Kirchhoff's surface⁴. Clearly, in case of

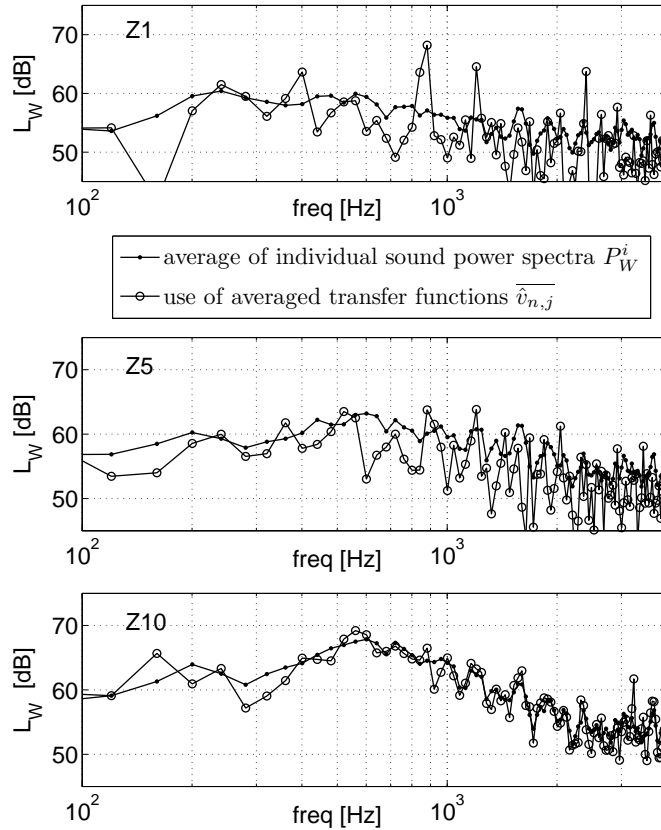


Figure 3.11.: Calculated average sound power spectra of the H3-flame according to Eqs. (3.8) and (3.16) on the basis of different Kirchhoff's surface around the flame. *Upper plot:* first and smallest Kirchhoff's surface Z1, *middle plot:* fifth Kirchhoff's surface Z5, *lower plot:* tenth and largest Kirchhoff's surface Z10.

the first and fifth Kirchhoff's surface, the both approaches do not lead to the same average sound power spectra. The spectra, which are obtained from the mean transfer functions, show a high spectral variance and differ from the average spectra, which are based on the averaging of the individual sound power spectra P_W^i of each data sequence. However, regarding the tenth Kirchhoff's surface, which

⁴See Section 4.1 of Paper IV for a characterisation of the different Kirchhoff's surfaces around the H3-flame.

is the largest one around the H3-flame, the two spectra deviate only slightly in the lower frequency range, and the overall agreement of the two approaches is very high. This result allows two conclusions. First, Eq. (3.16) is correct and allows a time-saving alternative averaging procedure by the use of mean transfer functions provided that the system is linear and the transfer functions and the reference spectra are stochastically independent. Second, these requirements are fulfilled at the tenth Kirchhoff's surface, i.e. the largest Kirchhoff's surface is located in the linear propagation region. Probably, the velocity data at the smaller Kirchhoff's surfaces are disturbed by inhomogeneities of the flow. This assumption corresponds to the findings in Section 3.3.2, where strong deviations from the ambient density and temperature were detected at the smaller control surfaces.

The coherence of the velocity data depends strongly on location of the considered test element with respect to the reference element. The coherence of the velocity data of close elements is very high, the data of remote elements show only a low coherence. The results in Fig. 3.11 are obtained by choosing the reference element on the lateral surface of the Kirchhoff's surfaces close to the outflow cap, see Fig. 3.12(a). In Fig. 3.12(b) the coherence between the velocity data of several test elements and the reference element at the tenth Kirchhoff's surface (Z10) can be found. The elements B and C are close to the reference element and their velocity data are highly coherent with the reference data, though element C lies at the outflow cap. Elements A, D and E are more remote to the reference element and their velocity data show a lower coherence. Element E is located opposite to the reference element at the lateral surface. In view of the varying signal coherence along the surface, a high number of averages would be advantageous. Unfortunately the signal lengths of the velocity data, calculated by the LES were not very long, therefore the number of averages was limited to 7 in this example. It can be assumed that a higher number of averages would further smooth the frequency response of the sound power spectrum, which are obtained by mean transfer functions.

Summary The averaging of the sound power spectra to decrease the spectral variance is a necessary, but also time-consuming procedure. The use of mean transfer functions $\overline{\hat{v}_{n,j}}$ as input data for the BEM calculation is a time-saving alternative. It requires linearity of the considered problem and the stochastic independence of the instantaneous transfer functions $\hat{v}_{n,j}^i$ and the amplitude spectrum $|v_{n,m}^i|^2$ of the reference signal. The lower the signal coherence, the higher

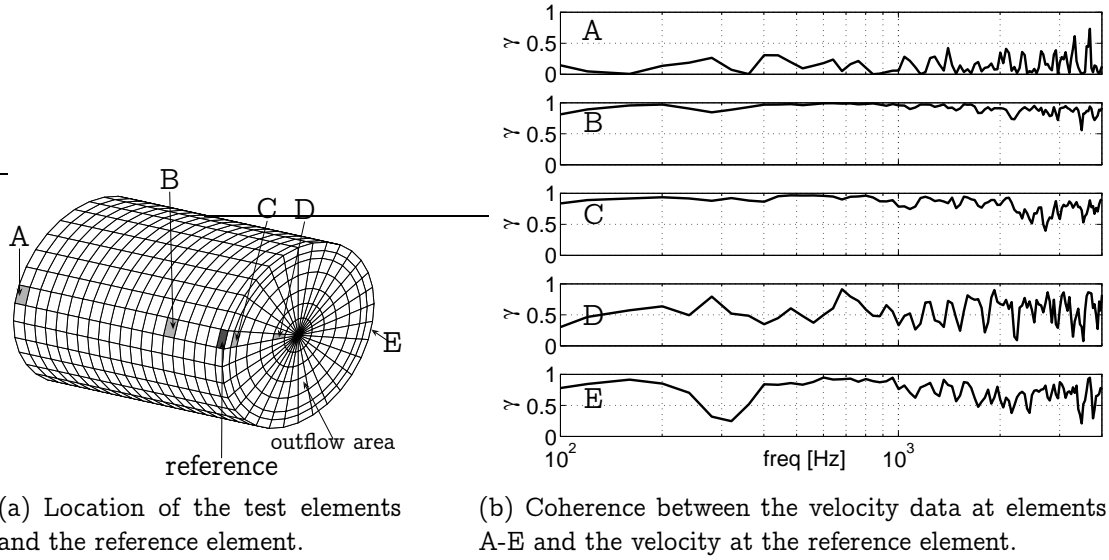


Figure 3.12.: Coherence between the velocity data at several surface elements and the reference element on the tenth Kirchhoff's surface (Z10) around the H3-flame.

the number of averages, which are needed to obtain a smooth intensity or power spectra. In the preceding section, the theoretical background of the alternative approach was investigated along with a validation of the derived formula by measurement data. The application of the alternative approach to the combustion noise problem shows that the resulting sound power spectra are very sensitive to the location of the Kirchhoff's surface. For the largest Kirchhoff's surface around the H3-flame a very high agreement to the classical averaging of the sound power spectra could be achieved. In this case, the use of mean transfer functions is the highly preferred averaging procedure because of the enormous reduction of the computational costs.

3.3.4. Downsampling of the surface data

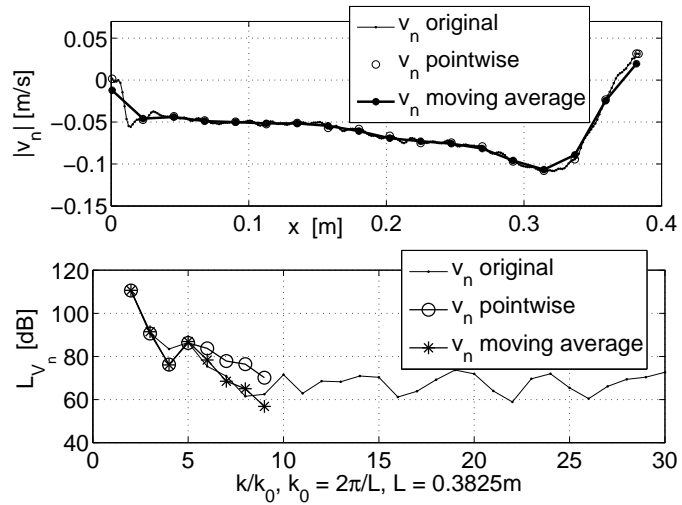
The LES grids were coarsened in axial and radial directions to form the BEM meshes of the Kirchhoff's surfaces around the flames as it is described in Section 4.1 of Paper IV. This mesh coarsening comes along with a downsampling of the given LES-Data. Since axial and radial resolutions were different, the grid in axial and radial directions had to be treated separately. The velocity data at the coarsened grid nodes can be sampled pointwise out of the finer mesh (in

case the grid nodes of both meshes coincide) or can be sampled in conjunction with a convolution with a spatial filter. The simplest filter is a rectangle filter, which results in the so called simple moving average. Both sampling techniques were applied to the HD-flame. A major or minor aliasing effect for the pointwise sampling is expected depending on the smoothness of the original normal velocity curve [79, Ch. 4]. The filtering with a the rectangle window function along the coarsened grid coordinates represents a low-pass filtering of the original signal and should provide a smaller aliasing effect in the wavenumber spectrum. The wavenumber spectrum $V_n(k_x)$ results from the Fourier transform from the spatial to the wavenumber domain, which is defined as

$$V_n(k_x) = \frac{1}{L} \int_0^L v_n(x) e^{-j k_x x} dx, \quad (3.21)$$

where L is the length of the cylinder. Fig. 3.13 shows the normal velocity along the axial direction x at $\phi = 0^\circ$ of the lateral surface of the tenth Kirchhoff's surface of the original and coarsened mesh.⁵ It can be seen that the velocity distribution

Figure 3.13.: Instantaneous velocity distribution in axial direction x at $t = 0.081s$ for the axial line of the tenth cylinder at $\phi = 0^\circ$, *upper plot:* spatial distribution, *lower plot:* wavenumber spectrum.



is quite smooth, the pointwise extracted data as well as the filtered data (moving average) follow the curve of the given data. Nevertheless, in the wavenumber spectrum an aliasing effect can be observed in the higher wavenumber range for the pointwise sampling. The wavenumber spectrum of the coarsened mesh is limited to $k/k_0 = 10$, ($k_0 = 2\pi/L$) due to the downsampling. Fig. 3.14 shows the

⁵See Fig. A.1 at page 107 for the coordinates of the cylindrical Kirchhoff's surfaces.

velocity and its spectrum for the same line at a later time step. The spatial velocity distribution appears again to be smooth enough to be well represented by the pointwise extraction as well as by the averaged data. Here, a wavenumber spectrum is obtained, which does not show an aliasing effect regarding both the sampling methods. The aliasing effect due to a pointwise sampling depends strongly

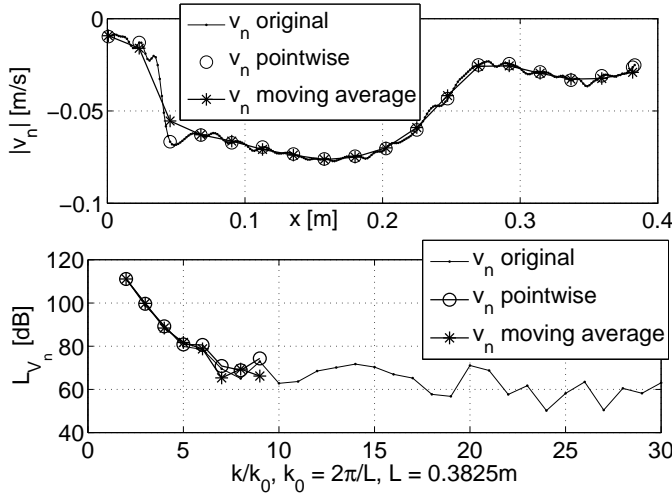


Figure 3.14.: Instantaneous velocity distribution in axial direction x at $t = 0.245s$ for axial line the axial line of the tenth cylinder at $\phi = 0^\circ$, *upper plot*: spatial distribution, *lower plot*: wavenumber spectrum.

on the velocity curve of the originally given data. From Figs. 3.13 and 3.14 can be concluded that the pointwise extraction does not necessarily lead to an aliasing effect. Fig. 3.15 shows the normal velocity distribution along a radial line at the outflow cap. Here, the averaging smooths the original curve, which shows some short wave fluctuations. A direct transform in the wavenumber domain is not possible for the velocity distribution in radial direction, because the mesh is not equidistant in this direction. An increase of the amplitudes of the wavenumber

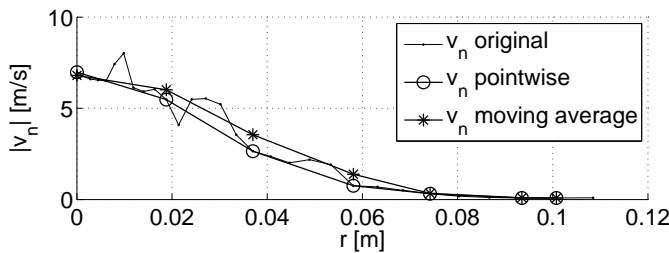
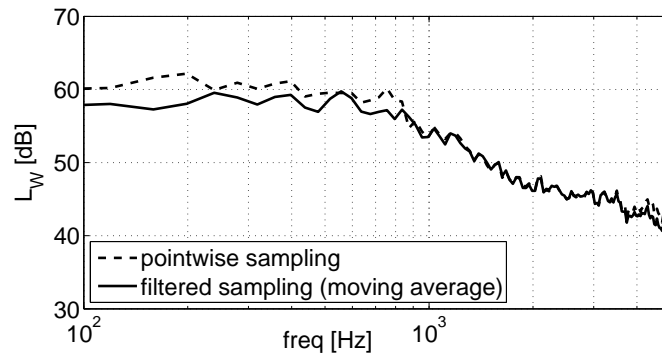


Figure 3.15.: Instantaneous velocity distribution in radial direction r at $t = 0.081s$ for the radial line at $\phi = 0^\circ$.

spectra $V_n(k)$ as seen in Fig. 3.13 can lead to an increased of the radiated sound power. But it is difficult to estimate the general effect on the acoustic radiation because the spatial spectra vary for every time step and every axial node line. A comparison of the sound power based on both sampling techniques is shown

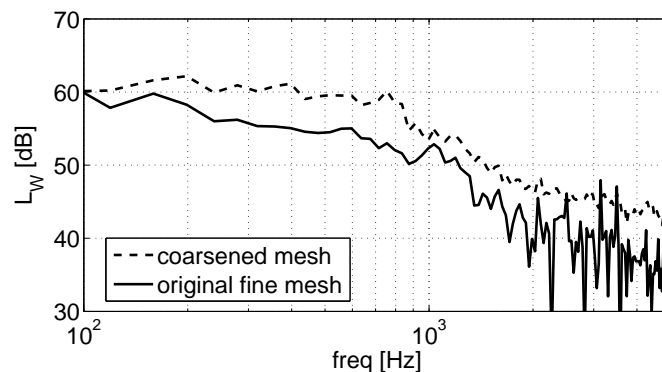
in Fig. 3.16, which presents the radiated sound power of the HD-flame, calculated from the tenth Kirchhoff's surface. Only a slight difference in the sound power spectra due to the different sampling methods can be observed in the lower frequency range.

Figure 3.16.: Radiated sound power of the HD-flame based on a pointwise and a filtered data sampling.



As discussed in Paper IV, the outflow cap of the Kirchhoff's surface mainly determines the amount of radiated sound power. To study the effect of the downsampling at the outflow cap, a BEM calculation with a surface model keeping the original LES mesh at the outflow area but with a coarsened lateral surface was performed. Fig. 3.17 shows the resulting sound power level of the HD-flame using the fine and the coarsened mesh at the outflow area, respectively. The data at the coarsened mesh were sampled using a moving average filter function. According

Figure 3.17.: Radiated sound power of the HD-flame, calculated with a coarsened and the original fine mesh of the outflow area of the Kirchhoff's surface, respectively.



to Fig. 3.17, the radiated sound power is significantly overestimated by using a coarsened mesh of the outflow cap. The effect of the mesh coarsening at the outflow cap is even more obvious, if only the radiated sound power of the outflow cap is considered. Fig. 3.18 shows the sound power, which is radiated only by the outflow cap in case of a coarsened mesh and in case of the original fine LES mesh.⁶ The curves deviate by more than 10 dB. As the results show, the computed

⁶To obtain the radiated sound power of the outflow cap the integration domain S in Eq. (3.6) is

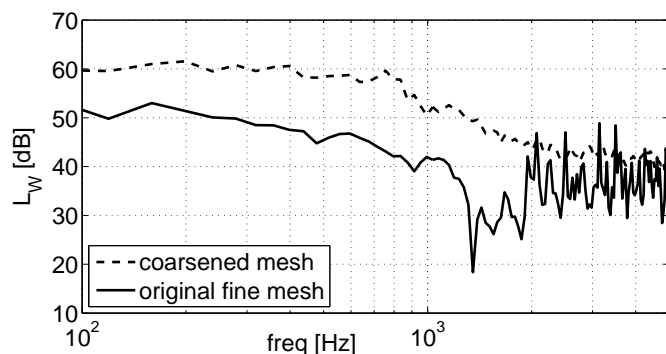


Figure 3.18.: Radiated sound power of the outflow cap of HD-flame, calculated with a coarsened and the original fine mesh, respectively.

radiated sound depends strongly on the used mesh. The sensitivity of the acoustic solutions to the use of fine or coarse grids within a hybrid approach has been also reported by one of our research partners in [80]. The length of coherent structures in fluid dynamics is small compared to the acoustic wavelengths and most of them may not radiate, but to obtain an accurate sound field they need to be well described or filtered out. Otherwise the sound radiation is incorrectly predicted by the hybrid method. The application of the simple moving average does not effectively suppress the occurring aliasing effects. Further research work should be devoted to more elaborated filtering techniques.

3.3.5. Input data correction

The need for a correction of the input data for the BEM calculations occurs at two instances regarding the coupling of the LES and the BEM. First, the artificial turbulence, which is prescribed at the rotational axis of the LES model to invoke turbulence in the low Mach number flow, disturbs the acoustic calculation. This error source can be remedied by setting the velocity at the inflow disc of the cylindrical Kirchhoff's surface to zero. This topic is discussed in Paper I. Second, the velocity distribution at the outflow area of the Kirchhoff's surface represents a significant error source as it is shown in Paper III and Paper IV. Whereas the acoustic intensity in the region of the lateral surface of the cylindrical Kirchhoff's surfaces can be modelled with high accuracy compared to the measured data, the calculated intensity near the outflow area strongly deviates from the measured values (Fig. 9 of Paper III and Fig. 15 of Paper IV). The disturbances, which emanates from the outflow area, are caused by temperature and density distributions, which differ from those of the ambient medium as it is was discussed in Section 3.3.2, or by hydrodynamic velocity fluctuations, which are misinterpreted

limited to the surface of the outflow cap.

as acoustic boundary conditions. The theme of this section is the correction of the velocity data at the outflow area of the Kirchhoff's surfaces. Two approaches are considered, the principal component analysis (PCA) and a splitting technique based on the Helmholtz theorem. The PCA is studied in detail, the splitting technique is merely outlined.

3.3.5.1. Principal component analysis

Theoretical background The Principal Component Analysis (PCA) was first introduced by K. Pearson in 1901 [81]. It is a multivariate data analysis technique, which “is concerned with explaining the variance-covariance structure through a few linear combinations of the original variables” [82, p. 340]. The PCA is a well established evaluation process in economics, psychology, natural sciences and over the years it has also found its way into acoustics. It has been used for acoustic signal identification and interpretation [83, 84] as well as for data reduction with respect to transfer function matrices [85–87].

From the mathematical point of view the PCA represents an eigenvalue problem and it is strongly related to the singular value decomposition or the principal axis transformation. The centred data matrix $\bar{\mathbf{X}}$ is decomposed into a matrix product \mathbf{TP}^t , where \mathbf{P} comprises a set of principal components and \mathbf{T} comprises scores or weights associated with each of the principal components,

$$\bar{\mathbf{X}} = \mathbf{TP}^t + \mathbf{E}. \quad (3.22)$$

Fig. 3.19 illustrates this decomposition. If the number of principal components is chosen as $A = N$, the residue matrix \mathbf{E} vanishes. The data matrix $\bar{\mathbf{X}}$ comprises

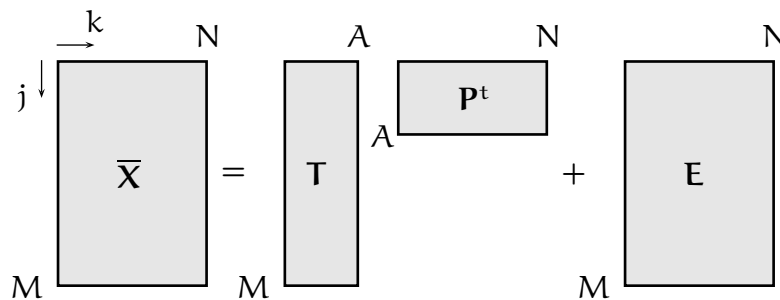


Figure 3.19.: Graphical depiction of the PCA of a matrix \mathbf{X} .

the centred variables \bar{x}_{jk} of the N columns,

$$\bar{x}_{jk} = x_{jk} - \frac{1}{M} \sum_{j=1}^M x_{jk}. \quad (3.23)$$

where x_{jk} are the original data. The principal components are defined as orthogonal eigenvectors of the covariance matrix \mathbf{C}

$$\mathbf{C} = \frac{1}{M} \bar{\mathbf{X}} \bar{\mathbf{X}}^t, \quad (3.24)$$

i.e. they diagonalise \mathbf{C}

$$\mathbf{P}^t \mathbf{C} \mathbf{P} = \mathbf{S}. \quad (3.25)$$

\mathbf{S} is a diagonal matrix, $\mathbf{S} = \text{diag}(\lambda_1, \lambda_2, \dots, \lambda_N)$, where the eigenvalues λ_k are ordered by size, i.e. $\lambda_1 \geq \lambda_2 \geq \dots \geq \lambda_N$. The score matrix \mathbf{T} is set up by the transformed data matrix

$$\mathbf{T} = \bar{\mathbf{X}} \mathbf{P}. \quad (3.26)$$

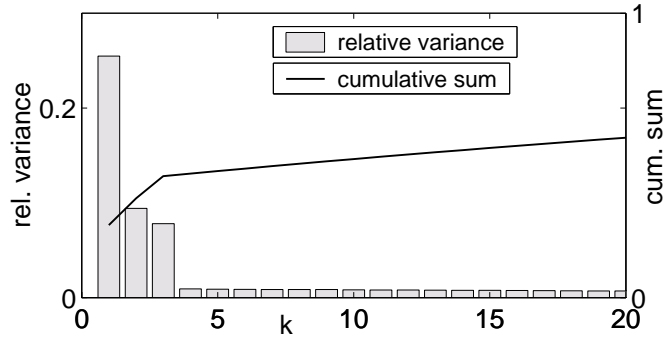
The total variance in the data set $\bar{\mathbf{X}}$ is the sum of all eigenvalues λ_k , each principal component explains a relative variance σ_k^2 of the data set with $\sigma_k^2 = \lambda_k / \sum_{k=1}^N \lambda_k$. The general assumption of the PCA is that a large variance corresponds to an important structure in the data. Hence, principal components with larger associated variances represent an interesting structure of the given data set, while those with lower variances represent noise [88].

PCA within the combustion noise project The main purpose of the PCA is to describe the data set $\bar{\mathbf{X}}$ by a subset of principal components $A < N$ with a low reconstruction error. It can be used for data reduction and classification of data, but the reconstruction modulus offers also the possibility to discriminate patterns in $\bar{\mathbf{X}}$, which are highly correlated. As it is mentioned in [84] “Principal component analysis (PCA) detects collinearity between signals. It is often the case that there are just a few types of underlying behaviour [...]” Concerning combustion noise of open flames a monopole source characteristic is mostly identified as underlying acoustic behaviour [74, Sec. 4], which is also supported by the present measurement analysis of the investigated flames in Section 3.2 of Paper III. Assuming a monopole source characteristic as underlying behaviour of the velocity distribution $v_n(\vec{x}, t)$ on the control surfaces, the coherent signal component of $v_n(\vec{x}, t)$ should be detectable by applying a PCA to $v_n(\vec{x}, t)$. The purely hydrodynamic velocity fluctuations, which are assumed to dominate $v_n(\vec{x}, t)$ on the outflow cap

of the control surfaces, can be considered as uncorrelated. Thus, the correlated signal portions should be separable from the uncorrelated disturbances by a PCA. The use of the separated coherent signal component as input data of the BEM calculation should lead to a higher agreement of measured and simulated sound power level of the investigated flames.

Test example The test example is the velocity distribution at the surface of a vibrating sphere. The velocity distribution at the sphere’s surface is prescribed by a virtual monopole, dipole and quadrupole source with the same amplitude at the sphere’s centre. The sources are driven at slightly different frequencies. The time signal of the velocity at the $N = 294$ nodes of the sphere is sampled at $M = 300$ time steps. Furthermore a random noise signal with about twofold amplitude with respect to the harmonic signals is added. After applying the PCA process to the data matrix $\bar{v}_n^{j,k}$ 294 principal components are obtained. The relative variance corresponding to the first principal components are plotted in Fig. 3.20. Fig. 3.20 represents a “scree plot” [89, Ch.8], a proposed graphical method to determine the significant components. The first three principal components can be clearly recognised as significant components due to their superior large values σ_k^2 . They explain about 42% of the total variance in the data. Fig. 3.21 illustrates the

Figure 3.20.: Eigenvalue spectrum in a relative variance plot. The first three principal components account for 42% of the variance.



ability of the PCA to filter out the coherent structure of $\bar{v}_n^{j,k}$. In Fig. 3.21 the original noisy signal $v_n^{j,k}$, the harmonic signal component of the original signal and the reconstructed signal at one specific node of the sphere are plotted ($1 \leq j \leq M$, $k = 6$). The reconstructed signal is obtained by using only the first three principal components.

In addition, the first three principal components directly correspond to the three different harmonic signal components of $v_n^{j,k}$, which is illustrated in Fig. 3.22. The left side shows the velocity distribution on the sphere’s surface, which corresponds to the three virtual sources at the sphere’s centre. At right side the

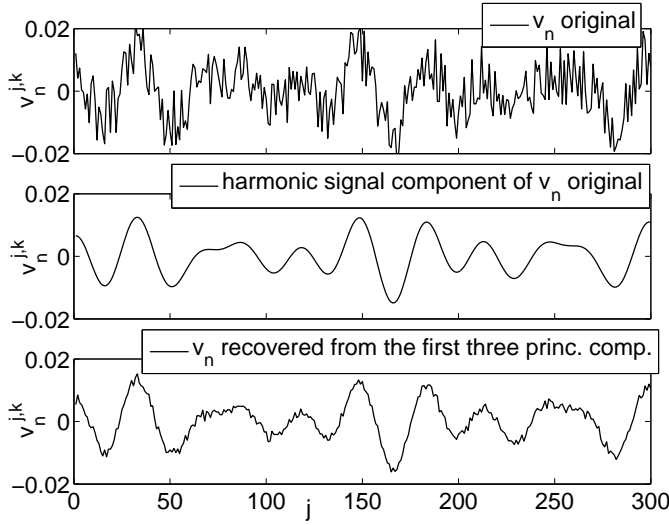


Figure 3.21.: Normal velocity $v_n^{j,k}$ at the k th node of the sphere ($k = 6$).

recovered velocity distributions with respect to only one of the principal components are presented. The association of the principal components with one of orthogonal vibrations of the sphere can be clearly detected, even though the reconstruction of the signal components is not free from defects.

In general, a strong dependence of the performance of the PCA on the noise level of the input data can be observed. In case, the added noise signal is highly increased in amplitude, the harmonic signal components can not be separated from the noise by the PCA. The distribution of eigenvalues λ_k and corresponding relative variances σ_k^2 of the covariance matrix of a purely random sample matrix has been studied by various authors, for instance [90, pp.79-81], [91, 92]. Assuming \mathbf{X} is a large $M \times N$ -matrix with $M \rightarrow \infty$, $N \rightarrow \infty$, of independent, normally distributed random variables $x_{j,k} \sim N(0, 1)$, the limiting probability density function of the eigenvalues of the coherence matrix \mathbf{C} is given by

$$g(\lambda) = \begin{cases} \frac{c}{2\pi\lambda} \sqrt{(\lambda - a)(b - \lambda)} & , a \leq \lambda \leq b \\ 0 & , \text{else} \end{cases} \quad (3.27)$$

with $a = \left(1 - \sqrt{1/c}\right)^2$, $b = \left(1 + \sqrt{1/c}\right)^2$ and $c = M/N$, which is called the Marchenko-Pastur law. The distribution function $G(\lambda)$ is obtained by integration,

$$G(\lambda) = \int_{-\infty}^{\lambda} g(\lambda) d\lambda. \quad (3.28)$$

If the random variables are stochastically distributed as in the test example, it seems sufficient to weight $g(\lambda)$, a and b with the standard deviation σ of the

sample signal to get a good approximation of $G(\lambda)$. According to Eq. (3.27) the eigenvalues are spread within the limits a and b , i.e. the largest eigenvalue approaches b and the smallest approaches a . Using Eqs. (3.27) and (3.28) the N eigenvalues of \mathbf{C} can be approximately predicted. Fig. 3.23 shows the relative variance spectra of the test data, which are superimposed with a random noise signal, in comparison with the relative variance spectra of a purely random data set. The left plot shows the same spectrum as Fig. 3.20, but here all eigenvalues are plotted. Again, the first three principal components can be identified by their

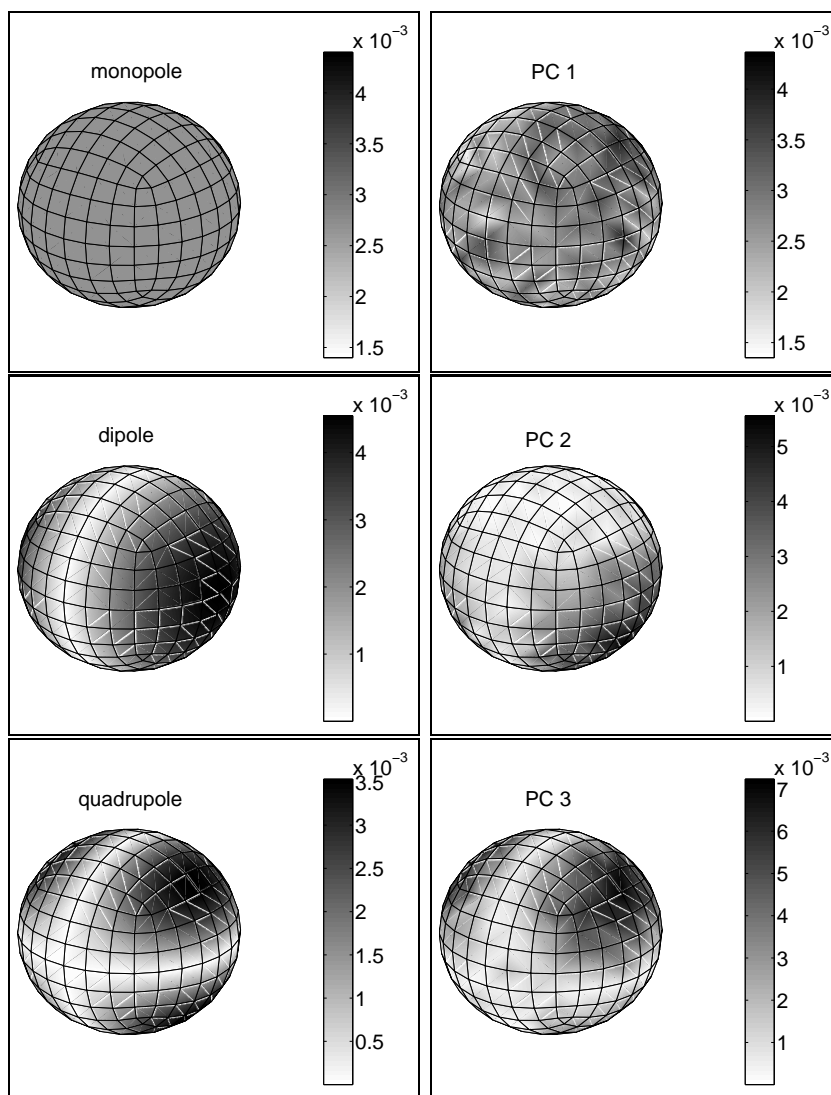


Figure 3.22.: Absolute value of original and reconstructed correlated signal components $|v_n^{j,k}|$ for $j = 1$ ($t = 0$ s).

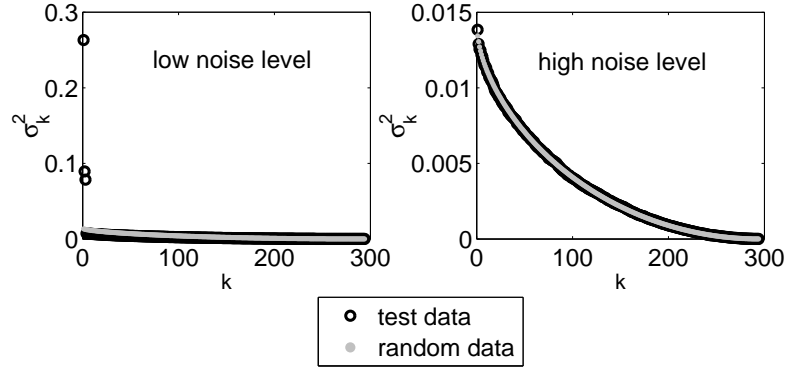


Figure 3.23.: Relative variance spectrum σ_k^2 of the test example data (black circles), superimposed with a low level noise signal and a high level noise signal, respectively. σ_k^2 of the test data set is compared to σ_k^2 of the a purely random sample data set (gray dots).

high relative variances σ_k^2 . The test data set, which was analysed in the right plot, was superimposed with a random data set of a ten times higher level than in the left plot. As it can be seen, the correlated signal within the test data can not be separated by the PCA. The relative variances associated with the test data set are roughly the same as those associated with a purely random data set.

Application of the PCA to the LES flame data Regarding the H3- and HD-flame, the PCA was applied to the LES velocity data on the largest Kirchhoff's surface. The dimensions of the data matrix \bar{X} are 2619×1088 for the H3-flame and 1717×1024 for the HD-flame, comprising the normal velocity at the centres of the elements of the control surfaces at 1717 and 2619 time steps, respectively. Fig. 3.24 shows the relative variances associated to the first principal components of the velocity data of the H3- and HD-flame. The first two or three principal components accounts for about 42% and 53% of the total variance in the data, respectively. The relative variances decline steeply towards higher principal components, the first 20 principal components explain more than 90% of the total variance. Fig. 3.25 shows the complete eigenvalue spectra of the velocity data. Again, it can be clearly recognised, that the major part of the data variance is concentrated in the first principal components. A comparison of Fig. 3.25 with Fig. 3.23 reveals the similarity of the eigenvalue spectra of the flames to that of the low-noise-disturbed test data. However, the comparison is somewhat inconclusive, since the standard deviation σ of the velocity data varies strongly along

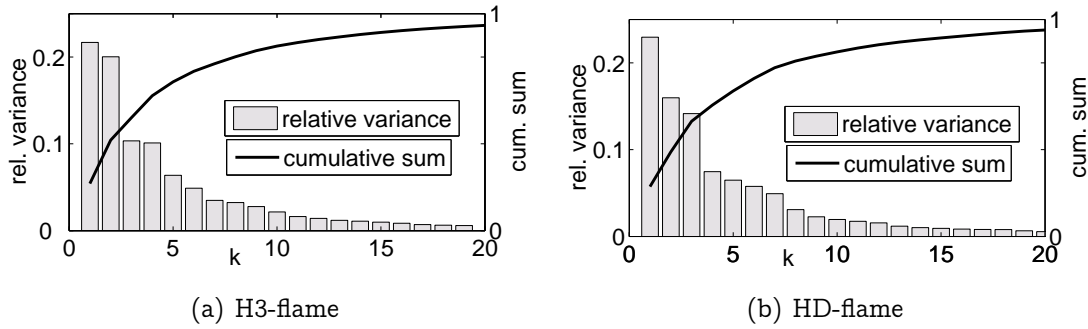


Figure 3.24.: Relative variance plot of the first 20 principal components of the H3-flame and the HD-flame.

the surface of the control surfaces. The highest standard deviation can be found at the outflow cap of the Kirchhoff's surface.

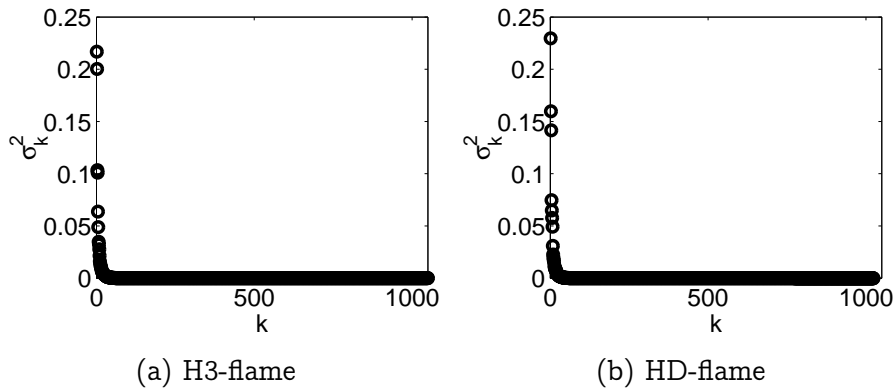


Figure 3.25.: Complete relative variance spectra of the principal components of the normal velocity data of the H3-flame and the HD-flame.

The calculation of the sound power level L_W on the basis of the first principal components of $v_n^{j,k}$ of the two flames yields some surprising results. The radiated sound power of several principal components of $v_n^{j,k}$ is presented in Fig. 3.26. Additionally, the sound power level of the original data set and the measured sound power level are plotted in the same figures. Regarding the H3-flame the first principal component shows a high agreement with the measured sound power level for frequencies above 500 Hz. The second principal components leads to a higher sound power level. As expected, the sound power level due to the added components approaches the sound power level of the original, complete data set. The high agreement of the first principal component with the measured frequency

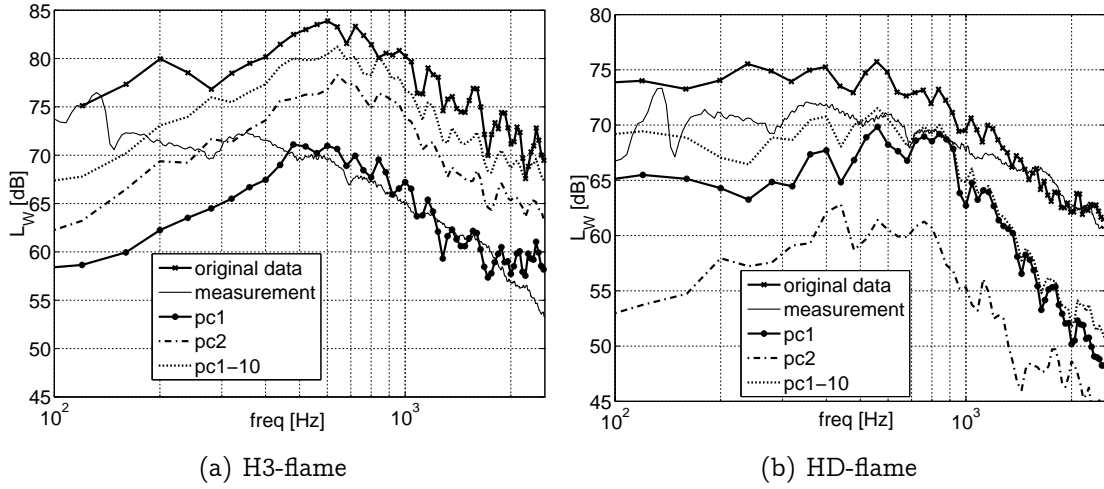


Figure 3.26.: Sound power level L_W of the H3-flame and the HD-flame, based on the original velocity data and on principal components of the velocity data in comparison to the measured L_W .

response of L_W is a promising result, but unfortunately it can not be reproduced with respect to the HD-flame. The right plot of Fig. 3.26 shows the results for the HD-flame. The sound power level due to the first principal component meets the measured one only in a small frequency range from 500 to 1000 Hz. The sound power level, which is based on the sum of the first ten principal components, differs strongly from the sound power level, which is based on the complete data set. In this case the higher principal components largely contribute to the acoustically effective velocity distribution on the control surface, though they explain only a marginal variance of the data set. All in all, though the eigenvalue spectra of the principal components of the two flames have a very similar characteristic, the radiated sound power due to the principal components of the velocity data differ much. General properties of the principal components can not be concluded from these two examples.

Summary The PCA is a very interesting technique for the investigation of large data sets. It provides the possibility to discriminate correlated patterns in a data set as it was shown in the test example. The principal components of the correlated structures can be detected by the extreme values of the associated eigenvalues of the coherence matrix of the data set. The performance of the PCA depends strongly on the signal-noise ratio. A high noise level hides the correlated signal components, so that they can not be separated as principal

components. The PCA was applied to the time domain velocity data on the surface elements of the control surfaces, which enclose the source region of the combustion process. It was applied to both, the H3- and the HD-flame data. The eigenvalues of the coherence matrices are not spread widely: 90% of the total data variance is explained by less than the first 20 of over 1000 principal components. This indicates the existence of correlated signal components within the data set. Nevertheless, the sound power levels calculated by the separate principal components do not agree with the measured sound power level. Whereas the use of the complete, untransformed data set leads to a strong overestimation of the measured sound power level, the transformed data sets also lead to either underestimated or overestimated sound power levels. Additionally, the acoustic behaviour of the principal components differ strongly regarding the two flames. Hence, general properties of the principal components could not be determined. The expectations, that the PCA could provide a separation of the correlated acoustic velocity data from the uncorrelated hydrodynamic perturbations, and that the use of the adjusted velocity data would lead to a higher agreement of the simulated and measured sound power levels of the flames, were not fulfilled. In summary, the application of the PCA to the flame data did not yield advantageous results and the idea was not longer pursued.

3.3.5.2. Splitting technique

The BEM requires acoustic input data on a surface, which completely encloses all acoustic sources. Concerning jets or open flames, the outflow cap of the Kirchhoff's surface intersects perpendicularly with the flow. Since the Mach numbers of the open flames are very small, the contribution of quadrupole sources of the jet flow beyond the closing disc to the overall sound field can be surely neglected. But the flow field of jet diffusion flames is characterised by vortical structures, which grow slowly and maintain their identities over a long distance [93]. The vortices convect downstream with the flow velocity. If these vortical structures pass the Kirchhoff's surface, their velocity fluctuations are sampled as acoustic data and are assumed to propagate into the acoustic far field with sound speed. Fig. 3.27 illustrates this effect. Since the homogeneous wave Eq. (3.1) is only valid in a non-rotational and non-divergent medium, it is not valid in proximity to the outflow cap of the Kirchhoff's surface due to the rotational character of the passing vortices. In the past, several strategies have been proposed to remedy the disturbances due to hydrodynamic fluctuations in the outflow area. Freund et al. [94] suggested the use of an open Kirchhoff's surface, which is now

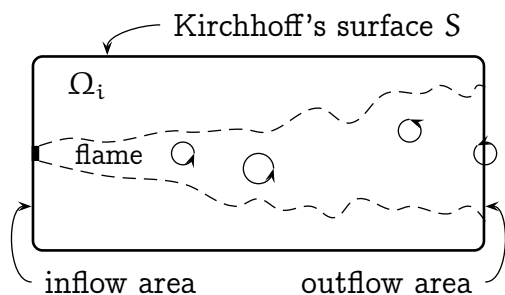


Figure 3.27.: Vortical flow structures pass through the outflow cap of the Kirchhoff's surface. The dashed line defines the area of increased temperature.

a common praxis in jet acoustics and similar studies, e.g. [95]. The main drawbacks of this approach are that a correct solution for the sound pressure is not available at all points in the exterior of the Kirchhoff's surface, and that the radiated sound power can not be determined due to the missing portion of the control surface. Shur [96] applies an averaging over outflow caps to cancel out the slow non-acoustic fluctuation, but a theoretical prove or validation tests for this approach are missing. The third method is the splitting of the flow field into the hydrodynamic part and the acoustical part. For flows in ducts the mode matching strategy [97] is a very successful technique, based on a modal decomposition across neighbouring outflow caps. The acoustic pressure fluctuations at the Kirchhoff's surface are obtained by a least square fit of the CFD results for the pressure fluctuations with the acoustic modes in the duct. In [98] the mode matching method is extended to the case of swirling vortical flows. But the application of this method is restricted to flows in ducts and the ducts can have only slowly varying cross-section. De Roeck [99] developed a promising splitting technique in the time domain for low-Mach-number flows in two dimensions, that is based on the Helmholtz decomposition for vector fields. It is suited for confined as well as for free-field flows and has been verified by some simple test cases.

The splitting technique, which was recently proposed by Piscoya [100] also bases on the Helmholtz theorem. It fits very well the boundary element approach for the acoustic domain and uses the Dual Reciprocity Boundary Element Method (DRBEM). It shall be outlined in the following as an outlook on worthwhile future work.

The Helmholtz theorem is also known as the fundamental theorem of vector calculus [101, § 20]. It states that any vector \vec{u} field in three dimensions, which is sufficiently smooth and decaying at infinity, can be resolved into the sum of an irrotational (curl-free) vector field \vec{u}_1 and a solenoidal (divergence-free) vector field \vec{u}_2 . This decomposition is unique except for a constant component, which

is denoted by \vec{u}_3 and is both irrotational and solenoidal.

$$\vec{u} = \vec{u}_1 + \vec{u}_2 + \vec{u}_3 \quad (3.29)$$

with

$$\text{rot } \vec{u}_1 = 0, \quad (3.30)$$

$$\text{div } \vec{u}_2 = 0, \quad (3.31)$$

$$\text{rot } \vec{u}_3 = \text{div } \vec{u}_3 = 0. \quad (3.32)$$

The irrotational field component u_1 is determined by the gradient of the velocity potential ϕ

$$\vec{u}_1(\vec{x}) = -\nabla\phi(\vec{x}). \quad (3.33)$$

$\phi(\vec{x})$ fulfils the differential equation

$$\text{div } \nabla\phi(\vec{x}) = \nabla^2\phi(\vec{x}) = -\text{div } \vec{u}_1(\vec{x}) \quad (3.34)$$

and with Eqs. (3.30) and (3.32) follows

$$\nabla^2\phi(\vec{x}) = -\text{div } \vec{u}(\vec{x}). \quad (3.35)$$

Eq. (3.35) represents an inhomogeneous Poisson equation. The source term $-\text{div } \vec{u}$ can be determined by an evaluation of the CFD source domain solution for the velocity field. A unique solution of $\phi(\vec{x})$ can be obtained by imposing adequate boundary conditions at the control surface S.

Regarding open turbulent diffusion flames the Mach number Ma of the fluid is very low. As it is shown in [70, p. 167ff] a Mach number $Ma \ll 1$ is one of the constraints for the incompressibility of a flow. In [69, Ch. 1.7.1] the limiting Mach number is specified as $Ma < 0.3$.⁷ The Mach number of the open flames is $Ma \approx 0.1$, so the flow can be assumed as incompressible. Following the argumentation of de Roeck [99], due to this incompressibility it can be assumed that the irrotational field \vec{u}_1 is of purely acoustic nature and represents the fluctuating velocity of the acoustic field \vec{v} ,

$$\vec{v} = -\nabla\phi. \quad (3.36)$$

Since the acoustic field bases on isentropic (adiabatic and reversible) fluctuations of p and ρ , the Navier-Stokes equation of motion reduces to

$$\rho \frac{D\vec{v}}{Dt} = -\nabla p, \quad (3.37)$$

⁷A derivation of this value can be found in [102, p. 178ff].

where D/Dt denotes the substantial derivative with respect to the time t [70, p. 165f]

$$\frac{D\vec{v}}{Dt} = \frac{\partial\vec{v}}{\partial t} + \vec{u} \cdot \nabla\vec{v}. \quad (3.38)$$

Eq. (3.37) represents the Euler equation for an inviscid flow. Additionally, all volume forces have been disregarded. The low Mach number of the flow allows neglecting the convective derivatives in the substantial derivative in Eq. (3.37). Hence, the pressure can be determined by the time derivative of the velocity potential alone,

$$\nabla p \approx -\rho \frac{\partial\vec{v}}{\partial t} = \rho \frac{\partial\nabla\phi}{\partial t} = \rho \nabla \frac{\partial\phi}{\partial t}, \quad (3.39)$$

$$p \approx j\omega\rho\phi. \quad (3.40)$$

Outside the Kirchhoff's surface S the velocity potential $\phi^{(\text{out})}$ fulfils the homogeneous Helmholtz equation, Eq. (3.1). Requiring the continuity of sound pressure and particle velocity at S the boundary conditions are

$$\phi = \frac{\rho^{(\text{out})}}{\rho} \phi^{(\text{out})}, \quad \frac{\partial\phi}{\partial\vec{n}} = \frac{\partial\phi^{(\text{out})}}{\partial\vec{n}}. \quad (3.41)$$

Applying Green's second theorem to Eq. (3.35) yields [103, Ch. 2.5.3]

$$C(\vec{x})\phi(\vec{x}) = \int_S \left(\frac{\partial\phi(\vec{y})}{\partial\vec{n}_y} G(\vec{x}, \vec{y}) - \phi(\vec{y}) \frac{\partial G(\vec{x}, \vec{y})}{\partial n_y} \right) dS - \int_{\Omega_i} b(\vec{y}) g(\vec{x}, \vec{y}) d\Omega_y \quad (3.42)$$

with

$$C(\vec{x}) = \begin{cases} 1 & \vec{x} \in \Omega_i \setminus S, \\ \frac{1}{2} & \vec{x} \in S, \\ 0 & \vec{x} \text{ outside } \Omega_i. \end{cases} \quad (3.43)$$

and

$$b(\vec{y}) = -\text{div } \vec{u}(\vec{y}), \quad G(\vec{x}, \vec{y}) = \frac{1}{4\pi r}, \quad r = \|\vec{x} - \vec{y}\|. \quad (3.44)$$

$G(\vec{x}, \vec{y})$ is the Green's function of the Poisson equation $\nabla^2\phi = -\delta(\vec{x} - \vec{y})$ [103, Ch. 2.2.2]. The integral equation, Eq. (3.42), solves the Poisson equation, Eq. (3.35), in the interior domain Ω_i . The additional volume integral accounts for the inhomogeneous source term of Eq. (3.35). By means of the Dual Reciprocity Boundary Element Method (DRBEM) this volume integral can be expressed as a sum of surface integrals. A detailed discussion of the DRBEM can be found in [104] and in references therein. Finally, a surface integral equation for the

interior and a surface integral equation for the exterior velocity potential are obtained, which are coupled by Eq. (3.41). After the velocity potential at the surface S is received, the normal velocity v_n of the irrotational velocity field can be determined via Eq. (3.36) and used as input data for a BEM calculation. In [100] a numerical test for this splitting technique is presented. In the test case the acoustic relevant velocity field u_1 can be successfully extracted from a total velocity field u . It can be expected that the application of this splitting technique is able to improve the results of the hybrid LES/BEM approach, but this has not been investigated yet. It is the most promising method regarding an appropriate input data correction for the desired coupling of a CFD- and a BEM simulation.

3.4. Application of the CHIEF method

The BEM for exterior problems suffers from the problem of non-uniqueness, i.e. the solution of the surface integral equation is not unique at certain characteristic frequencies, which are related to internal resonances of the corresponding interior problem [24]. Several approaches have been investigated to remedy the non-uniqueness problem. Reviews of different methods can be found in [105–107].

The CHIEF method (Combined Helmholtz Integral Equation Formulation) was first introduced by Schenck [15] to avoid the non-uniqueness of the system of equations at the eigenfrequencies of the interior sound field. Additional collocation points (the CHIEF points) are located in the interior domain of the object, where the interior Helmholtz integral formulation must be satisfied. With this overdetermination the surface HIE and interior HIE are solved simultaneously to enforce the finding of the unique surface solution.

3.4.1. The interior sound field of the cylinders

The efficiency of the CHIEF points depend on their location. The best places are the pressure maxima of the interior sound field modes, the worst places are the nodal lines of the interior modes. The cylindrical Kirchhoff's surfaces, which are used in the hybrid approach have the advantage that the interior sound field can be analysed analytically. Since the exterior boundary problem has a Neumann boundary condition (v_n is prescribed at the Kirchhoff's surface S), the associated interior problem is a Dirichlet boundary problem, i.e. $p = 0$ at S [15]. The derivation of the interior sound field can be found in in Appendix A. In Fig. 3.28 the resulting mode shapes of the interior field are plotted.

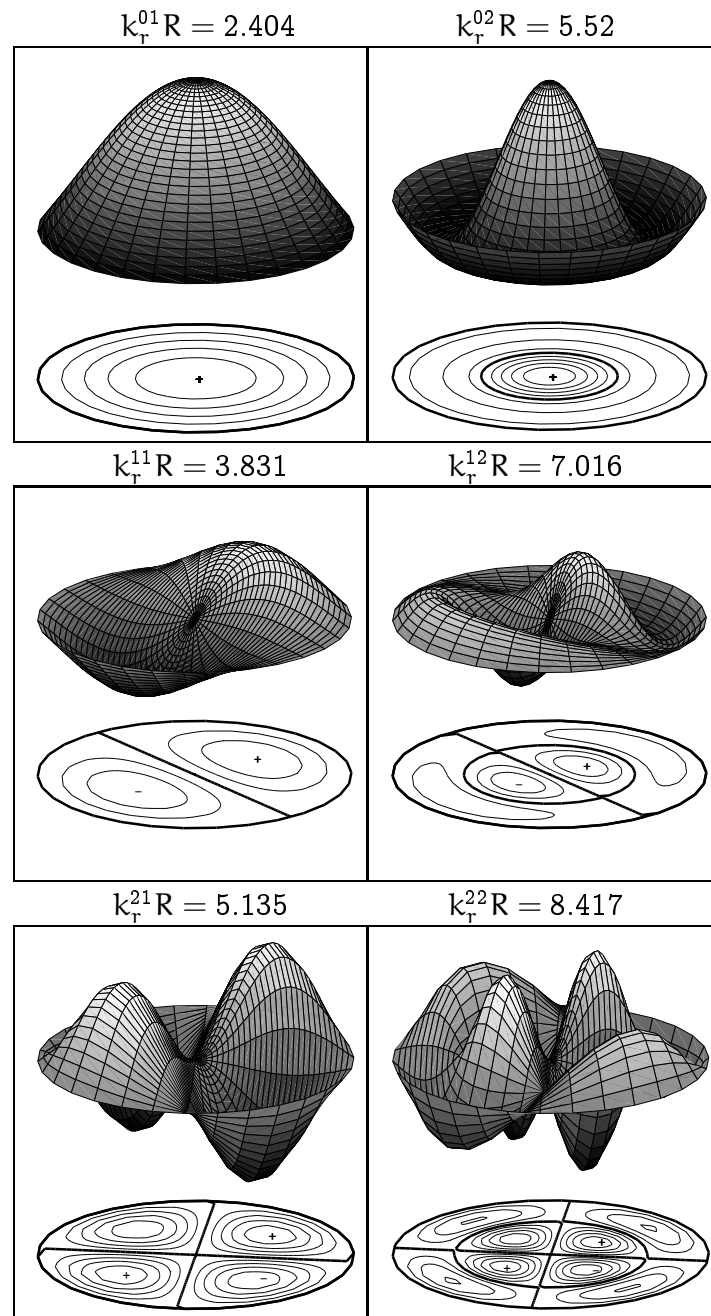


Figure 3.28.: Pressure distribution of the first transverse modes of the sound field in the cylinder with boundary condition $p = 0$. Nodal lines are plotted boldly. The derivation of the sound field solution can be found in Appendix A.

3.4.2. Testing CHIEF point positions

Any CHIEF point located at a nodal line of an interior mode can not remedy the non-uniqueness of the BEM solution, which occurs at this mode. The finding of good position of the CHIEF points is discussed in literature, for example in [15, 22, 106, 108, 109]. In case of an axisymmetric radiator or scatterer, it is recommended in [106] and [109] to place the CHIEF points at the axis of symmetry of a body of revolution, following an corresponding argumentation in [14]. Tobocman [110] obtained good results with a random distribution of CHIEF points in a rigid spheroid scatterer. According to Fig. 3.28 CHIEF points at the axis of symmetry of the cylinders should be only effective for the 0, i-modes, which show a maximum sound pressure value at the axis line. All other modes exhibit a nodal line at the axis of symmetry. It is doubtful that the axis of symmetry is a good place to put the CHIEF points regarding the higher modes.

The effectiveness of the CHIEF method is tested by a constructed substitute problem as proposed in [22] and [111]. At the elements of the tenth cylindrical Kirchhoff's surface of the HD-flame⁸ the normal velocity is prescribed, that would be produced by a multipole source located within in cylinder. Hence, the velocity field on the surface of the cylinder is identical to the field of the multipole source. This normal velocity distribution is used as input data for the BEM calculation. The calculated sound pressure on the surface of the structure as well as in the exterior domain can be directly compared with the analytical solution of the multipole source. The error of the calculation is the surface error E_{surf} or radiation error E_{rad} ,

$$E_{\text{surf}} = \sqrt{\frac{\int_S |p_{\text{analyt}}(\vec{x}) - p_{\text{BEM}}(\vec{x})|^2 dS}{\int_S |p_{\text{analyt}}(\vec{x})|^2 dS}}, \quad (3.45)$$

$$E_{\text{rad}} = \sqrt{\frac{P_{W,\text{analyt}} - P_{W,\text{BEM}}}{P_{W,\text{analyt}}}}, \quad (3.46)$$

with $p(\vec{x})$ as sound pressure at S and P_W as radiated sound power. The test was carried out using a monopole source located at point $\vec{y} = (x_s, y_s, z_s)$ as radiating sound source inside the structure. The fundamental solution of the monopole source in three-dimensional free space is given by Eq. (2.4). Introducing a weighting factor for the fundamental solution of the monopole source, that provides a normal velocity v_a at a fixed distance r_a from the source point location,

⁸Details on the Kirchhoff's surfaces can be found in Section 4.1 of Paper IV.

leads to analytical expressions for the sound pressure and sound power [112, Ch. 2.5.1]

$$p_{\text{analyt}}(r) = r_a^2 v_a \frac{j \omega \rho_0}{1 + j k_0 r_a} \frac{e^{-j k_0 (r - r_a)}}{r}, \quad (3.47)$$

$$P_{W,\text{analyt}} = \frac{\rho_0 c_0}{2} 4\pi r_a^2 \frac{k_0^2 r_a^2}{1 + k_0^2 a^2} v_a. \quad (3.48)$$

The BEM solution for the radiated sound power is given by

$$P_{W,\text{BEM}} = \sum_{i=1}^N \frac{1}{2} \Re\{p_i v_{n,i}^*\} S_i, \quad (3.49)$$

where i is the index of the elements and N is the total number of surface elements.

First, the monopole radiation error was determined for the tenth Kirchhoff's surface of the HD-flame without the usage of any CHIEF point. The monopole source was located at $\vec{y} = (L/2, 0.4805R_{10}, 0)$ with L as length and R_{10} as radius of the cylinder. As shown in Appendix A, Eq. (A.12), the eigenfrequencies of the interior sound field occur at the intersections of the k_x^{mi} and k_x^n -curves. In the upper plot of Fig. 3.29 the graphs of several k_x^{mi} and k_x^n are shown. The middle plot shows the radiation error of the BEM solution without using any CHIEF point. As discussed in [15] the non-uniqueness of the set of equations appears exactly at the eigenfrequencies of the adjoint interior Dirichlet problem. The error of the BEM solution shows distinct peaks at these frequencies. Since the source is located at the centre of the cylinder in x -direction, the m, i, n -modes with $n = 2k$, $k = 1, 2, \dots$, are not excited by the source. In radial direction the source is located close to the maximum of the $1, 1, n$ -mode. The efficiency of three CHIEF points settings was tested: first, the location at the axis of symmetry at $\vec{x}_i = (x_i, 0, 0)$, as applied in [106] and [109]; second, out of the axial centre at $\vec{x}_i = (x_i, -0.4805R_{10}, 0)$; and third, a random distribution. Fig. 3.30 shows the location of ten CHIEF points inside the cylinder for the three cases. The monopole radiation error E_{rad} of the three settings is shown in the lower plot of Fig. 3.29. The CHIEF points at the axis of symmetry can only eliminate the occurrence of the $0, i, n$ -modes as discussed above. They do not effect at all the higher modes with $m > 0$. The CHIEF points out of axis are able to surmount perfectly the non-uniqueness problem. The error does not exceed 5% all over the frequency range. However, the CHIEF points were located opposite to the source, which is the best possible position, because for all modes a maximum sound pressure level can be expected here, see Fig. 3.28. But also the random distribution of the same number of CHIEF points lead to very sufficient results. As a result of this

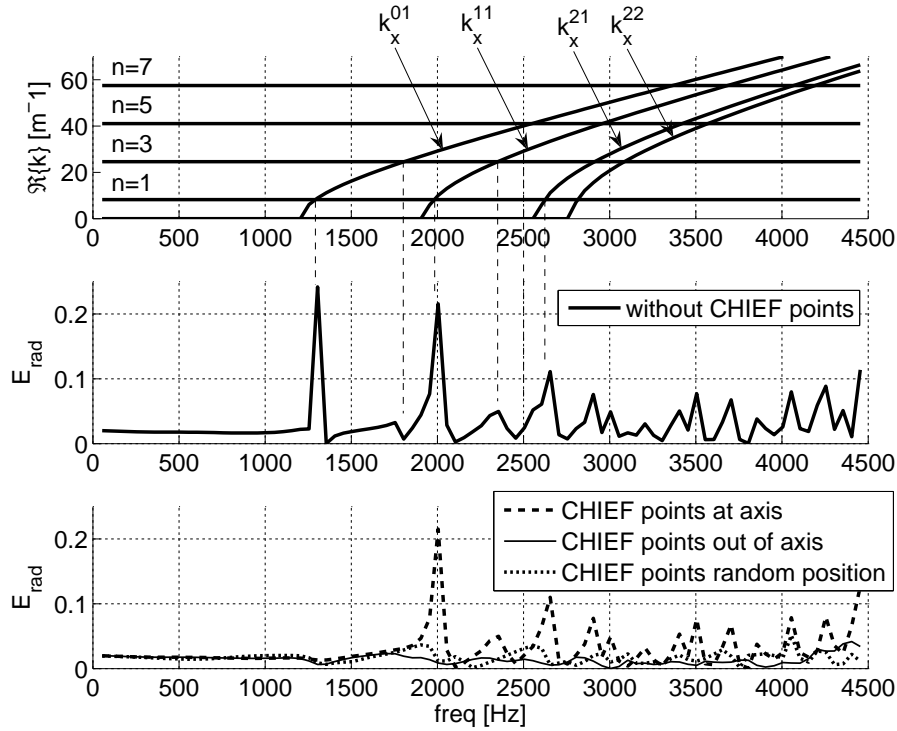


Figure 3.29.: Efficiency of several CHIEF point settings. *Upper plot:* The eigenfrequencies are given by the intersection of k_x^{mi} and k_x^n ; *middle plot:* Radiation error E_{rad} without any CHIEF point; *lower plot:* Radiation error E_{rad} for different CHIEF point positions.

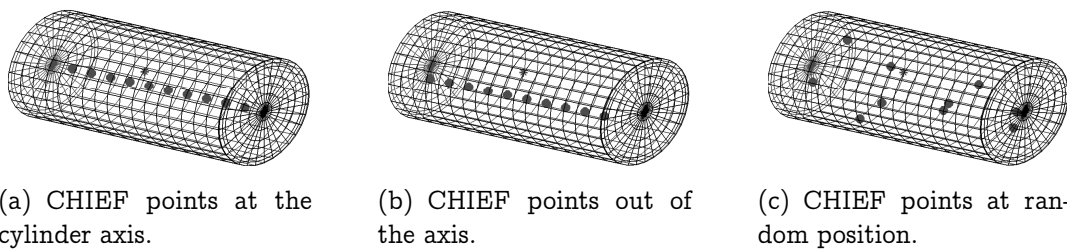


Figure 3.30.: Position of the CHIEF points (\bullet) in the three test settings. The location of the virtual monopole source is marked by an asterisk (*).

study, in all subsequent calculations the second configuration with ten CHIEF points at a line out of axis is used.

3.5. Inclusion of ground effects

In practical situations, the flames are located in a certain environment (room, laboratory, etc). Assuming that side walls and ceilings have some type of acoustical treatment, the scenario will be more similar to a half-space problem than to a free field problem. The presence of the ground can be directly included in the BEM by introducing an appropriate Green's function into Eq. (2.13). This topic is discussed in Chapter 4 at full length. Here, the ideal cases of a rigid ground with infinite impedance ($Z_p = \infty$) or a soft ground with zero impedance ($Z_p = 0$) are considered. The adequate Green's function is given by Eqs. (4.8) and (4.9). A graphical depiction of Eq. (4.8) is given in Fig. 3.31. The effect of the plane is a mirroring of the sound sources, i.e. the total sound field is composed of a direct and a reflected sound field. The height of the Kirchhoff's surface above the plane is $h = 0.1$ m.

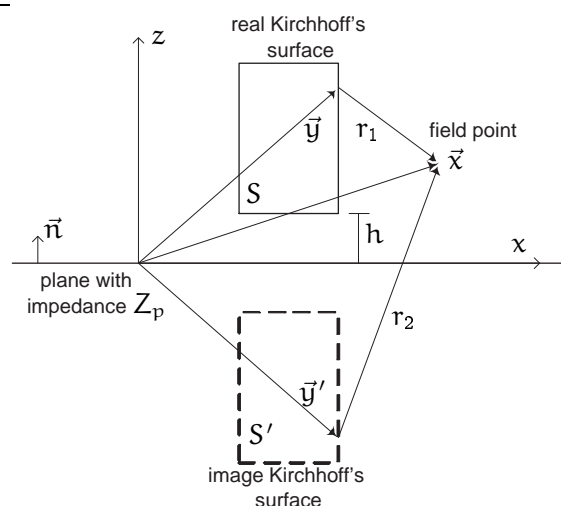


Figure 3.31.: Sketch of real and image Kirchhoff's surface in the presence of a reflecting plane.

Figs. 3.32 and 3.33 show the calculated radiation patterns and sound power spectra of the flame for the three cases: free space, rigid plane and soft plane, as they were obtained by BEM calculations. In the plots of the radiation patterns (Fig. 3.32), the superposition of direct and reflected waves cause a local increase and decrease of the sound pressure compared to the free space case. The presence of a soft or rigid plane leads to a slight decrease or increase of the sound power level in the lower frequency range, respectively (Fig. 3.33). Generally, the influence of the plane on the radiated sound power decreases with the distance h of the flame from the plane. This behaviour is also theoretically derived in Appendix C regarding a monopole source above a soft or rigid plane. The radiated sound

Figure 3.32.: Directivity of the sound field of the HD-flame depending on the characteristics of the plane. The arrow indicates the direction of the flow.

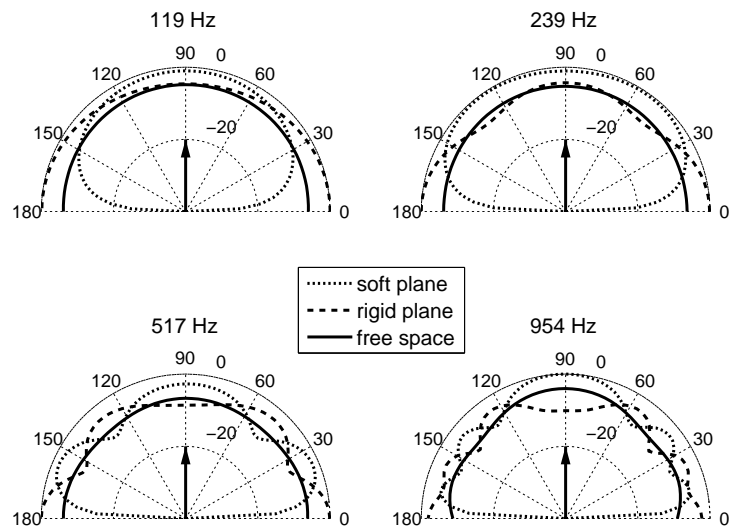
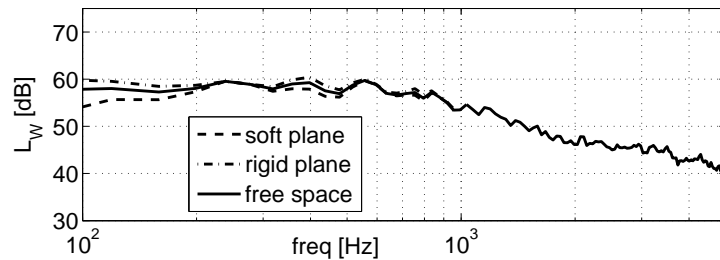


Figure 3.33.: Radiated sound power of the HD-flame depending on the characteristics of the plane.



power of a monopole source above an infinite plane $P_{W,\text{half}}$ and of a monopole source in the unbounded three-dimensional space $P_{W,\text{free}}$ obey the relation

$$P_{W,\text{half}} \approx P_{W,\text{free}} \left(1 + R_p \frac{\sin(k_0 2h)}{k_0 2h} \right), \quad (3.50)$$

where $R_p = -1$ if $Z_p = 0$ and $R_p = 1$ if $Z_p = \infty$. In agreement with this theoretical result, the calculations show that in case $k_0 2h \gg 1$ the influence of an ideal rigid or soft plane on the radiated sound power can be almost neglected. Nevertheless, the directivity of the sound field is strongly affected by the presence of a plane, independently of h , and has to be considered when doing sound power measurements. In the higher frequency range, only a careful scanning of sound intensity or sound pressure at an enveloping surface around the flame yields reliable results due to the mentioned effects.

Chapter 4

A half-space BEM for calculating the sound radiation above an impedance plane

Classically, the BEM is applied to acoustic problems in the free three-dimensional domain. Mostly, the assumption of an unbounded space is a simplification apart from radiation and scattering problems in an anechoic chamber. While for the determination of the radiation characteristics of an vibrating structure the reflections from surrounding boundaries may be neglected, the sound field itself is strongly affected by such reflection and absorption effects. For the simulation of an interior acoustic field, the finite surrounding surfaces can be discretised and the acoustic normal impedance can be prescribed to the surface elements. Regarding outdoor sound propagation, the sound waves are reflected by a ground of infinite extend.

The exterior physical world can be mathematically described as a half-space limited by an infinite plane, provided that the ground is characterized by its normal acoustic impedance. i.e. it is locally reacting. To take the reflections from the ground into account, it is necessary to include the ground into the BEM model. This can be done by a discretisation of a section of the ground into boundary elements. On one hand, a premature clipping of the originally infinite ground leads to erroneous results and on the other hand, a sufficiently large section of the ground leads to a huge set of equations. A more exact way is to include the ground effect by an appropriate Green's function into the BEM model. An appropriate Green's functions describes the sound propagation in the half-space by automatically taking into account the presence of the ground without any further need of a discretisation of the interface.

In this chapter, half-space Green's functions for the sound propagation above an impedance plane are presented and their applicability within a BEM formulation is discussed. The implementation of a suitable Green's function into the BEM code BEMLAB is described and the accuracy and effectiveness of this BEM solution in comparison with an indirect BEM and a discretised impedance plane is investigated. Finally, in the last section of this chapter the simulation of the horn effect of a tyre above a mineral wool layer is presented as a validation test for the developed BEM approach. A very good agreement of the measured and the simulated effect will be shown.

4.1. The half-space Green's function

The core of the Helmholtz-Integral-Equation, Eq. (2.13), is the Green's function $g(\vec{x}, \vec{y})$. As solution of the inhomogeneous Helmholtz equation

$$\nabla^2 g + k^2 g = -\delta(\vec{x} - \vec{y}), \quad (4.1)$$

where ∇^2 is the Laplacian operator and δ the Dirac delta function, it describes the sound propagation between source point $\vec{y} = (x_s, y_s, z_s)$ and observation point $\vec{x} = (x, y, z)$. In case of an unbounded three-dimensional domain, the solution for $g(\vec{x}, \vec{y})$ is

$$g(\vec{x}, \vec{y}) = \frac{e^{-jk_0 r_1}}{4\pi r_1}, \quad (4.2)$$

with $r_1 = \|\vec{x} - \vec{y}\|$. Considering a half-space problem, the three-dimensional domain is separated by an infinite plane S_p into two half-spaces. Since a transmission of energy through the infinite plane is not allowed, the physical domain is reduced to one half-space. The half-space geometry can be seen in Fig. 4.1.

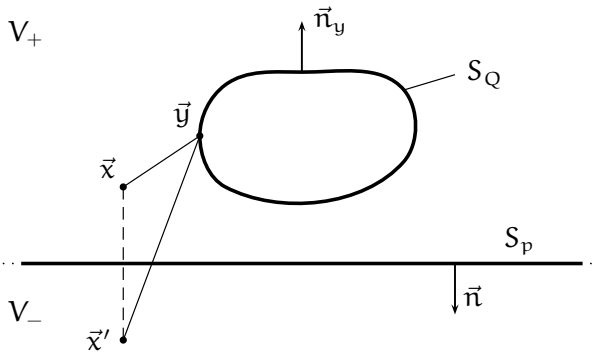


Figure 4.1.: Geometry of the radiation and scattering problem in a half-space.

The acoustical characteristic of the plane S_p is given by its impedance Z

$$Z = \frac{p(\vec{x})}{v_n(\vec{x})}, \quad \vec{x} \text{ on } S_p. \quad (4.3)$$

Using Eq. (2.12) the impedance condition at S_p can be expressed as

$$p(\vec{x}) + \frac{Z}{j\omega\rho_0} \frac{\partial p(\vec{x})}{\partial \vec{n}_x} = 0, \quad \vec{x} \text{ on } S_p. \quad (4.4)$$

Now, a Green's $g_h(\vec{x}, \vec{y})$ function is searched for, which fulfils this given impedance boundary condition on the domain boundary S_p

$$g_h(\vec{x}, \vec{y}) + \frac{1}{j\omega\rho_0} \frac{\partial g_h(\vec{x}, \vec{y})}{\partial \vec{n}_x} = 0, \quad \vec{x} \text{ on } S_p, \quad (4.5)$$

which is called a half-space Green's function. The advantage of a half-space Green's function is that S_p can be excluded from the integration. Regarding Eq. (2.13), the domain boundary of the half-space problem is $S = S_Q \cup S_p$. After inserting a half-space Green's function $g_h(\vec{x}, \vec{y})$ into Eq. (2.13) the integration along S_p yields 0,

$$\int_{S_p} \left[v_n(\vec{y}) \left(Z \frac{\partial g_h(\vec{x}, \vec{y})}{\partial \vec{n}_y} + j\omega\rho_0 g_h(\vec{x}, \vec{y}) \right) \right] dS(\vec{y}) = 0. \quad (4.6)$$

Comparing Eq. (4.5) with Eq. (4.6) shows, that the term in rounded brackets in Eq. (4.6) represents exactly Eq. (4.5), besides that the position of \vec{x} and \vec{y} are interchanged (\vec{y} is now on S_p). Due to symmetry of the Green's function of the wave equation [29, Ch. 5, § 14]

$$g(\vec{x}, \vec{y}) = g(\vec{y}, \vec{x}), \quad (4.7)$$

both expressions are equal. Thus, the integration along S_p can be omitted by using an appropriate half-space Green's function.

In case of a perfectly rigid or perfectly soft plane, the appropriate half-space Green's function is given by

$$g(\vec{x}, \vec{y}) = \frac{e^{-jk_0 r_1}}{4\pi r_1} + R_p \frac{e^{-jk_0 r_2}}{4\pi r_2}, \quad (4.8)$$

with $k_0 = \omega/c_0$, $r_1 = \|\vec{y} - \vec{x}\|$ and $r_2 = \|\vec{y} - \vec{x}'\|$ [113]. \vec{x}' is the image of \vec{x} , mirrored by the infinite impedance plane. The reflection coefficient R_p depends on the normal impedance of the plane Z_p

$$R_p = \begin{cases} +1, & Z_p = \infty, \\ -1, & Z_p = 0. \end{cases} \quad (4.9)$$

Usually, Eq. (4.8) is called the image source ansatz provided that $r_2 = \|\vec{y}' - \vec{x}\|$ with \vec{y}' as the mirrored image of the source point \vec{y} . This ansatz is also discussed in section 17.2.4 of Paper V. Choosing r_2 as $r_2 = \|\vec{y} - \vec{x}'\|$ as used within the scope of this thesis is mathematically more convenient regarding the partial derivative $\partial g(\vec{x}, \vec{y}) / \partial \vec{n}_y$ of Eq. (2.13), though the classical image source ansatz complies more with our understanding of the physical effect of the infinite plane.

An example for an application of Eq. (4.8) within the BEM can be found in Section 3.5, where the dependence of the sound field of an open flame on the ground effect of a rigid and a soft plane is investigated.

In general, the reflection coefficient R_p has to be a constant. Considering only plane waves it is possible to use an angle-dependent reflection coefficient to take an arbitrary impedance of the plane into account [114, Ch. 19.3.2.1],

$$R_p = \frac{Z_p \cos(\theta_0) - 1}{Z_p \cos(\theta_0) + 1}. \quad (4.10)$$

The angle θ_0 is defined as

$$\cos(\theta_0) = (z_s + z) / r_2, \quad (4.11)$$

see Fig. 4.2. For large $k_0 r_2$ the reflected wave in Eq. (4.8) can be simplified to a plane wave and the use of a plane wave reflection coefficient represents a good approximation for $g(\vec{x}, \vec{y})$, but this is mostly not the case considering the solution of the HIE within the BEM. General solutions for the Green's function above an impedance plane are discussed in the next section.

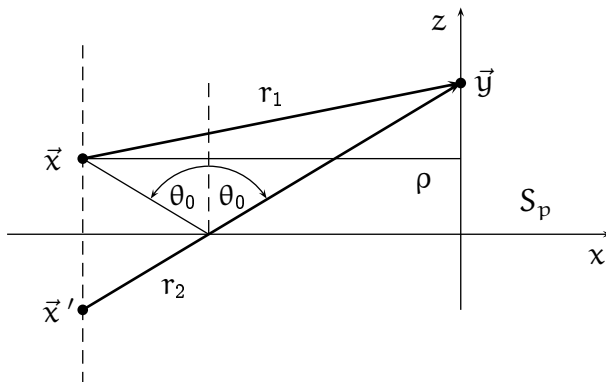


Figure 4.2.: Position of source point \vec{y} and observation point \vec{x} with respect to the plane S_p .

4.2. Green's functions in presence of an impedance plane

4.2.1. Literature review

In the past many researchers published their solutions for the sound propagation above an impedance plane or an interface between two acoustic media. A comprehensive review of the literature can be found in [115, Ch.13.5]. In the following a brief survey of the background of the formulation, which was implemented in the BEM code, will be given.

First Sommerfeld [116, 117] obtained a solution for the reflection of electromagnetic, spherical waves by a homogeneous, flat earth. His solution is discussed in Section 17.2.5 of Paper V and Section III of [118].

In the field of acoustics Rudnick [119] first tackled the problem of the spherical wave reflections by an interface of two acoustic homogeneous media. His work is strongly related to that of Sommerfeld as he also applied a Hankel transform. This work was followed by Lawhead and Rudnick, who published in [120] their farfield solution for the reflections of sound waves from a locally reacting ground. Thirty years later Habault and Filippi [121] followed the Hankel transform tradition and received an exact as well as an approximate solution for sound field reflected by a plane boundary of local and extended reaction. Their surface wave representation [121, Eq. (36)] for a locally reacting surface is also discussed in sections 17.2.5 f. of Paper V. Nobile and Hayek [122] obtained an asymptotic series solution for the reflection problem by a Hankel transform.

A large group of authors applied another technique, which could be called the Fourier transform approach. The incident spherical wave is expanded into plane waves. The reflection of the plane waves can be described by the plane wave reflection coefficient (cf. Eq. (4.10)). Thus, the reflected spherical field is given by an inverse Fourier transform of the reflected plane waves. The Fourier integral is converted into a contour integral in the complex plane and the value of the integral is estimated by a method of steepest descent. The general procedure is described at full length by Brekhovskikh in [123, Ch. 4]. The method was first applied by Weyl [124] in the electromagnetic context as a direct reply to Sommerfeld's work [116]. Ingard [125] first made use of Weyl's approach for the reflection of acoustic waves from a locally reacting plane and obtained an approximate far field solution. Many authors have followed as Wenzel [126], Chien and Soroka [127, 128], Thomasson [129–131], Attenborough et al. [132], Kawai et al. [133] and Filippi [134]. The authors chose different integration paths

or modified steepest descent methods to eventually find an accurate approximate solution mainly for grazing incidence, i.e. for $\theta_0 \approx \pi/2$. With some simplifying assumptions this approach leads to the well-known Weyl/van der Pol formula, which is discussed in the next Section 4.2.2. An exact solution valid for all $k_0 r_2$ and θ_0 is provided by Thomasson [129, Eqs. (32)–(41)], [131, Eqs. (A1)–(A13)], Filippi [134, Eq. (52)] and Habault [135, Eq. (4.7)]. All three authors obtained the same formulation for the reflected wave field.

A few authors have used totally different techniques to obtain the desired Green's function $g(\vec{x}, \vec{y})$. Y. L. Li et al. [136] applied an inverse Laplace transform of the heat conduction equation and got an exact formulation for $g(\vec{x}, \vec{y})$ including a line integral over a Faddeeva function kernel [136, Eq. (21)]. W. L. Li et al. [137] used a power series expansion of the parameter γ to receive an exact Green's function for a positive impedance boundary condition (mass-like impedance) of the plane. Their solution is also discussed in Section 17.2.5 and 17.3.2 of Paper V. More recently Ochmann [118, Eq. (42)] published a solution for the sound field above a plane of arbitrary impedance by a superposition of equivalent sources located at complex source points. Shortly after Taraldsen [138] presented a comprehensive literature review concerning this so-called complex image method together with an identical solution for $g(\vec{x}, \vec{y})$ [138, Eq. (5)]. This complex image solution is derived in Section 17.2.7 of the attached Paper V. It was incorporated into the BEMLAB-code.

4.2.2. Approximate solution for sound propagation close to the ground

The Weyl-van der Pol formula is the most widely used approximate solution for predicting the sound field above a locally reacting ground. It was first deduced from electromagnetic wave propagation theory [123, § 20]. Regarding acoustic wave propagation it follows from the aforementioned Fourier transform approach for finding the Green's function for the sound propagation in a half-space with an infinite plane of finite acoustical impedance. Assuming the time convention $e^{j\omega t}$ it reads

$$g(\vec{x}, \vec{y}) = \frac{e^{-jk_0 r_1}}{4\pi r_1} + [R_p + (1 - R_p)F(\rho_e)] \frac{e^{-jk_0 r_2}}{4\pi r_2}, \quad (4.12)$$

with the boundary loss factor $F(\rho_e)$

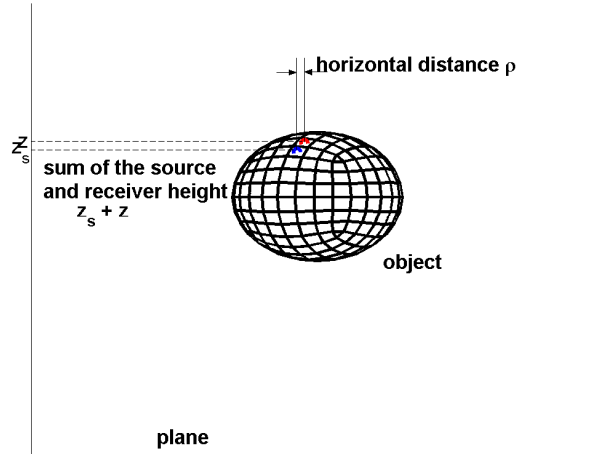
$$F(\rho_e) = 1 - j\sqrt{\pi}\rho_e e^{-\rho_e^2} \operatorname{erfc}(j\rho_e) \quad (4.13)$$

and the numerical distance ρ_e

$$\rho_e = \frac{1}{2}(1 - j)\sqrt{kr_2}(\cos(\theta_0) + Y_p). \quad (4.14)$$

The term $Q = [R_p + (1 - R_p)F(\rho_e)]$ is often called the spherical wave reflection factor. Amongst other applications, the formula is used in non-destructive measurement techniques for the determination of outdoor ground impedance [139, 140]. Its derivation can be found in [119, 127, 132, 141] and [115, Ch.13.5.7]. Eqs. (4.12)–(4.14) are only valid under the following conditions: $k\rho > 1$, $\rho \gg z + z_s$, $k(z + z_s) \gg 1$, $|Y_p|^2 \ll 1$, and $\rho \approx r_2$. That means, it can only be applied for long horizontal distances of \vec{x} and \vec{y} and high frequencies. Additionally, \vec{x} as well as \vec{y} has to be located close to the ground and a high impedance of the ground is required. In view of condition $\rho \gg z + z_s$, which means that the height of \vec{x} and \vec{y} is much smaller than the horizontal distance, it is obvious that the conditions of the Weyl-van der Pol formula can not be fulfilled regarding the collocation process of the BEM. Fig. 4.3 illustrates the corresponding proportions of a boundary element model. Though, the Weyl-van der Pol formula is a very

Figure 4.3.: The requirement $\rho \gg z + z_s$ of the Weyl-van der Pol formula can not be fulfilled within a BEM model.



powerful and convenient solution, it is not suited as core of a BEM formulation.

4.2.3. Exact solutions for the sound propagation above an impedance plane

A BEM formulation requires the use of a highly accurate solution for the Green's function $g(\vec{x}, \vec{y})$, therefore the abovementioned approximate solutions did not come into question for a use within BEMLAB. Available exact solutions are those from Thomasson [129, 131], Habault [121], W. L. Li et al. [137] with restrictions,

Y. L. Li et al. [136] and Ochmann [118]. These solutions are presented in the following. Unless otherwise noted, the time convention $e^{j\omega t}$ is assumed. The nomenclature has been adapted to the one used in this thesis. In a later section three of the solutions are validated by benchmark problems and their applicability within a BEM formulation is discussed.

Thomasson's solution In [129, Eqs. (32)–(41)] the following solution assuming a time dependence $\exp(-j\omega t)$ can be found:

$$g(\vec{x}, \vec{y}) = -\frac{e^{jk_0 r_1}}{4\pi r_1} - \frac{e^{jk_0 r_r}}{4\pi r_2} + \frac{k_0 Y_p e^{jk_0 r_2}}{2\pi} \int_0^\infty \frac{e^{-k_0 r_2 t}}{\sqrt{W(t)}} dt + \frac{1}{4}(1-C)k_0 Y_p H_0^{(1)}(k_0 \rho \sqrt{1-Y_p^2}) e^{-jk_0(z_s+z)Y_p} \quad (4.15)$$

with

$$W(t) = (\cos(\theta_0) + Y_p)^2 + 2j t(1 + \cos(\theta_0)Y_p) - t^2 \quad (4.16)$$

and additional constants

$$C = \begin{cases} +1, & \Re\{\sigma_0\} > 1, \Im\{Y_p\} < 0 \\ -1, & \text{else,} \end{cases} \quad (4.17)$$

$$\sigma_0 = -\cos(\theta_0)Y_p + \sqrt{1-Y_p^2} \sin(\theta_0), \quad (4.18)$$

$$\sigma_1 = -\cos(\theta_0)Y_p - \sqrt{1-Y_p^2} \sin(\theta_0), \quad (4.19)$$

$$\Re\left\{\sqrt{W(t)}\right\} \begin{cases} < 0, & \Re\{\sigma_0\} > 1, \Im\{Y_p\} < 0, t > t_1 \\ > 0, & \text{else,} \end{cases} \quad (4.20)$$

$$t_1 = \Im\{(\sigma_0 - 1)(\sigma_1 - 1)\} / \Re\{(\sigma_0 - 1) + (\sigma_1 - 1)\} \quad (4.21)$$

$$\Re\left\{\sqrt{1-Y_p^2}\right\} > 0 \quad (4.22)$$

$$\cos(\theta_0) = (z_s + z)/r_2. \quad (4.23)$$

The same formulation can be found in [134, Eq. (52)] and [135, Eq. (4.7)]. A critical part of Eq. (4.15) is the so-called surface wave term including the Hankel function in case of spring-like impedances ($\Im\{Y_p\} < 0$). For $\rho = 0$ (perpendicular incidence) the Hankel function is singular and there exists no definite value for $g(\vec{x}, \vec{y})$. $\rho = 0$ corresponds to $\theta_0 = 0$ and after inserting $\theta_0 = 0$ in Eq. (4.19) it can be easily seen, that $\Re\{\sigma_0\} < 0$ for every Y_p since the real part of the

admittance of any physical impedance plane has to be greater than or equal to zero ($\Re\{Y_p\} \geq 0$). That means, $C = +1$ in case of perpendicular incidence. Thus, the Hankel function term does not contribute to $g(\vec{x}, \vec{y})$ in this case. Since the integrand in Eq. (4.15) does not become singular, there are no restrictions for the application of Thomasson's solution.

Habault's solution Habault and Filippi published the following solution [121, Eq. (36)]

$$\begin{aligned}
g(\vec{x}, \vec{y}) &= \frac{e^{-j k_0 r_1}}{4\pi r_1} + \frac{e^{-j k_0 r_2}}{4\pi r_2} \\
&+ \frac{k_0}{4Z_p} (\text{sgn}\tilde{\mathcal{I}}\{Z_p\} - 1) H_0^{(2)}(\alpha\rho) e^{-j k_0 / Z_p \text{sgn}\tilde{\mathcal{I}}\{Z_p\} |z+z_s|} \\
&- \frac{j k_0}{Z_p} (\text{sgn}\tilde{\mathcal{I}}\{Z_p\} - 1) \int_{-z_s}^{\infty} e^{-j k_0 / Z_p \text{sgn}\tilde{\mathcal{I}}\{Z_p\} |z_s+z'|} \frac{e^{-j k_0 r}}{4\pi r} dz' \\
&- \frac{j k_0}{Z_p} (\text{sgn}\tilde{\mathcal{I}}\{Z_p\} + 1) \int_{-\infty}^{-z_s} e^{-j k_0 / Z_p \text{sgn}\tilde{\mathcal{I}}\{Z_p\} |z_s+z'|} \frac{e^{-j k_0 r}}{4\pi r} dz'
\end{aligned} \tag{4.24}$$

with $r^2 = (z - z')^2 + \rho^2$ and $\alpha = k_0 \sqrt{1 - 1/Z_p}$. Both the integrals can be interpreted as line integrals over additional image sources at (x_s, y_s, z') . While the solution for a mass-like impedance of the plane ($\text{sgn}\tilde{\mathcal{I}}\{Z_p\} = 1$) does not become singular, since all sources are located in the non-physical half-space below the impedance plane, the solution for a spring-like impedance of the plane ($\text{sgn}\tilde{\mathcal{I}}\{Z_p\} = -1$) have two singularities in case of perpendicular incidence ($\rho = 0$). In this case the Hankel function becomes singular and the integrand has a singularity at $z' = z$. Physically this singular solution does not exist, i.e. a vertical alignment of source and receiver does not lead to an infinite sound pressure at the receiver. Mathematically both singularities should cancel out each other, but this could not be shown so far. During the collocation procedure within the BEM it cannot be avoided that \vec{x} and \vec{y} are vertically aligned, therefore Habault's solution is only applicable for mass-like impedances of the plane.

W. L. Li's solution In [137, Eq. (24)] W. L. Li et al. presented their solution for mass-like impedances ($\Re\{\gamma\} \geq 0$)

$$g(\vec{x}, \vec{y}) = \frac{e^{-j k_0 r_1}}{4\pi r_1} + \frac{e^{-j k_0 r_2}}{4\pi r_2} - 2\gamma e^{\gamma z_s} \int_{z_s}^{\infty} \frac{e^{-j k_0 r}}{4\pi r} e^{-\gamma z'} dz' \tag{4.25}$$

with $r^2 = (z + z')^2 + \rho^2$. It can be easily shown, that Eq. (4.25) matches Eq. (4.24) for mass-like impedances. It is interesting to see, that the different mathematical techniques used in [121] and [137] lead to the same expression for $g(\vec{x}, \vec{y})$. For spring-like impedances the authors can only find an approximate solution. Thus, again only the solution for mass-like impedances is unrestrictedly applicable concerning a BEM formulation. The presented solution for mass-like impedances has been incorporated in the BEMLAB code. Implementation details as well as a verification test can be found in Section 17.3.2 of Paper V.

Ochmann's solution Ochmann [118, Eq. (42)] presented an exact solution based on the complex image method. The quoted solution Eq. (4.26) follows from applying the time convention $e^{j\omega t}$ to [118, Eq. (42)].

$$g(\vec{x}, \vec{y}) = \frac{e^{-jk_0 r_1}}{4\pi r_1} + \frac{e^{-jk_0 r_2}}{4\pi r_2} + \frac{j\gamma}{2\pi} \int_{-\infty}^0 \frac{e^{-jk_0 r}}{r} e^{-j\gamma z'} dz' \quad (4.26)$$

with $r^2 = (z + z_s + jz')^2 + \rho^2$ and

$$\gamma = jk_0/Z_p. \quad (4.27)$$

The complex image sources under the integral sign are located at complex source points at $(x_s, y_s, -z_s - jz')$. Interestingly, this formulation covers mass-like as well as spring-like impedances of the infinite plane. There is no restriction for the application of Eq. (4.26) except that it is not allowed to have both \vec{x} and \vec{y} directly on the plane. In this case Eq. (4.26) becomes singular because r vanishes at $z' = -\rho$. Ochmann's solution is also derived and discussed in Section 17.2.7 of the attached Paper V, there it can be found as Eq. (17.37).

Y. L. Li's solution Y. L. Li et al. contributed with another exact solution [136, Eq. (21)] to the set of possible Green's functions. Assuming the time convention $e^{-j\omega t}$ it reads

$$g(\vec{x}, \vec{y}) = \frac{e^{jk_0 r_1}}{4\pi r_1} + \frac{e^{jk_0 r_2}}{4\pi r_2} + \frac{j}{k_0} \int_0^{\infty} \left(\frac{k_0}{4j\pi z'} \right) jkY_p e^{jk_0(z' + r_2^2/4z')} w \left(\frac{(z + z_s)\sqrt{j k_0}}{2\sqrt{z'}} + Y_p \sqrt{j k_0 z'} \right) dz', \quad (4.28)$$

where w denotes a complex error function, which is known as Faddeeva function. At a first glance, the integral in Eq. (4.28) seems not to be easier solvable than the previous ones. The authors do not mention any restriction of the solution. Thus, it should also be appropriate to be used within a BEM formulation, but this has not been investigated so far.

4.2.4. Comparison of the exact solutions by benchmark problems

Since it is difficult to show mathematically the equivalence of the different exact solutions for $g(\vec{x}, \vec{y})$, the validity of the solutions are examined by benchmark problems. There are few published data on the sound field due to a point source above an impedance plane with specified acoustical properties, e.g. in [142–144]. In the following the measurement data, which were published by Delany and Bazley in [143] are taken as benchmark test data for the validation of the exact solutions. Delany and Bazley explored the sound field above a mineral wool layer. The sound source was a horn driver connected to a brass tube, whose end was located at a fixed distance z_s above the ground, source and microphone were separated by a horizontal distance ρ , the microphone height z is variable. The distances are measured in wavelengths. The time convention is changed to $e^{j\omega t}$. The parameters variations are listed in Table 4.1. Fig. 4.4 shows the calculated

setup	f [kHz]	Z_p	z_s [λ]	ρ [λ]
A	1	2.02 - 1.47j	1	1
B	2	1.57 - 0.94j	1	2
C	1	2.02 - 1.47j	2	2

Table 4.1.: Measurement parameters.

sound field compared to the measured pressure distribution as sound pressure level L_p , which is defined as

$$L_p = 10 \log_{10} \left| \frac{p(\vec{x})}{p_0} \right|^2. \quad (4.29)$$

Regarding the calculated sound pressure the strength of the sound source is prescribed as $A_{\text{src}} = 1$ N/m and p_0 is set to $p_0 = 2 \cdot 10^{-5}$ Pa. A specification of A_{src} and p_0 is missing in [143].

Numerical evaluation The numerical evaluation of Ochmann's solution (4.26) is described in detail in Section 17.3.3 of Paper V. Since the mineral wool layer has a very low resistance, $\mathfrak{I}\{\gamma\} > 1$, the Gauss-Laguerre quadrature [32, 25.4.45] can be applied for the evaluation of the integral. A substitution of $\eta = -z'\mathfrak{I}\{\gamma\}$ leads to the appropriate form of the integral, which can be found in Eq. (17.90) of Paper V. The definition of the Gauss-Laguerre quadrature is given in Eq. (17.67) of Paper V and in Appendix D.

The solution of Habault, Eq. (4.24), for spring-like impedances of the plane reads

$$g(\vec{x}, \vec{y}) = \frac{e^{-j k_0 r_1}}{4\pi r_1} + \frac{e^{-j k_0 r_2}}{4\pi r_2} - \frac{k_0}{2Z_p} H_0^{(2)}(\alpha \rho) e^{j k_0 / Z_p |z+z_s|} + \frac{j k_0}{Z_p} 2 \int_{-z_s}^{\infty} e^{j k_0 / Z_p |z_s+z'|} \frac{e^{-j k_0 r}}{4\pi r} dz'. \quad (4.30)$$

By substituting $\eta = -(z' + z_s)\mathfrak{R}\{\gamma\}$ the integral in Eq. (4.30) can also be changed into a form, which is theoretically suitable for the Gauss-Laguerre quadrature. But the integrand is strongly fluctuating and a very high number of integration points is needed. Regarding the investigated benchmark problems the integral could not be approximated accurately with the available number of 97 integration points¹. Therefore the integral is approximated by a left Riemann sum, which requires a finite upper limit of the integral. The integrand $\Psi(z')$ can be separated into an enveloping function $\Psi_E(z')$ and an oscillating function $\Psi_O(z')$, $\Psi(z') = \Psi_E(z')\Psi_O(z')$. The envelope reads

$$\Psi_E(z') = \frac{e^{k_0 \mathfrak{I}\{Z_p\}|s+z'|/|Z_p|^2}}{4\pi r}. \quad (4.31)$$

The improper integral is terminated at an upper limit z_0 , where $\Psi_E(z') < 10^{-6}$. The interval $[-z_s, z_0]$ is partitioned into a sufficient number of elements, which was set to $5 \cdot 10^4$.

Since the integral in Thomasson's solution, Eq. (4.15), does not have a fluctuating kernel, Eq. (4.15) should easily be evaluated numerically. After substituting $\eta = k_0 r_2 t$, the integral in Eq. (4.15) can be solved with the Gauss-Laguerre quadrature. The Hankel function term does not have to be evaluated, since $\mathfrak{R}\{\sigma_0\} < 1$ for all investigated parameter variations and receiver heights. Thus, Eq. (4.15) can be very quickly computed.

Y. L. Li's solution, Eq. (4.28), has not been applied to the benchmark problems.

¹Integration points and weights for the Gauss-Laguerre quadrature are listed up to $n = 32$ in [145] or [146]. The determination of integration points and weights for $n > 32$ is described in Appendix D.

Discussion Fig. 4.4 shows the calculated and measured sound pressure levels for the three investigated measurement setups. The measured data were extracted from [143, Fig. 6]. Since the authors did not specify the used reference value p_0 , the measurement curves are translated in such a way, that the calculated sound pressure levels meets the measured ones at $z = 0$. Thus, the quantitative agreement of the calculated and measured curves is rather arbitrary. But the

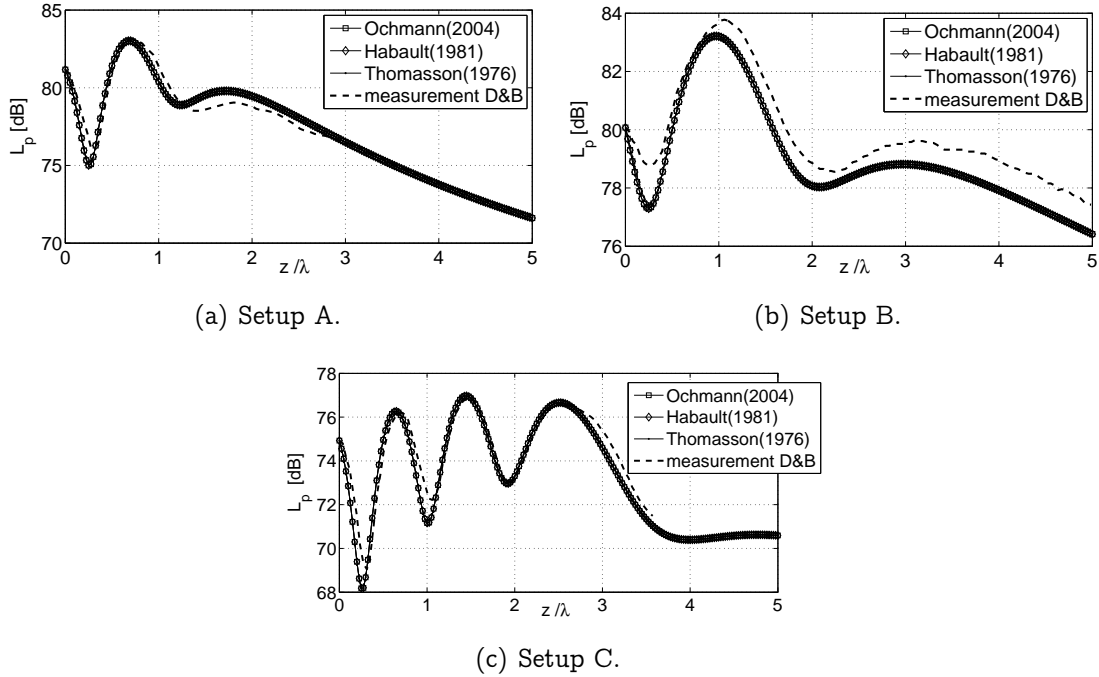


Figure 4.4.: Calculated and measured sound field due to a point source above an impedance plane. Setup parameters are listed in Tab. 4.1. Measurement data are from [143, Fig. 6].

qualitative agreement of the theoretical and experimental results is very good for all three parameter variations. It can also be seen, that all three theoretical solutions do not differ much concerning the investigated setups. While the solutions of Habault and Ochmann (Eqs. (4.24) and (4.26)) lead exactly to the same sound pressure at all receiver locations, the solution of Thomasson yields small deviations. This is shown in Fig. 4.5, which is a magnification of the middle plot of Fig. 4.4 and shows the sound field in proximity to the plane for setup B. Though the values of $k_0 r_2$ are not too small for $z < 0.3\lambda$ ($14.05 < k_0 r_2 < 14.90$) the integral in Eq. (4.15) converges very slow and even the use of up to 97 points for the Gauss-Laguerre quadrature does not lead to a sufficient convergence in

this parameter range. This is contradictory to the statement in [135, Ch.4.1.2], where a 4-point quadrature is mentioned to be enough for values of $k_0 r_2$ “not too small”. Surely, the integral can be evaluated by an adaptive multigrid quadrature or other quadrature techniques, but such techniques are considerably slower than the Gauss-Laguerre quadrature.

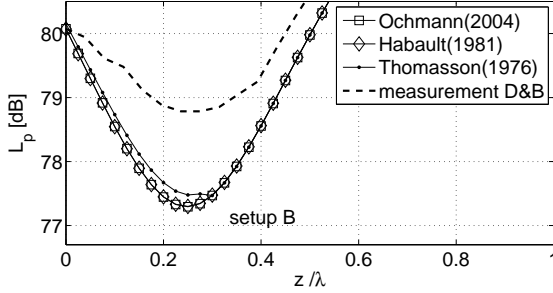


Figure 4.5.: Magnification of Fig. 4.4(b), i.e. calculated and measured sound field close to an impedance plane. Measurement data from [143, Fig. 6].

It can be finally concluded, that all three exact solutions are able to predict the sound pressure distribution over an impedance plane, but the evaluation of the integral is differently complicated. Habault’s solution, Eq. (4.24), is characterized by a strongly fluctuating integrand, which makes the integration very expensive and slow. Along with the mentioned singularity for $\rho = 0$ this solution is not suitable within a BEM formulation. Thomasson’s solution, Eq. (4.15), is not as quick as expected, especially for smaller $k_0 r_2$ the solution needs a more time-consuming treatment. Due to the case differentiations the coding is not as straightforward as for the other solutions. But it does not have any singularity and could be used in a BEM code. Ochmann’s solution, Eq. (4.26), seems to be most appropriate for using within a BEM application. Regarding the investigated benchmark problems it is the fastest solution, the integral converges quickly and the use of the Gauss-Laguerre quadrature yields most reliable results. But as it is discussed in Paper V, this is only the case if $\Im\{\gamma\} > 1$ as in the investigated configurations. For $\Im\{\gamma\} < 1$ a multigrid quadrature has to be applied. The multigrid quadrature is observed to be very stable and accurate, but it is very time-consuming. Possibly, a combination with Thomasson’s solution could be advantageous for some configurations. Ochmann’s solution was successfully implemented in the BEM code BEMLAB. This is thoroughly described in Section 17.3.3 of Paper V. Section 17.3.3 contains a discussion of the characteristics of the integrand, the formulation of its normal derivatives, quadrature solutions as well as a presentation of several test cases for the verification of the correct implementation.

4.2.5. Limiting cases of a soft or rigid impedance plane

The presented Green's functions must approach Eq. (4.8) in case $Z_p \rightarrow \infty$ and $Z_p \rightarrow 0$, respectively. This behaviour will be studied with respect to Ochmann's solution, Eq. (4.26).

Rigid boundary condition of the plane In this case $Z_p \rightarrow \infty$ and $\gamma \rightarrow 0$, cf. Eq. (4.27). Therefore, the last summand in Eq. (4.26) approaches zero

$$\lim_{\gamma \rightarrow 0} \frac{j\gamma}{2\pi} \int_{-\infty}^0 \frac{e^{-jk_0 r}}{r} e^{-j\gamma z'} dz' = 0, \quad (4.32)$$

with $r^2 = (z + z_s + jz')^2 + \rho^2$. The integral in Eq. (4.32)/Eq. (4.26) converges for all parameter settings aside from placing both \vec{x} and \vec{y} on the boundary plane S_p as discussed in Section 17.3.3 of Paper V, Eq. (17.72). Thus, the limiting value of Eq. (4.32) for $\gamma \rightarrow 0$ is zero, and Eq. (4.26) approaches

$$\lim_{\gamma \rightarrow 0} g(\vec{x}, \vec{y}) = \frac{e^{-jk_0 r_1}}{4\pi r_1} + \frac{e^{-jk_0 r_2}}{4\pi r_2}, \quad (4.33)$$

which is the half-space Green's function for a perfectly rigid impedance plane, cf. Eq. (4.8).

Soft boundary condition of the plane This case is not that easy to treat. The soft boundary condition at S_p is defined by $Z_p = 0$ and $\lim_{Z_p \rightarrow 0} \gamma = j\infty$. To obtain the limit of the integrand in Eq. (4.26) for $\gamma \rightarrow j\infty$ the integration by parts is applied:

$$\lim_{\gamma \rightarrow j\infty} \int_{-\infty}^0 f(z')h(z') dz' = \lim_{\gamma \rightarrow j\infty} \left([F(z')h(z')]_{-\infty}^0 - \int_{-\infty}^0 F(z')h'(z') dz' \right) \quad (4.34)$$

with

$$f(z') = 2j\gamma e^{-j\gamma z'}, \quad (4.34 \text{ a})$$

$$h(z') = \frac{e^{-jk_0 r}}{4\pi r}, \quad (4.34 \text{ b})$$

$$F(z') = -2e^{-j\gamma z'}, \quad (4.34 \text{ c})$$

$$h'(z') = \frac{e^{-jk_0 r}(z + z_s + jz')(-j + k_0 r)}{r^3}. \quad (4.34 \text{ d})$$

The limiting value of the first term on the right hand side of Eq. (4.34) is easily obtained

$$\begin{aligned} \lim_{\gamma \rightarrow j\infty} [F(z')h(z')]_{-\infty}^0 &= \lim_{\gamma \rightarrow j\infty} \left[-2e^{-j\gamma z'} \frac{e^{-jk_0 r}}{4\pi r} \right]_{-\infty}^0 \\ &= -2 \frac{e^{-jk_0 r_2}}{4\pi r_2} - \lim_{\gamma \rightarrow j\infty} \left(2e^{-j\gamma(-\infty)} \frac{e^{-jk_0 r}}{4\pi r} \right) \\ &= -2 \frac{e^{-jk_0 r_2}}{4\pi r_2}, \end{aligned} \quad (4.35)$$

since $\lim_{\gamma \rightarrow j\infty} e^{-j\gamma(-\infty)} = 0$.

The integral on the right hand side of Eq. (4.34) can be evaluated by Lebesgue's dominated convergence theorem. Let $\gamma = j a_n$, $a_n \in \mathbb{R}$, $\lim_{n \rightarrow \infty} a_n = \infty$. $F_n(z')$ is a sequence of the function $F(z')h'(z')$ with $\lim_{n \rightarrow \infty} F_n(z') = F(z')h'(z')$:

$$F_n(z') = -2e^{-j a_n z'} h'(z') = -2e^{a_n z'} h'(z'). \quad (4.36)$$

Since $h'(z')$ is bounded and $\lim_{n \rightarrow \infty} e^{a_n z'} = 0$ for $z' \in (-\infty, 0)$ (again provided that \vec{x} and \vec{y} are not located on the boundary plane S_p , i.e. $z + z_s > 0$), the limiting value of the integrand is zero: $\lim_{n \rightarrow \infty} F_n(z') = 0$ for $z' \in (-\infty, 0)$. Furthermore, the sequence $F_n(z')$ is dominated by $h'(z')$ and the integral over $|h'(z')|$ exists:

$$|F_n(z')| = |e^{-a_n z'}| |h'(z')| \leq |h'(z')|, \quad (4.37)$$

$$\int_{-\infty}^0 |h'(z')| dz' < \infty \quad (4.38)$$

Under those conditions, the limit of the integral is

$$\lim_{\gamma \rightarrow j\infty} \int_{-\infty}^0 F(z')h'(z') dz' = \lim_{n \rightarrow \infty} \int_{-\infty}^0 F_n(z') dz' = \int_{-\infty}^0 \lim_{n \rightarrow \infty} F_n(z') dz' = 0. \quad (4.39)$$

Combining Eqs. (4.26), (4.34), (4.35) and (4.39) yields the limiting Green's function of Eq. (4.26) for the soft boundary case as

$$\lim_{\gamma \rightarrow j\infty} g(\vec{x}, \vec{y}) = \frac{e^{-jk_0 r_1}}{4\pi r_1} - \frac{e^{-jk_0 r_2}}{4\pi r_2}, \quad (4.40)$$

which is the half-space Green's function for a perfectly soft impedance plane, cf. Eq. (4.8).

The limiting cases of perfectly soft and rigid boundary conditions of the plane were used as test cases to check the correct implementation of Eq. (4.26) into the BEMLAB-code. The results are presented in Section 17.3.3 of Paper V, cf. Fig. 17.13 and Fig. 17.14.

4.3. Discretised plane versus half-space BEM

The incorporation of an appropriate half-space Green's function (4.26) into a BEM formulation provides the treatment of radiation and scattering problems in presence of an infinite plane, which divides the unbounded three-dimensional space. The only alternative to this approach is the discretisation of a sufficiently large area of the boundary plane to take the influence of the plane on the sound field into account. On the one hand, this leads to a considerable enlargement of the systems matrices and on the other hand, the sufficient the area size is not known *a priori*. In Section 5 of Paper VI a comparison of the two approaches has been presented. A vibrating sphere is located 1 m above an impedance plane with a rather soft normal impedance characteristic, the field points are placed in a row at the same height above the plane with increasing horizontal distance ρ from the centre of the sphere, see Fig. 6 of Paper VI. Fig. 8 of Paper VI shows the boundary element model of the vibrating sphere above a section of the infinite plane, discretised into boundary elements. Since the area is not represented by a closed surface, a direct BEM approach is not suited for this problem. The indirect BEM formulation has not been implemented into the BEMLAB code so far, therefore LMS Virtual.Lab Rev.7B has been used to evaluate the sound pressure distribution at the field points. Fig. 9 of Paper VI shows the error curves of the different approaches. While the error of the half-space BEM solution ($E_{\text{CBEM-GL}}$) is very small, the use of finite plane models does not provide a correct sound field solution ($E_{\text{BEM indirect}}$). In Paper VI the dependence of the simulation error on the size of the discretised areas is demonstrated, in the following the influence of the discretisation level and of an additional symmetry plane is investigated. The tested parameter settings can be found in Tab. 4.2. As already mentioned,

setup	size of the plane [m]	size of the elements [cm]	add. symmetry plane
A	6 × 6	12.50	—
B	12 × 12	12.50	—
C	6 × 6	8.33	—
D	6 × 6	6.25	—
E	6 × 6	12.50	at $z = -14.3$ cm

Table 4.2.: Parameters of the boundary element models utilising a discretised area instead of a half-space formulation.

a comparison concerning the size of the discretised area (A and B) can be found in Fig. 9 of Paper VI. The results with respect to different discretisation levels (A, C and D) are presented in Fig. 4.6. The discretisation in setup A is chosen in such a way that the edge length of the elements is smaller than $\lambda/6 = 14.3$ cm. Obviously, a finer discretisation does not diminishes the simulation error at the field points.

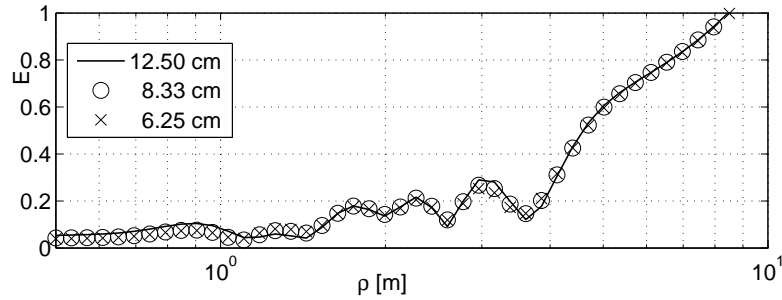


Figure 4.6.: Simulation error depending on the size of the elements.

With increasing distance of the field points to the centre of the sphere, the sound waves, which are radiated by the sphere, can be more and more considered as plane waves with an incident angle $\theta_0 \rightarrow \pi/2$. According to Eq. (4.10), for $\theta_0 \rightarrow \pi/2$ the plane wave reflection coefficient approaches $R_p \rightarrow -1$. Consequently, the idea is not far off to support the finite area by an additional symmetry plane with $R_p = -1$. This corresponds to the creation of a half-space with a perfectly soft plane. Setup E represents this configuration, the soft plane is placed at a distance of $\lambda/2$ beneath the absorbent area. Fig. 4.7 shows the simulation error with and without this additional symmetry plane (A and E). As it can

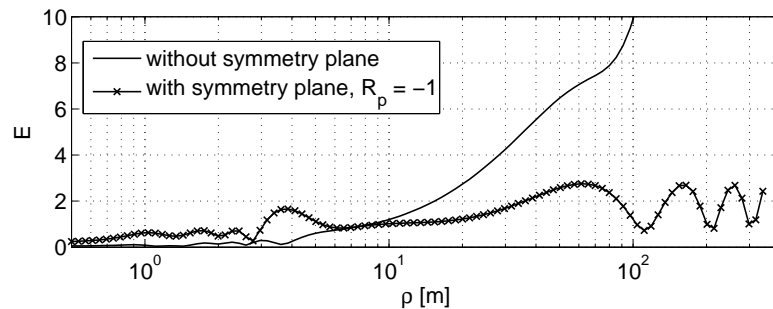


Figure 4.7.: Simulation error depending on the presence of an additional symmetry plane.

be seen, the simulation error at the field points above or close to the absorbent area is increased, the error at the field points outside the discretised area is decreased. In Fig. 4.8 the sound pressure at the field points is presented to clarify the background of the discussed error curves. The graphs of Fig. 4.8 show the

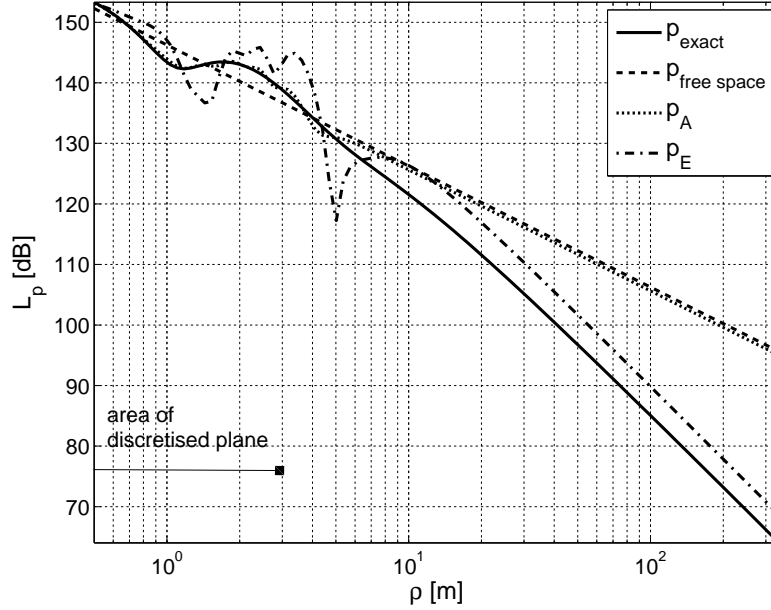


Figure 4.8.: Sound pressure level at the field points with respect to different half-space settings.

sound pressure level at the field points, given by the exact reference solution p_{exact} , by the free-space solution $p_{\text{free space}}$ as well as by the indirect BEM calculations of setup A and E. p_{exact} can be obtained from

$$p_{\text{exact}} = A_{\text{src}} g(\vec{x}_{\text{fp}}, \vec{y}_{\text{src}}) \quad (4.41)$$

with $g(\vec{x}_{\text{fp}}, \vec{y}_{\text{src}})$ as half-space Green's function, Eq. (4.26), A_{src} as source strength and \vec{y}_{src} as the centre of the vibrating sphere. $p_{\text{free space}}$ is defined analogously beside that $g(\vec{x}_{\text{fp}}, \vec{y}_{\text{src}})$ is the free space Green's function, Eq. (4.2).

The field point pressure solution p_A differ slightly from the exact solution as long as the field points are located above the plane (but much more than the half-space BEM solution, cf. Fig. 9 of Paper VI). Outside the absorbent area p_A approaches the free field solution, which is hardly surprising. The additional symmetry plane disturbs the BEM solution for $\rho < 3$ m, thus p_E differs more strongly from the exact solution. But at the distant field points the infinite soft plane emulates the test configuration more than no plane.

All in all, the examples show that it is hardly possible to predict the sound field above an impedance plane by means of a discretised finite area of the infinite plane. The use of an classical direct or indirect BEM formulation without using an appropriate Green's function does not yield accurate results even if a very fine discretisation and a large plane model is chosen.

4.4. Computation of the horn effect

The horn effect is an amplification of the sound field radiated by sound sources close to the contact area of tyre and plane S_p , measured at a field point \vec{x}_{fp} . Close to the contact area the tyre and the surface S_p form a horn-like geome-

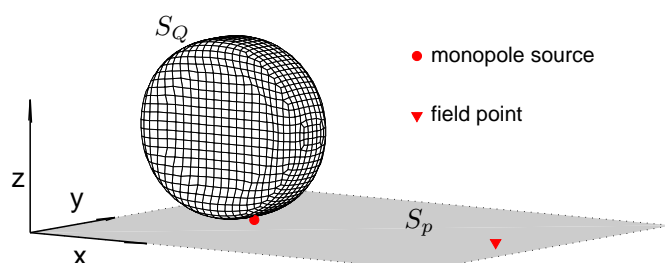


Figure 4.9.: Position of tyre, monopole source and field point in the half-space setting.

try. This geometry influences the radiation characteristic and efficiency of sound sources, which are located in the contact area, i.e. in or close to the centre of the horn [147, 148]. The computation of the horn effect is an ambitious benchmark problem for the developed half-space BEM. On one hand, the horn-like geometry is a numerical complex situation, on the other hand, the frequency response of horn effect is very sensitive to this geometry, and it is strongly influenced by the impedance of the plane S_p [149]. Only a very correct modelling of the scattering effects inside the horn provides a correct prediction of the sound pressure amplification.

4.4.1. Configuration

The amplification due to the horn effect is expressed as

$$\Delta L_H = 20 \log_{10} \left| \frac{p_{ts}(\vec{x}_{fp})}{p_s(\vec{x}_{fp})} \right|. \quad (4.42)$$

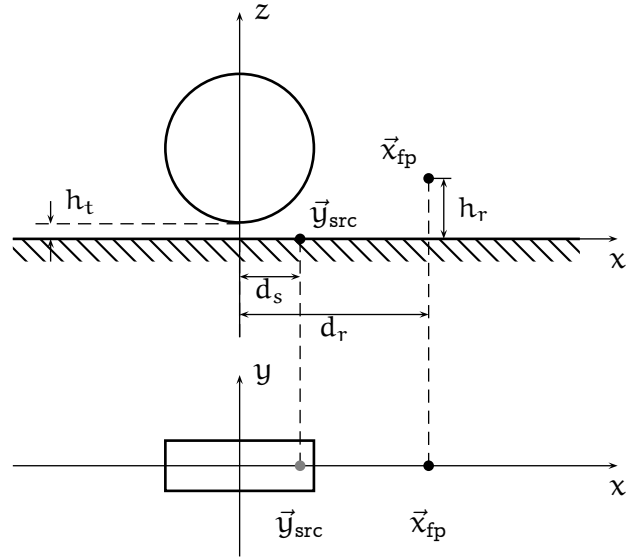
$p_{ts}(\vec{x}_{fp})$ represents the sound pressure at the field point in the presence of the tyre, $p_s(\vec{x}_{fp})$ is the field point sound pressure in the absence of the tyre. The

centre of the horn is located at the point of origin at $(0, 0, 0)$. The source is a monopole source, located at the plane its source strength is $A_{\text{src}} = 1 \text{ N/m}$. The tyre is assumed to have a rigid boundary condition, i.e. the term $\partial p(\vec{y})/\partial \vec{n}_y$ vanishes on S_Q . First, a BEM solution for the horn effect in presence of rigid plane was sought after. After developing a numerical treatment for the complex horn geometry with respect to the more simple rigid boundary condition of the plane, the horn effect in presence of an plane of finite impedance is investigated. The geometrical parameters, which were set regarding the investigations of the horn effect over rigid ground, are listed in Tab. 4.3. A dimensional sketch and the used notation can be found in Fig. 4.10.

d_s	h_t	d_r	h_r
80 mm	0–1 mm	1m	0 m

Table 4.3.: Setup parameters for the investigation of the horn effect over rigid ground.

Figure 4.10.: Horn geometry and dimensioning.



4.4.2. Tyre model

The tyre model does not have any tread pattern, a diameter of 62 cm, and a width of 22 cm. In preliminary studies the most appropriate computational model was identified using LMS Sysnoise. A square and a rounded tyre model profile

was tested, see Fig. 4.11, and the influence of a slight uplift h_t of the tyre was investigated. The reference solution is the measured horn effect with $d_s = 80$ mm and $h_t = 0$ m over rigid ground, provided by [147, Fig. 5]. A raise of the tyre

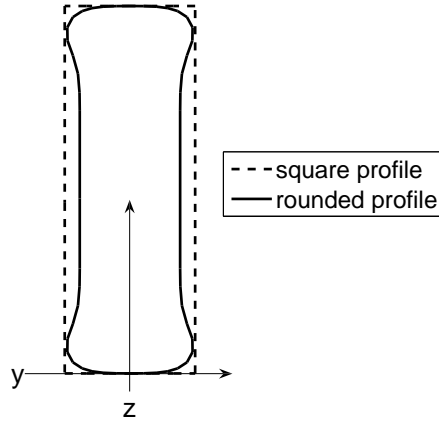


Figure 4.11.: Cross section of the square and rounded tyre model.

is favourable to weaken the near-singularity of the integrand in Eq. (4.26), which occurs if both \vec{x} and \vec{y} are close to infinite plane, i.e. if the combined height $z + z_s$ is very small. As it is discussed in [147], the horn effect is very sensitive to any modifications of the horn geometry. The numerical studies show the same effect. The influence of the configuration parameters can be seen in Fig. 4.13. The upper plot shows the strong influence of the height of the tyre over the plane. Only a few millimetres significantly change the amplification characteristic. For this study the square shaped tyre was used. The middle plot shows a comparison of the horn effect of the rounded and the square shaped tyre. The tyre with the square cross section leads to a distinct overestimation of the amplification level ΔL_H . In this variation both types of tyres were raised by 1 mm. In the lower plot the influence of the surface discretisation on ΔL_H is presented (rounded profile, $h_t =$

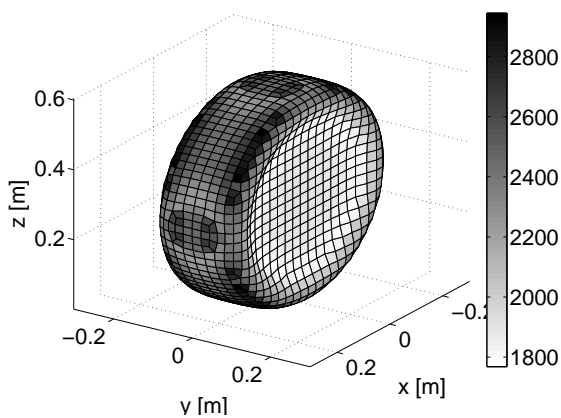


Figure 4.12.: Maximum frequency of the surface elements of the tyre model with 1474 elements.

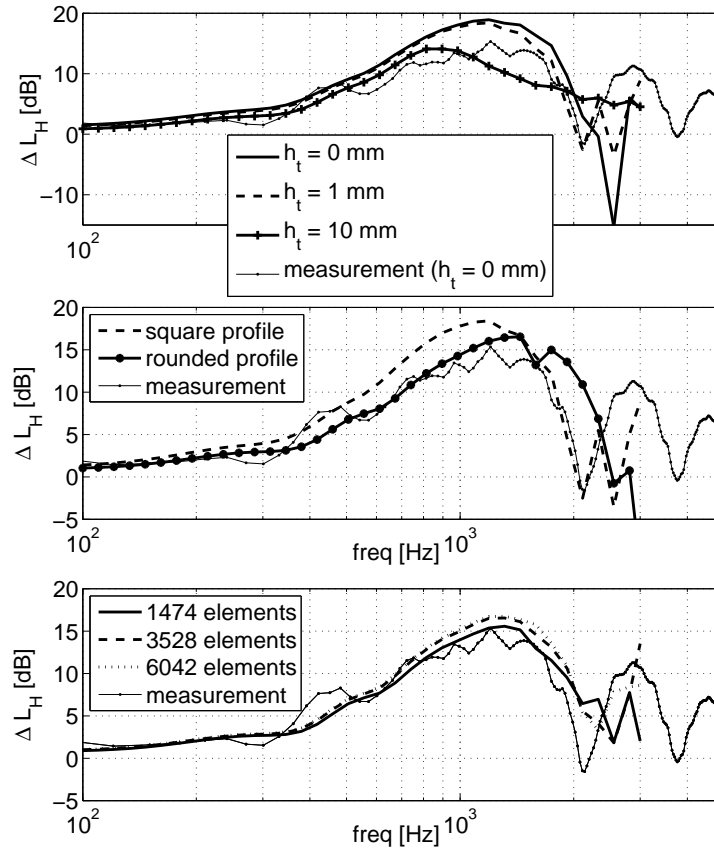


Figure 4.13.: Dependence of ΔL_H on the height of the tyre over the rigid plane (*upper plot*), on the profile of the tyre ($h_t = 1$ mm) (*middle plot*) and on the discretisation of the tyre surface ($h_t = 1$ mm) (*lower plot*).

1mm). Below 2 kHz the frequency responses do not differ significantly regarding the three different models. Above 2 kHz the curves start to diverge. The most appropriate discretisation for the frequency range above 2.5 Hz is the one with 6042 elements, but in the lower frequency range also the small model with 1474 elements is sufficient. As a result of these numerical studies, in the following investigations the rounded tyre model with 1474 elements, raised by $h_t = 1$ mm, has been used. Fig. 4.12 shows the maximum frequency of the surface elements of this tyre model, i.e. the size of the elements is sufficient up to the indicated frequency according to the six-elements-per-wavelength rule. As it can be seen, the belt of the tyre is finer discretised as its side walls. In general, the presented tyre model is suited for calculations up to 2000-2500 Hz.

4.4.3. Numerical treatment of the horn geometry

The BEMLAB-code uses a rough but fast one point integration for the evaluation of the discretised integral equation on S_Q . Regarding the surface area close to plane, this approach is not sufficient, since in this area the “narrow gap” problem is encountered. Similar to the problem of very close boundary surfaces, such as narrow gaps or very thin structures, a near-singularity of the kernel functions occurs due to a very small distance r_2 in the second term of Eq. (4.8) and Eq. (4.26). The first approach was a refinement of this surface area until the element size matches the distance from its centre to the plane. The resulting surface mesh of the tyre can be seen in Fig. 4.14. The figure shows the sound pressure

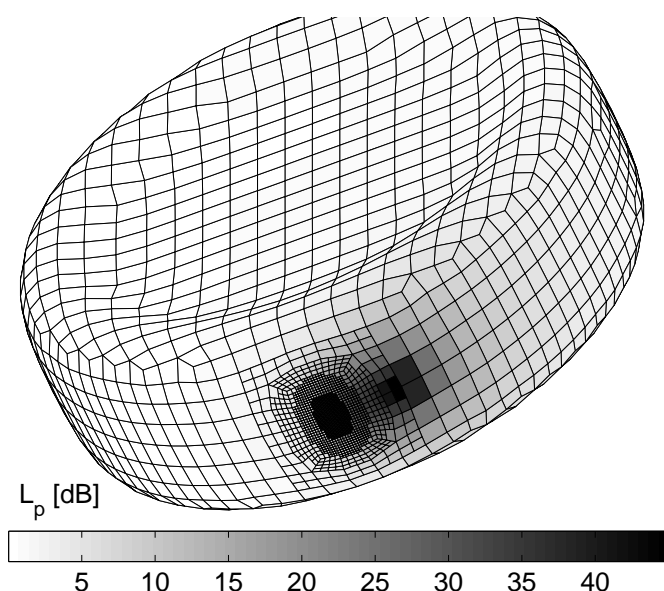
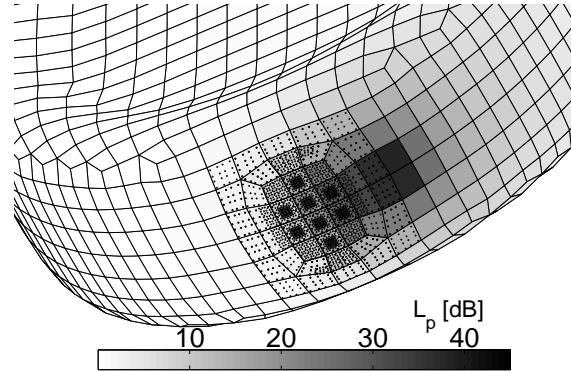


Figure 4.14.: L_p on the refined surface mesh of the tyre at 985 Hz. The tyre is seen from the bottom.

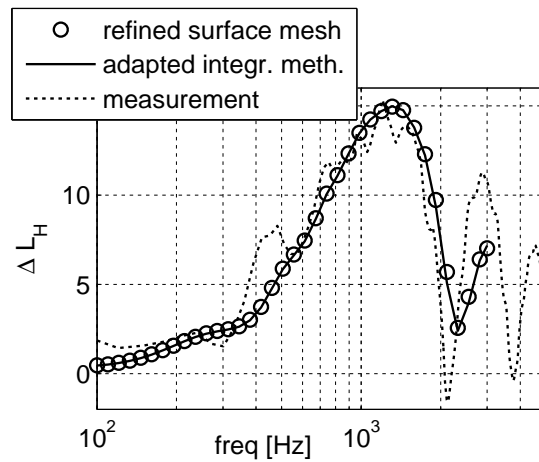
level distribution (L_p) on the surface of the tyre at 985 Hz. Unfortunately this approach leads to a doubling of the total number of elements. Second, we applied an *adapted* integration method, proposed by Cutanda Henríquez and Juhl in [150, 151]. Each surface element is subdivided into intervals proportional to the relative distance between the centre of the element and the plane. After assigning Gauss-Legendre integration points to the element subintervals, the values of $g(\vec{x}, \vec{y})$ and $\partial g(\vec{x}, \vec{y})/\partial \vec{n}_y$ can be determined as a sum of the subinterval values. The total number of elements remains the same as for the one-point-integration. The resulting distribution of integration points at the critical surface area of the tyre is shown in Fig. 4.15. While the finer mesh allows a higher resolution of the sound pressure distribution on the surface of the tyre, the field point pressure in

Figure 4.15.: L_p at the surface mesh of the tyre at 985 Hz. The Gauss-Legendre integration points, resulting from the adapted integration method, are plotted as black dots.



1 m distance from the centre of the horn can be modelled very well with both approaches for $d_s = 80$ mm and $h_t = 1$ mm as it is shown in Fig. 4.16. The resulting amplification level ΔL_H does not differ regarding the two methods, though the adapted integration method is considerably less time and memory consuming. By applying the adapted integration method also to the field point evaluation, it is possible to interchange the position of \vec{x}_{fp} and \vec{y}_{src} as it was done during the measurements. Regarding the measurements this reciprocity principle was used for practical reasons. It is also advantageous to a BEM simulation. Whereas a variation of the position of the source d_s requires a separate calculation for each source position, placing several \vec{x}_{fp} at different d_r in the horn and \vec{y}_{fp} in front of the tyre allow the determination of the amplification ΔL_H for all variations by one single BEM calculation. Due to reciprocity, ΔL_H is not affected by the exchange of source and receiver. Fig. 4.17 shows the amplification ΔL_H for the receiver positions $\vec{x}_{fp} = (d_r, 0, 0)$ with $d_r = 10, 20, 40, 80$ mm and the source position $\vec{y}_{src} = (1\text{m}, 0, 0)$. In general, the computational results show an excellent agree-

Figure 4.16.: Amplification due to the horn effect of a tyre above rigid ground calculated with the refined tyre model and the adapted integration method on the basis of element subdivision. Measurement data from [147, Fig. 5].



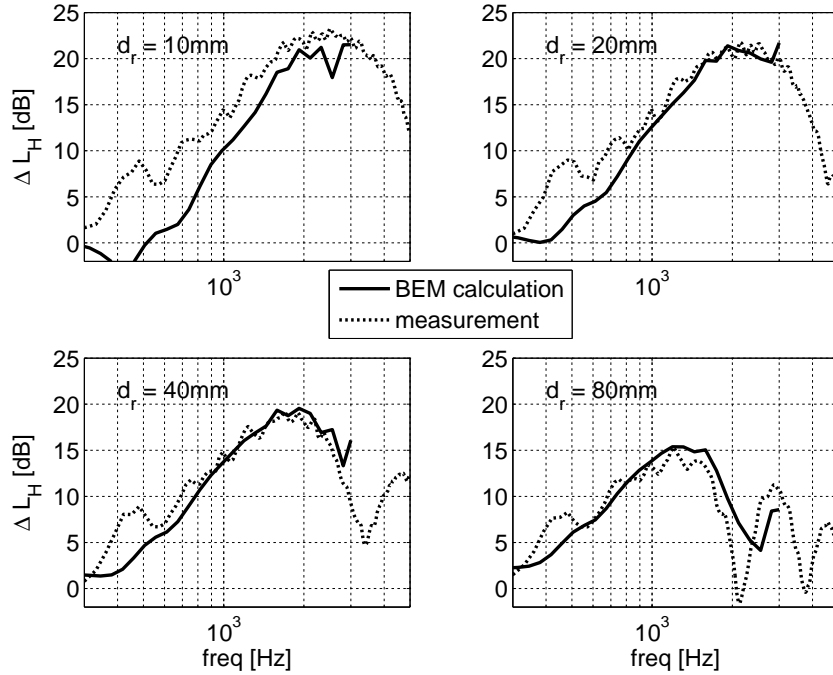


Figure 4.17.: Amplification due to the horn effect of a tyre above rigid ground for different receiver positions. Measurement data from [147, Fig. 5].

ment with the measured frequency response of ΔL_H . Only the case $d_r = 10$ mm is a critical configuration due to extreme proximity to the horn centre.

4.4.4. Influence of the impedance plane

Considering Eq. (4.26) the most expensive step is the evaluation of the improper integral for every matrix coefficient of \mathbf{H} and \mathbf{G} . For some configurations the very fast Gauss-Laguerre quadrature can be applied to solve the integral, otherwise the adaptive multigrid quadrature has to be used, which provides reliable results for all possible configurations, but is much slower (cf. Paper V, sec. 17.3.3). The usage of the Gauss-Laguerre quadrature depends mainly on γ and the combined height of \vec{x} and \vec{y} , $z + z_s$. Generally, the application of the Gauss-Laguerre quadrature is restricted to configurations with $\Im\{\gamma\} > 1$.

In the following a very soft rigidly-backed layer with an effective flow resistivity of $R_{\text{eff}} = 20$ kPas/m² is chosen as impedance plane. The height of the layer is 7 cm. Impedance and γ , respectively, of such a layer can be obtained by the impedance model of Delany&Bazley [152]. Fig. 4.18 shows the contour plot

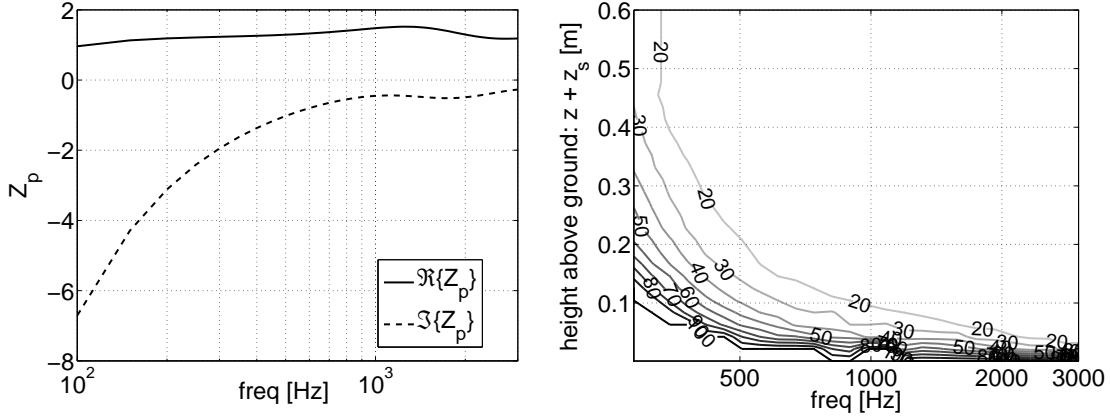


Figure 4.18.: *Left plot:* Z_p of a rigidly backed layer of $R_{\text{eff}} = 20 \text{ kPas/m}^2$ and a height of 7 cm. *Right plot:* Contour plot of the necessary number of integration points to solve the integral in Eq. (4.26) with the Gauss-Laguerre quadrature depending on frequency and the combined height of \bar{x} and \bar{y} with respect to the soft impedance layer.

of necessary integration points of the Gauss-Laguerre quadrature depending on frequency and combined height $z + z_s$. As it can be seen, small heights of \bar{x} and \bar{y} and low frequencies are very unfavourable combinations regarding the application of the Gauss-Laguerre quadrature. In case, the number of integration points exceeds 97, the kernel functions have to be evaluated by the multigrid quadrature. The evaluation of the matrix coefficients is the bottleneck of a BEM calculation including an impedance plane. While the calculation of one frequency step in case of a rigid plane takes around 0.3 minutes, it can take hours in case of a finite impedance of the ground.

Fig. 4.19 shows the resulting amplification due to the horn effect of a tyre above a rigid plane and above the soft impedance layer. The amplification levels ΔL_H differ significantly. In case of the impedance layer, the frequency of maximum amplification is shifted to lower frequencies and the total amplification level is dramatically reduced.

4.4.5. Validation of the model by measurement data

This section presents a validation of the BEM simulation of the horn effect in presence of an impedance plane by measurement data. The measurements were done by F.-X. Bécot and published in his PhD thesis [149, Ch. 4]. A series of

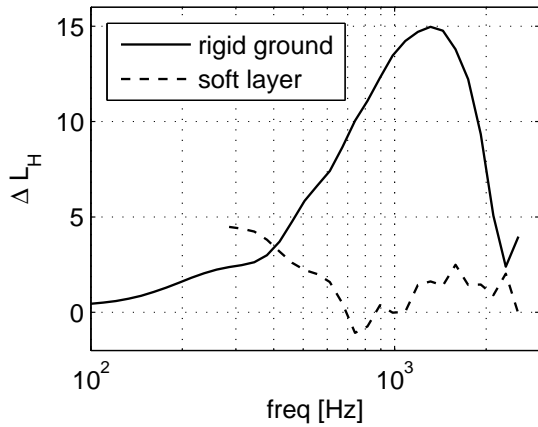


Figure 4.19.: Amplification due to the horn effect of a tyre over rigid ground and over a very soft impedance layer (7cm mineral wool, rigidly backed, $R_{\text{eff}} = 20 \text{ kPas/m}^2$).

four measurement setups have been selected as validation basis for the BEM simulation. In Tab. 4.4 the measurement parameters can be found (cf. Fig. 4.10 for the dimensioning). The impedance plane is represented by a rigidly-backed

setup	h_t [cm]	d_s [cm]	d_r [cm]	h_r [cm]
a	1.85	4.2	98	19.7
b	1.85	18.2	98	19.7
c	0.8	4.2	48	4.7
d	0.8	12.2	48	4.7

Table 4.4.: Parameters for the measurements of the horn effect above an impedance plane.

mineral wool layer of thickness 1.6 cm and $R_{\text{eff}} = 124 \text{ kPas/m}^2$. Fig. 4.20 shows the calculated and measured amplification ΔL_H of the four setups. The predicted amplification matches the measured frequency response very well. The measured curve shows more fluctuations but this might be due to a reverberant measurement environment or the finite size of the real mineral wool layer. The main amplification characteristic of the given setting can be modelled correctly. The calculation was limited towards the lower frequency range due to the increasing computational effort. Unfortunately a rather stiff impedance layer was used in the measurements. Therefore, the condition $\mathcal{I}\{\gamma\} > 1$ is only fulfilled above 700 Hz. i.e. below 700 Hz the Gauss-Laguerre quadrature can not be applied for the determination of the matrix coefficients at all. But using only the multigrid quadrature leads to a computing time of around 40 hours per frequency step. For setup “b” the amplification level at the missing frequencies have been determined

by such tedious calculations. The whole frequency response of ΔL_H can be found

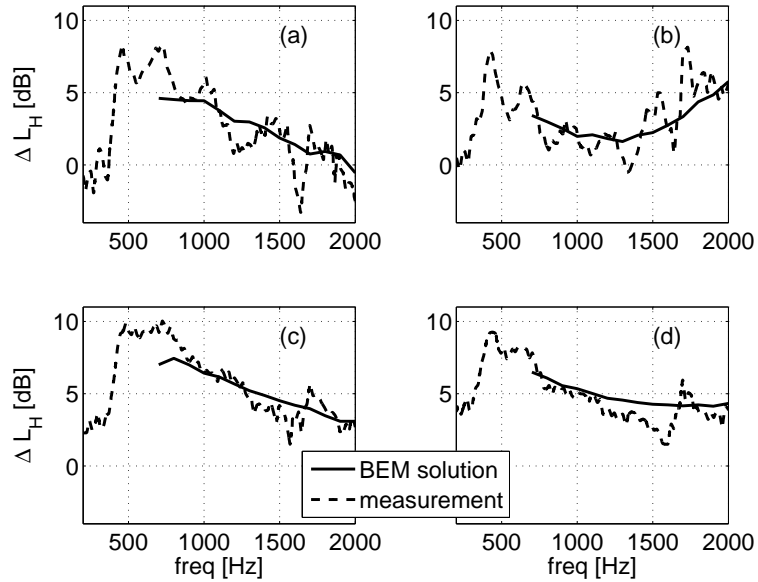


Figure 4.20.: Calculated and measured horn effect of a tyre above an plane of finite impedance. Measurement data from [149, Fig. 4-6, 4-7].

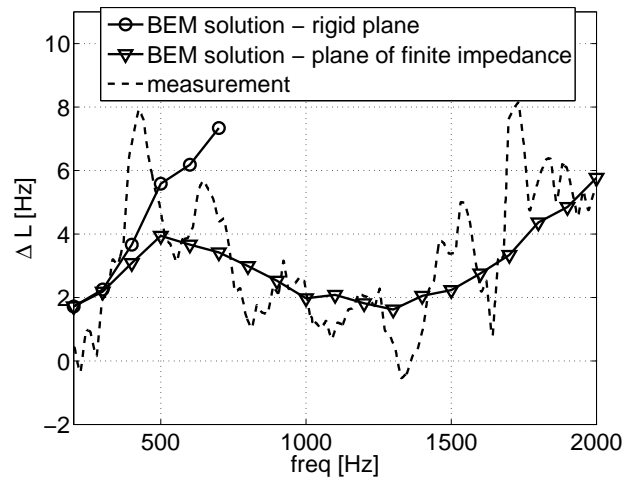


Figure 4.21.: Calculated and measured horn effect of a tyre above an plane of finite impedance [Setup b, see Tab. 4.4]. Measurement data from [149, Fig. 4-6b].

in Fig. 4.21. The measured decrease of ΔL_H towards the lower frequency range can be predicted very well by the BEM simulation. Though the setup of the system matrices \mathbf{H} and \mathbf{G} is more and more expensive towards lower frequencies, the integral term of Eq. (4.26) almost vanishes at low frequencies since the impedance of the mineral wool layer increases and γ decreases, respectively. For $\gamma \rightarrow 0$, the assumption of a rigid plane holds also for the mineral wool layer. In Fig. 4.21 there can be additionally found the frequency response of ΔL_H assuming a rigid impedance plane. As it can be seen, at the lowest frequencies the horn effect amplification level for a rigid plane actually meets that for the plane of finite impedance.

Chapter 5

Conclusions and further work

In this thesis the BEM was applied to combustion noise and to half-space problems. Whereas the half-space BEM project was devoted to the development of a specialised BEM with respect to the particular half-space geometry, the combustion noise project was focussed on the application of a standard BEM to a non-standard sound source.

5.1. Combustion noise

The calculation of the sound radiation of open, turbulent, non-premixed jet flames was based on a hybrid approach, where the BEM was directly coupled to an incompressible LES of the source region. The hybrid approach was applied to two flames, the HD- and the H3-flame. The numerical aspects of the coupling were investigated as well as its general validity. The simulation results were validated by measurements of the radiated sound power of the investigated flames. The thesis leads to the following conclusions:

- Regarding combustion noise, where strong volume sources due to turbulent density fluctuations in the combustion zone govern the sound generation processes, the current incompressible LES approach yields velocity data at a control surface surrounding the source region (Kirchhoff's surface), which are suitable for an acoustic continuation of the source domain simulation by a BEM.

This conclusion can be drawn from the theoretical discussion and it is corroborated by the simulation results. The comparison of simulated and measured sound power of the HD-flame shows a good overall agreement, whereas the

simulated sound power of the H3-flame strongly differs from the measured one. However, a closer look at the sound intensity at several measuring points shows a good agreement of the simulated and measured data for measuring points close to the lateral surface of the Kirchhoff's surface. The high deviations occur at measuring points close to the outflow cap of the Kirchhoff's surface.

- The velocity data at the portion of the Kirchhoff's surface, which intersects with the flow (inflow/outflow boundary), require a special treatment. Due to the adjacent burner, a rigid boundary condition could be prescribed at the inflow cap of the Kirchhoff's surfaces. After this input data correction at the inflow boundary, the outflow boundary became the main error source for the acoustic simulation. On the one hand, the requirement of an homogeneous density and temperature distribution at the Kirchhoff's surface is mostly violated at the outflow closing disk. On the other hand, the velocity distribution at this portion of the enclosing control surface is disturbed by hydrodynamic velocity fluctuations due to convecting vortical structures of the flow, which pass the outflow boundary. In view of the required correction of the velocity data at the outflow boundary, the following conclusion can be drawn from the thesis:
 - o The Principal Component Analysis (PCA) does not provide a proper correction of the velocity data.
 - o A splitting technique, which is based on the Helmholtz theorem for vector fields, is the most promising approach for an appropriate input data correction.
- The accuracy of the hybrid approach is very sensitive to the location of the Kirchhoff's surface. It has to be ensured that the Kirchhoff's surface is located in the homogeneous region around the combustion zone, where density and temperature at the Kirchhoff's surface are equal to those of the ambient medium.
- The data sampling at the Kirchhoff's surface is another critical point of the hybrid approach. The coarsening of the fine LES grid induces a downsampling of the velocity data. Due to this spatial downsampling aliasing effects may occur, which lead to a distinct overestimation of the radiated sound power. Advanced filter techniques have to be applied during the sampling process to avoid an aliasing of the BEM input data.

- The determination of an average sound power spectrum is a time-consuming process, which requires several BEM runs for each frequency step. In the thesis, it could be shown that the use of averaged velocity transfer functions as input data for the BEM is a time-saving alternative provided the Kirchhoff's surface lies in the homogeneous domain and the number of averages is sufficient.
- Regarding the used cylindrical Kirchhoff's surface the CHIEF method is an appropriate regularisation method to remedy the non-uniqueness problem of the BEM for exterior problems. The CHIEF method is computationally efficient, simply to implement and sufficiently guarantees uniqueness of the BEM results over a wide frequency range.

5.2. Half-space BEM

The aim of this work was the development of a specialised BEM formulation for half-spaces, whose boundary planes are characterised by a finite acoustic impedance. Generally, the implementation of an appropriate half-space Green's function into the BEM is the most effective way of taking such an infinite impedance plane into account. Several approximate and exact solutions for the Green's function for the sound radiation above an impedance plane were reviewed and tested for the applicability within a BEM formulation. The results and conclusions can be summarised as follows:

- The exact Green's function in terms of the complex image method is the most appropriate solution for an implementation within the BEM. The behaviour of this Green's function and its derivatives were analysed in detail.
 - Two quadrature techniques have been studied and applied to evaluate the improper integral, which is part of the Green's function. The multi-grid quadrature is characterised by its high stability. It can be applied without any restrictions and yields very reliable results. However, it is a time-consuming quadrature technique. The Gauss-Laguerre quadrature is much faster, but its application is restricted to a rather soft boundary condition at the impedance plane, which is often fulfilled in the higher frequency range considering real grounds, and a sufficient height of the radiating/scattering objects above the impedance plane.
- Several academic test cases verified the applicability of the selected Green's function and its correct implementation in the BEM code BEMLAB. The following test cases have been investigated:

- Sound radiation of a pulsating sphere above a perfectly rigid and perfectly soft plane, respectively.
 - Comparison between prescribed and back-calculated impedance of the plane.
 - Sound field in case of perpendicular incidence.
- The comparison with an alternative approach, which was based on the use of a discretised portion of the impedance plane, showed the high quality of the half-space BEM solution.

The alternative half-space calculation was performed by means of the indirect BEM. The infinite impedance plane was represented by a discretised plane model of finite extend. The influence of the size and the discretisation level of the plane model on the accuracy of the sound field solution was investigated. Neither a large plane model (edge length about 14λ) nor a very fine discretisation (size of the elements about $1/14\lambda$) yielded a satisfactory simulation of the sound field above the plane. In the area directly above the plane, the simulation error ranged between 5% and 25%. The simulated sound field outside the finite plane model was completely erroneous. The simulation error of the developed half-space BEM, on the contrary, was about 2.5% over a wide spatial range. The simulation error increased only at observation points, which were very far away from the sound source (distance more than 200λ).

- The horn effect of the tyre–road interface was chosen as benchmark problem for the developed half-space BEM. The complex horn geometry required an advanced numerical treatment, which was successfully implemented in the BEMLAB code. The simulated horn effect over an impedance plane was compared with measurement data. The high agreement of the simulated and measured effect in case of a rigid plane as well as in case of a mineral wool layer validates the half-space BEM approach.

5.3. Future work

Both BEM projects concentrated on the development and application of the BEM in acoustics. On the one hand, the BEM served as a far field method in a hybrid approach for the determination of the radiated sound power of open flames. On the other hand, a specialised half-space BEM was developed to account for the presence of an infinite impedance plane in the acoustic domain. The results of

the thesis are encouraging and can serve as starting points for further research work in these directions.

Combustion noise The computationally efficient coupling of an incompressible LES and a BEM yielded promising results. Certainly, further improvements of the hybrid approach are required in order to allow an exact prediction of the sound emission from combustion processes.

- An accurate input data correction at the outflow boundary of the Kirchhoff's surface around the flame remain as a main task for a further application of hybrid approaches. The development of the outlined splitting technique, which is based on the Helmholtz theorem and utilises the option of the Dual Reciprocity Boundary Element Method (DRBEM) to account for inhomogeneities in a control volume by converting the volume integral into a boundary integral, is a very worthwhile future task.
- The coarsening of the fine mesh, which is used by methods of Computational Fluid Dynamics (CFD), such as incompressible or compressible LES, implicates a downsampling of the original CFD data. The strong influence of the downsampling on the sound field solution was studied in the thesis, but a satisfying remedy for the occurring aliasing effect could not be provided. There is a strong need in advanced filtering techniques to avoid aliasing effects due to the spatial downsampling.
- The development of a full three zonal approach, which combines a CFD method for the solution of the incompressible or compressible Navier-Stokes equations in the source domain (Direct Numerical Simulation (DNS), LES *et al.*) with a CAA method for a inhomogeneous propagation zone (Linearised Euler Equations (LEE), Acoustic Perturbation Equation (APE) *et al.*) and the BEM as far field method, would be an interesting issue. Certainly, a three zonal approach requires the detailed study of the two coupling steps. A three zonal approach may be appropriate to calculate the noise emission from swirl flames, where stronger hydrodynamic disturbances at the lateral surfaces of the Kirchhoff's surface can be expected.
- A coupling of the BEM to a compressible LES of the HD- and the H3-flame could not be performed in the combustion noise project, because a compressible LES of open, non-premixed jet flames was not available during the project period. However, there is not much difference expected between the coupling

of the BEM to a compressible LES and the coupling to the presented incompressible LES regarding the investigated flames. The incompressible LES is able to describe the velocity field of non-zero divergence due to volume sources in the combustion zone, which are the main sound sources. But a comparison of the presented results with those, obtained by a coupling to a compressible LES could additionally corroborate the comparatively inexpensive coupling to an incompressible LES. The outflow boundary problem as well as the down-sampling problem remain the major research issues, since they also arise in conjunction with a compressible LES.

Half-space BEM The aim of the half-space BEM project to develop a universal BEM formulation for half-spaces with arbitrary boundary condition at the boundary plane could be achieved. But the evaluation of the matrix coefficients represents the bottleneck of the current half-space approach. The half-space BEM could be further enhanced by

- An improved or alternative quadrature technique for the evaluation of the improper integral in the used Green's function.
- A detailed investigation of Thomasson's solution and Y. L. Li's solution for the sound radiation above an impedance planes. These solutions may allow a faster evaluation of the matrix coefficients for a given geometry and boundary condition of the impedance plane.
- The combination of the current half-space BEM with Fast Multipole Methods and a reformulation in terms of the indirect BEM approach.

Bibliography

- [1] Virtual.Lab. <http://www.lmsintl.com/simulation/virtuallab/>.
- [2] Vnoise. <http://www.sts-soft.com/VNoise.aspx>.
- [3] FastBEM Acoustics. <http://www.fastbem.com/index.html>.
- [4] R. D. Ciskowski and C. A. Brebbia, editors. *Boundary Element Method in Acoustics*. Computational Mechanics Publications / Elsevier Applied Science, Southampton, 1991.
- [5] J. O. Watson. Boundary elements from 1960 to the present day. *Electron. J. Bound. Elem.*, 1(1):34–46, 2003.
- [6] A. Ali and C. Rajakumar. *The Boundary Element Method: Applications in Sound and Vibration*. A. A. Balkema Publ., Lisse, 2004.
- [7] BENET bibliography. <http://www.olemiss.edu/sciencenet/benet/>.
- [8] I. Fredholm. Sur une classe d'équations fonctionnelles. *Acta Mathematica*, 27(1):365–390, 1903.
- [9] M. A. Jawson. Integral equation methods in potential theory: I. *Proc. Roy. Soc. Lond. (A)*, 275(1360):23–32, 1963.
- [10] G. T. Symm. Integral equation methods in potential theory: II. *Proc. Roy. Soc. Lond. (A)*, 275(1360):33–46, 1963.
- [11] M. B. Friedman and R. P. Shaw. Diffraction of a plane shock wave by an arbitrary rigid obstacle. *J. Appl. Mech.*, 29:40–46, 1962.
- [12] R. P. Banaugh and W. Goldsmith. Diffraction of steady acoustic waves by surface of arbitrary shape. *J. Acoust. Soc. Am.*, 35(10):1590–1601, 1963.
- [13] G. Chertock. Sound radiation from vibrating surfaces. *J. Acoust. Soc. Am.*, 36(7):1305–1313, 1964.
- [14] L. G. Copley. Integral equation method for radiation from vibrating bodies. *J. Acoust. Soc. Am.*, 41(4):807–816, 1967.
- [15] H. A. Schenck. Improved integral formulation for acoustic radiation problems. *J. Acoust. Soc. Am.*, 44(1):41–58, 1968.

- [16] A. J. Burton and G. F. Miller. The application of integral equation methods to the numerical solution of some exterior boundary problems. *Proc. Roy. Soc. Lond. (A)*, 323(1553):201–220, 1971.
- [17] R. E. Kleinman and G. F. Roach. Boundary integral equations for the three-dimensional Helmholtz equation. *SIAM Review*, 16(2):214–236, 1974.
- [18] W. L. Meyer, W. A. Bell, B. T. Zinn, and M. P. Stallybrass. Boundary integral solutions of three dimensional acoustic radiation problems. *J. Sound Vibr.*, 59(2): 245 – 262, 1978.
- [19] A. F. Seybert, B. Soenarko, F. J. Rizzo, and D. J. Shippy. Application of the BIE method to sound radiation problems using an isoparametric element. *J. Vibr., Acous., Stress, and Reliab. in Design, Trans. ASME*, 106:414–420, 1984.
- [20] A. F. Seybert, B. Soenarko, F. J. Rizzo, and D. J. Shippy. An advanced computational method for radiation and scattering of acoustic waves in three dimensions. *J. Acoust. Soc. Am.*, 77(2):362–368, 1985.
- [21] S. Amini and D. T. Wilton. An investigation of boundary element methods for the exterior acoustic problem. *Comput. Meth. Appl. Mech. Eng.*, 54(1):49–65, 1986.
- [22] A. F. Seybert and T. K. Rengarajan. The use of CHIEF to obtain unique solutions for acoustic radiation using boundary integral equations. *J. Acoust. Soc. Am.*, 81 (5):1299–1306, 1987.
- [23] C. A. Brebbia, editor. *Recent advances in boundary element methods*. Pentech Press, London, 1978.
- [24] T. W. Wu, editor. *Boundary Element Acoustics: Fundamentals and Computer Codes*. WIT Press, Southampton, Boston, 2000.
- [25] O. von Estorff, editor. *Boundary Element Acoustics: Advances & Applications*. WIT Press, Southampton, Boston, 2000.
- [26] S. Marburg and B. Nolte, editors. *Computational Acoustics of Noise Propagation in Fluids - Finite and Boundary Elements Methods*. Springer, Berlin, 2008.
- [27] N. A. Gumerov and R. Duraiswami. *Fast multipole methods for the Helmholtz equation in three dimensions*. Elsevier Series in Electromagnetism. Elsevier, Amsterdam, London, 2004.
- [28] B. Nolte, I. Schäfer, J. Ehrlich, M. Ochmann, R. Burgschweiger, and S. Marburg. Numerical methods for wave scattering phenomena by means of different boundary integral formulations. *J. Comput. Acoust.*, 15(4):495–529, 2007.
- [29] R. Courant and D. Hilbert. *Methoden der mathematischen Physik*. Springer, Berlin, 4th edition, 1993.
- [30] A. Sommerfeld. Die Greensche Funktion der Schwingungsgleichung. *Jhrber. Deutsch. Math.-Verein.*, 21:309–353, 1912.
- [31] A. Kneschke. *Differentialgleichungen und Randwertprobleme*, volume II, Par-

- tielle Differentialgleichungen. B. G. Teubner Verlagsgesellschaft, Leipzig, Germany, 2nd edition, 1961.
- [32] M. Abramowitz and I. A. Stegun, editors. *Handbook of mathematical functions*. Dover Publications, Inc., New York, 1972.
- [33] A. Tadeu and J. António. Use of constant, linear and quadratic boundary elements in 3D wave diffraction analysis. *Eng. Anal. Bound. Elem.*, 24(2):131–144, 2000.
- [34] S. Marburg and S. Schneider. Influence of element types on numeric error for acoustic boundary elements. *J. Comput. Acoust.*, 11(3):363–386, 2003.
- [35] Future noise policy - European Commission Green Paper, COM(96) 540, 1996.
- [36] U. Kuckartz, H. Grunenberg, A. Rheingans-Heintze, and S. Rädiker. *Umweltbewusstsein in Deutschland—Ergebnisse einer repräsentativen Bevölkerungsumfrage*. Bundesministerium für Umwelt, Naturschutz und Reaktorsicherheit (BMU), Berlin, 2000–2006. <http://www.umweltbewusstsein.de/>.
- [37] C. Wippermann, M. Calmbach, and S. Kleinhüchelkotten. *Umweltbewusstsein in Deutschland—Ergebnisse einer repräsentativen Bevölkerungsumfrage*. Bundesministerium für Umwelt, Naturschutz und Reaktorsicherheit (BMU), Berlin, 2008. <http://www.umweltbundesamt.de/umweltbewusstsein/umweltbewusstsein.htm>.
- [38] CALM II network. Research for a quieter Europe in 2020. <http://www.calm-network.com>, Sep. 2007.
- [39] T. T. Wolde. EU noise policy and related research needs. *Acta Acustica united with Acustica*, 89(5):735–742, 2003.
- [40] A. H. Lefebvre. *Gas Turbine Combustion*. Taylor & Francis, Philadelphia, Pa., 2nd edition, 1999.
- [41] C.-C. Hantschk and E. Schorer. Vorhersage der Schallemissionen industrieller Fackelsystem. In Deutsche Gesellschaft für Akustik, editor, *Fortschritte der Akustik - DAGA '2005*, pages 517–518, München, Germany, 2005. ISBN 3-9808659-0-8.
- [42] J. R. Stone, E. A. Krejsa, and B. J. Clark. Progress in core/combustion noise prediction. In *43rd AIAA Aerospace Sciences Meeting and Exhibit*, Reno, Nevada, USA, 2005.
- [43] S. Candel, D. Durox, S. Ducruix, A. L. Birbaud, N. Noiray, and T. Schuller. Flame dynamics and combustion noise: progress and challenges. *Int. J. Aeroacoust.*, 8(1-2):1–56, 2009.
- [44] A. Schwarz and J. Janicka, editors. *Combustion Noise*. Springer, Berlin, 2009.
- [45] T. P. Bui, W. Schröder, and M. Meinke. Acoustic perturbation equations for reacting flows to compute combustion noise. *Int. J. Aeroacoust.*, 6(4):335–355, 2007.
- [46] F. Flemming, A. Sadiki, and J. Janicka. Investigation of combustion noise using a

- LES/CAA hybrid approach. *Proc. Combust. Inst.*, 31:3189–3196, 2007.
- [47] J. Warnatz, U. Maas, and R. W. Dibble. *Combustion*. Springer, Berlin, 6th edition, 2006.
- [48] A. M. Kempf. *Large Eddy Simulation of Non-premixed Flames*. PhD thesis, Institute for Energy and Powerplant Technology, TU Darmstadt, Germany, 2003.
- [49] M. M. Tacke. *Zur Stabilität angehobener turbulenter Diffusionsflammen*. PhD thesis, Institute for Energy and Powerplant Technology, TU Darmstadt, Germany, 1998.
- [50] H. Forkel. *Über die Grobstruktursimulation turbulenter Wasserstoff-Diffusionsflammen*. PhD thesis, Institute for Energy and Powerplant Technology, TU Darmstadt, Germany, 1999.
- [51] H. Forkel and J. Janicka. Large-eddy simulation of a turbulent hydrogen diffusion flame. *Flow, Turbulence and Combustion*, 65(2):163–175, 2001.
- [52] F. Flemming. *On the Simulation of Noise Emissions by Turbulent Non-Premixed Flames*. PhD thesis, Institute for Energy and Powerplant Technology, TU Darmstadt, Germany, 2007.
- [53] International workshop on measurement and computation of turbulent non-premixed flames. <http://public.ca.sandia.gov/TNF/abstract.html>.
- [54] T. Hüttl, C. Wagner, and J. Delfs, editors. *LES for Acoustics*, Göttingen, Germany, 7.-8. October 2002.
- [55] A. S. Lyrintzis. Surface integral methods in computational aeroacoustics - from the (CFD) near-field to the (acoustic) far field. *Int. J. Aeroacoust.*, 2(2):95–128, 2003.
- [56] S. A. Klein and J. B. W. Kok. Sound generation by turbulent non-premixed flames. *Comb. Sci. Tech.*, 149(1-6):267–295, 1999.
- [57] S. A. Klein. *On the acoustics of turbulent non-premixed flames*. PhD thesis, University of Twente, Netherlands, 2000.
- [58] T. P. Bui, W. Schröder, and M. Meinke. Numerical analysis of the acoustic field of reacting flows via acoustic perturbation equations. *Comput. Fluid.*, 37(9):1157–1169, 2008.
- [59] F. Zhang, P. Habisreuther, M. Hettel, and H. Bockhorn. Numerical investigations of the noise sources generated in a swirl stabilized flame. *Acta Acustica united with Acustica*, 95(3):418–427, 2009.
- [60] E. Manoha, G. Elias, B. Troff, and P. Sagaut. Towards the use of boundary element method in computational aeroacoustics. In *5th AIAA/CEAS Aeroacoustics Conference*, Bellevue, WA, USA, 1999.
- [61] L. Morino, M. Gennaretti, U. Iemma, and F. Salvatore. Aerodynamics and aeroacoustics of wings and rotors via BEM - unsteady, transonic, and viscous effects. *Comput. Mech.*, 21(4/5):265–275, 1998.

- [62] C. Montavon, I. Jones, D. Szepessy, R. Henriksson, Z. el Hachemi, S. Dequand, M. Piccirillo, M. Tournour, and F. Tremblay. Noise propagation from a cylinder in a cross flow: comparison of SPL from measurements and from a CAA method based on a generalised acoustic analogy. In *IMA Conference on Computational Aeroacoustics*, University of Greenwich - Maritime Greenwich Campus, 2002.
- [63] C. Polacsek and S. Burguburu. CFD-BEM coupling for computing noise radiated from engine inlets. In *Proc. Computational Aeroacoustics - Euromech 449*, Chamonix, France, 2003.
- [64] P. Költzsch. Flow acoustics. In F. P. Mechel, editor, *Formulas of Acoustics*, chapter N, pages 846–929. Springer, Berlin, 2002.
- [65] C. Richter and F. Thiele. Zonal approaches for the simulation of indirect combustion noise. In *Proc. International Congress on Acoustics - ICA*, Madrid, Spain, 2007.
- [66] L. S. G. Kovásznyai. Turbulence in supersonic flow. *J. Aeronautic. Sci.*, 20(10): 219–237, 1953.
- [67] B.-T. Chu and L. S. G. Kovásznyai. Non-linear interactions in a viscous heat-conducting compressible gas. *J. Fluid Mech.*, 3(5):494–514, 1958.
- [68] C. Bogey and C. Bailly. Three-dimensional non-reflective boundary conditions for acoustic simulations: far field formulation and validation test cases. *Acta Acustica united with Acustica*, 88(4):463–471, 2002.
- [69] J. H. Ferziger and M. Perić. *Computational methods for fluid dynamics*. Springer, Berlin, 3rd rev. edition, 2002.
- [70] G. K. Batchelor. *An introduction to fluid dynamics*. Cambridge Univ. Pr., London, 1974.
- [71] F. Fahy. *Sound intensity*. E & FN Spon, London, 2nd edition, 1995.
- [72] W. C. Strahle. On combustion generated noise. *J. Fluid Mech.*, 49(2):399–414, 1971.
- [73] W. C. Strahle. Some results in combustion generated noise. *J. Sound Vibr.*, 23(1):113–125, 1972.
- [74] W. C. Strahle. Combustion noise. *Progr. Energ. Combust. Sci.*, 4(3):157–176, 1978.
- [75] D. G. Crighton, A. P. Dowling, J. E. Ffowcs-Williams, M. Heckl, and F. G. Leppington. *Modern Methods in Analytical Acoustics*. Springer, London, 1992.
- [76] S. Gade. *Sound Intensity, Part I. Theory*. Number 3 in Technical review. Brüel & Kjær, Nærum, Denmark, 1982.
- [77] G. A. Korn and T. M. Korn. *Mathematical handbook for scientists and engineers*. Dover Publ., Inc., Mineola, New York, 2000.

- [78] H.-O. Georgii. *Stochastics: Introduction to Probability and Statistics*. de Gruyter, Berlin, 2008.
- [79] A. V. Oppenheim, R. W. Schaffer, and J. R. Buck. *Zeitdiskrete Signalverarbeitung*. Pearson Studium, München, 2004.
- [80] T. Ph. Bui, M. Ihme, M. Meinke, W. Schröder, and H. Pitsch. Numerical applicability of different sound source formulations to compute combustion noise using acoustic perturbation equations for reacting flows. In *14th AIAA/CEAS Aeroacoustics Conference (29th AIAA Aeroacoustics Conference)*, Vancouver, British Columbia Canada, 2008. AIAA 2008-2948.
- [81] K. Pearson. On lines and planes of closest fit to systems of points in space. *Phil. Mag.*, 2(6):112–117, 1901.
- [82] R. A. Johnson and D. W. Wichern. *Applied multivariate statistical analysis*. Prentice-Hall series in statistics. Prentice-Hall, Englewood Cliffs, NJ, 2nd edition, 1988.
- [83] H. Wu, M. Siegel, and P. Khosla. Vehicle sound signature recognition by frequency vector principal component analysis. *Trans. Instrum. Meas.*, 48(5):1005–1009, 1999.
- [84] C. C. Tan, N. F. Thornhill, and R. M. Belchamber. Principal component analysis of spectra with application to acoustic emissions from mechanical equipment. *Trans. Inst. Meas. Contr.*, 24(4):333–353, 2002.
- [85] D. J. Kistler and F. L. Wightman. A model of head-related transfer functions based on principal components analysis and minimum-phase reconstruction. *J. Acoust. Soc. Am.*, 91(3):1637–1647, 1992.
- [86] R. H. Cabell and C. R. Fuller. A principal component algorithm for feedforward active noise and vibration control. *J. Sound Vibr.*, 227(1):159–181, 1999.
- [87] P. Belanger, A. Berry, Y. Pasco, O. Robin, Y. St-Amant, and S. Rajan. Multi-harmonic active structural acoustic control of a helicopter main transmission noise using the principal component analysis. *Appl. Acoust.*, 70(1):153–164, 2009.
- [88] J. Shlens. *A Tutorial on Principal Component Analysis*, 2005. <http://www.sn1.salk.edu/~shlens/pub/notes/pca.pdf>.
- [89] K. V. Mardia, J. T. Kent, and J. M. Bibby. *Multivariate Analysis*. Academic Press, London, 1979.
- [90] C. M. Stein. Multivariate analysis I. Technical Report 42, Dept. Statistics Stanford Univ., 1969.
- [91] V. A. Marčenko and L. A. Pastur. Distribution of eigenvalues for some sets of random matrices. *Math. USSR – Sbornik*, 1(4):457–483, 1967.
- [92] I. M. Johnstone. On the distribution of the largest eigenvalue in principal components. *Ann. Stat.*, 29(2):295–327, 2001.

- [93] V. R. Katta, L. P. Goss, and W. M. Roquemore. Simulation of vortical structures in a jet diffusion flame. *Int. J. Numer. Meth. Heat Fluid Flow*, 4(5):413–424, 1994.
- [94] J. B. Freund, S. K. Lele, and P. Moin. Calculation of the radiated sound field using an open Kirchhoff surface. *AIAA J.*, 34(5):909–916, 1996.
- [95] N. Andersson, L.-E. Eriksson, and L. Davidson. Investigation of an isothermal Mach 0.75 jet and its radiated sound using large-eddy simulation and Kirchhoff surface integration. *Int. J. Heat Fluid Flow*, 26(3):393–410, 2005.
- [96] M. L. Shur, P. R. Spalart, and M. K. Strelets. Noise prediction for increasingly complex jets. part I: Methods and tests. *Int. J. Aeroacoust.*, 4(4-5):213–246, 2005.
- [97] N. C. Ovenden and S. W. Rienstra. Mode-matching strategies in slowly varying engine ducts. *AIAA J.*, 42(9):1832–1840, 2004.
- [98] G. Vilenski. Mode matching in engine ducts with vortical flows. In *Collection of Technical Papers - 12th AIAA/CEAS Aeroacoustics Conference*, volume 4, pages 2325–2335, 2006.
- [99] W. De Roeck, M. Baelmans, and W. Desmet. Aerodynamic/acoustic splitting technique for computational aeroacoustics applications at low mach numbers. *AIAA J.*, 46(2):463–475, 2008.
- [100] R. Piscoya and M. Ochmann. Separation of acoustic and hydrodynamic components of the velocity for a CFD-BEM hybrid approach. In *Proc. Int. Conf. on Acoustics (NAG/DAGA 2009)*, Rotterdam, Netherlands, 2009.
- [101] A. Sommerfeld. *Mechanik der deformierbaren Medien*. Vorlesungen über theoretische Physik. Harri Deutsch, Thun-Frankfurt/Main, 6th edition, 1978.
- [102] H. Herwig. *Strömungsmechanik A-Z*. Vieweg, Wiesbaden, 2004.
- [103] L. C. Wrobel. *Application in Thermo-Fluids and Acoustics*, volume 1 of *The Boundary Element Method*. John Wiley & Sons, 2002.
- [104] R. Piscoya, H. Brick, and M. Ochmann. Determination of the far field sound radiation from flames using the dual reciprocity boundary element method. *Acta Acustica united with Acustica*, 95(3):448–460, 2009.
- [105] S. Amini and P. J. Harris. A comparison between various boundary integral forms of the exterior acoustic problem. *Comput. Meth. Appl. Mech. Eng.*, 84(1):59–75, 1990.
- [106] W. Benthien and A. Schenck. Nonexistence and nonuniqueness problems associated with integral equation methods in acoustics. *Comput. Struct.*, 65(3):295–305, 1997.
- [107] S. Marburg and T. W. Wu. Treating the phenomena of irregular frequencies. In S. Marburg and B. Nolte, editors, *Computational Acoustics of Noise Propagation in Fluids. Finite and Boundary Element Methods*, chapter 15, pages 411–434. Springer, Berlin, 2008.

- [108] G. H. Koopmann and H. Benner. Method for computing the sound power of machines based on the Helmholtz integral. *J. Acoust. Soc. Am.*, 71(1):78–89, 1982.
- [109] A. Mohsen and M. Hesham. An efficient method for solving the nonuniqueness problem in acoustic scattering. *Comm. Numer. Meth. Eng.*, 22(11):1067–1076, 2006.
- [110] W. Tobocman. Calculation of acoustic wave scattering by means of the Helmholtz integral equation. I. *J. Acoust. Soc. Am.*, 76(2):599–607, 1984.
- [111] M. Ochmann and A. V. Osetrov. Construction of analytical solutions for the error estimation of acoustical boundary element solvers. In *Proc. of the Forum Acusticum*, pages 1000–1004, Sevilla, 2002.
- [112] L. Cremer and M. Hubert. *Vorlesungen über Technische Akustik*. Springer, Berlin, 3rd edition, 1985.
- [113] A. F. Seybert and B. Soenarko. Radiation and scattering of acoustic waves from bodies of arbitrary shape in a three-dimensional half space. *J. Vibr., Acous., Stress, and Reliab. in Design, Trans. ASME*, 110(1):112–117, 1988.
- [114] M. Heckl and H. A. Müller, editors. *Taschenbuch der Technischen Akustik*. Springer, Berlin, 1995.
- [115] F. P. Mechel. *Schallabsorber*, volume 1. Springer, Berlin, 1989.
- [116] A. Sommerfeld. Über die Ausbreitung der Wellen in der drahtlosen Telegraphie. *Ann. Phys.*, 28:665–736, 1909.
- [117] A. Sommerfeld. Über die Ausbreitung der Wellen in der drahtlosen Telegraphie. *Ann. Phys.*, 81:1135–1153, 1926.
- [118] M. Ochmann. The complex equivalent source method for sound propagation over an impedance plane. *J. Acoust. Soc. Am.*, 116(6):3304–3311, 2004.
- [119] I. Rudnick. The propagation of an acoustic wave along a boundary. *J. Acoust. Soc. Am.*, 19(2):348–356, 1947.
- [120] R. B. Lawhead and I. Rudnick. Acoustic wave propagation along a constant normal impedance boundary. *J. Acoust. Soc. Am.*, 23(5):546–549, 1951.
- [121] D. Habault and P. J. T. Filippi. Ground effect analysis: Surface wave and layer potential representations. *J. Sound Vib.*, 79(4):529–550, 1981.
- [122] M. A. Nobile and S. I. Hayek. Acoustic propagation over an impedance plane. *J. Acoust. Soc. Am.*, 78(4):1325–1336, 1985.
- [123] L. M. Brekhovskikh. *Waves in layered media*. Academic Press, New York, London, 1960.
- [124] H. Weyl. Ausbreitung elektromagnetischer Wellen über einem ebenen Leiter. *Ann. Phys.*, 60:481–500, 1919.
- [125] U. Ingard. On the reflection of a spherical sound wave from an infinite plane.

- J. Acoust. Soc. Am.*, 23(3):329–335, 1951.
- [126] A. R. Wenzel. Propagation of waves along an impedance boundary. *J. Acoust. Soc. Am.*, 55(5):956–963, 1974.
- [127] C. F. Chien and W. W. Soroka. Sound propagation along an impedance plane. *J. Sound Vib.*, 43(1):9–20, 1975.
- [128] C. F. Chien and W. W. Soroka. A note on the calculation of sound propagation along an impedance surface. *J. Sound Vib.*, 69(2):340–343, 1980.
- [129] S-I. Thomasson. Reflection of waves from a point source by an impedance boundary. *J. Acoust. Soc. Am.*, 59(4):780–785, 1976.
- [130] S-I. Thomasson. Sound propagation above a layer with a large refraction index. *J. Acoust. Soc. Am.*, 61(3):659–674, 1961.
- [131] S-I. Thomasson. Asymptotic solution for sound propagation above an impedance boundary. *Acustica*, 45(2):122–125, 1980.
- [132] K. Attenborough, S. I. Hayek, and J. M. Lawther. Propagation of sound above a porous half-space. *J. Acoust. Soc. Am.*, 68(5):1493–1501, 1980.
- [133] T. Kawai, T. Hidaka, and T. Nakajima. Sound propagation above an impedance boundary. *J. Sound Vib.*, 83(1):125–138, 1982.
- [134] P. J. T. Filippi. Extended source radiation and Laplace type integral representation: Application to wave propagation above and within layered media. *J. Sound Vib.*, 91(1):65–84, 1983.
- [135] P. J. T. Filippi, D. Habault, J.-P. Lefebvre, and A. Bergassoli. *Acoustics: Basic physics, theory and methods*. Academic Press, London, 1999.
- [136] Y. L. Li, M. J. White, and M. H. Hwang. Green’s functions for wave propagation above an impedance ground. *J. Acoust. Soc. Am.*, 96(4):2485–2790, 1994.
- [137] W. L. Li, T. W. Wu, and A. F. Seybert. A half-space boundary element method for acoustic problems with a reflecting plane of arbitrary impedance. *J. Sound Vib.*, 171(2):173–184, 1994.
- [138] G. Taraldsen. The complex image method. *Wave motion*, 43:91–97, 2005.
- [139] M. Ögren and H. Jonasson. Measurement of the acoustic impedance of ground. SP Report 1998:28, SP Swedisch National Testing and Research Institut, 1998.
- [140] R. Blumrich and J. Altmann. Ground impedance measurement over a range of 20 m. *Acta Acustica united with Acustica*, 85(5):691–700, 1999.
- [141] K. Attenborough. Sound propagation close to the ground. *Annu. Rev. Fluid Mech.*, 34:51–82, 2002.
- [142] R. B. Lawhead and I. Rudnick. Measurements on an acoustic wave propagated along a boundary. *J. Acoust. Soc. Am.*, 23(5):541–545, 1951.
- [143] M. E. Delany and E. N. Bazley. Monopole radiation in the presence of an absorbing

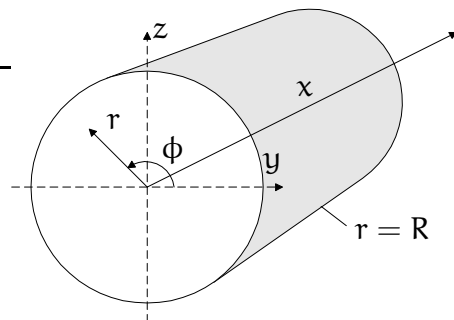
- plane. *J. Sound Vib.*, 13(3):269–279, 1970.
- [144] K. Attenborough, S. Taherzadeh, H. E. Bass, X. Dia, R. Raspet, G. R. Becker, A. Güdesen, A. Chrestman, G. A. Daigle, A. L'Espérance, Y. Gabillet, K. E. Gilbert, Y. L. Li, M. J. White, P. Naz, J. M. Noble, and H. A. J. M. van Hoof. Benchmark cases for sound propagation models. *J. Acoust. Soc. Am.*, 97(1):173–191, 1995.
- [145] V. I. Krylov. *Approximate Calculation of Integrals*. The Macmillan Company, New York, 1962.
- [146] P. Rabinowitz and G. Weiss. Tables of abscissas and weights for numerical evaluation of integrals of the form $\int_0^\infty e^{-x}x^\alpha f(x)dx$. *Math. Tables Aids Comput.*, 13(68):285–293, 1959.
- [147] W. Kropp, F.-X. Bécot, and S. Barrelet. On the sound radiation from tyres. *Acta Acustica united with Acustica*, 86(5):769–779, 2000.
- [148] R. A. G. Graf, C.-Y. Kuo, A. P. Dowling, and W. R. Graham. On the Horn Effect of a Tyre/Road Interface, Part I: Experiment and Computation. *J. Sound Vib.*, 256(3):417–431, 2002.
- [149] F.-X. Bécot. *Tyre noise over impedance surfaces- Efficient application of the Equivalent Sources Method*. PhD thesis, Chalmers University of Technology, Gothenburg, Sweden & Insa – Scientific and Technical University, Lyon, France, 2003.
- [150] V. Cutanda Henríquez, P. M. Juhl, and F. Jacobsen. On the modeling of narrow gaps using the standard boundary element method. *J. Acoust. Soc. Am.*, 109(4):1296–1303, 2001.
- [151] V. Cutanda Henríquez and P. M. Juhl. Acoustic boundary element formulation with treatment of nearly singular integrands by element subdivision. In *19th International Congress on Acoustics - ICA 2007*, Madrid, Spain, 2007.
- [152] M. E. Delany and E. N. Bazley. Acoustic properties of fibrous absorbent materials. *Appl. Acoust.*, 3(2):105–116, 1970.
- [153] M. J. Crocker. *Handbook of Acoustics*. John Wiley & Sons, 1998.
- [154] I. S. Gradshteyn and I. M. Ryzhik. *Table of Integrals, Series, and Products*. Academic Press, Burlington, Mass.; Oxford, 9th edition, 2007.
- [155] T. S. Shao, T. C. Chena, and R. M. Frank. Tables of zeros and gaussian weights of certain associated laguerre polynomials and the related generalized hermite polynomials. *Math. Comput.*, 18(85):598–616, 1964.
- [156] Numerical integration: Abscissas and weights of Gauss-Laguerre integration. http://www.efunda.com/math/num_integration/findgausslaguerre.cfm.

Appendix A

Interior sound field of a cylinder

In the following the acoustic modes of the interior domain of cylinders are analysed analytically. Cylinders are used as Kirchhoff's surfaces in Chapter 3. The knowledge about the mode shapes is important for a correct positioning of the CHIEF points. The CHIEF points are additional collocation points, which are used to remedy the non-uniqueness of the BEM for an exterior problem at the eigenfrequencies of the associated interior problem, see Section 3.4. The CHIEF points only work properly if they are not located at the nodal lines of the interior modes. The boundary condition at the surface of the cylinders is $p = 0$ at S . The

Figure A.1.: Geometry of a cylinder.



sound field inside the cylinder can be described by the ansatz

$$p(r, \phi, x, t) = R(r) \Phi(\phi) X(x) T(t), \quad (\text{A.1})$$

with

$$R(r) = A J_m(k_r r) + B N_m(k_r r), \quad (\text{A.2})$$

$$\Phi(\phi) = \Phi_0 e^{jm\phi}, \quad (\text{A.3})$$

$$X(x) = C \sin(k_x z) + D \cos(k_x z), \quad (\text{A.4})$$

$$T(t) = T_0 e^{j\omega t}. \quad (\text{A.5})$$

From the wave equation in polar coordinates follows

$$-\frac{\omega}{c_0} + k_x^2 + k_r^2 = 0, \quad (\text{A.6})$$

$$k_x^2 = k_0^2 - k_r^2.$$

k_r and k_x can be determined by inserting the boundary conditions

$$p(r = R) = 0, \quad p(x = 0) = 0 \quad \text{and} \quad p(x = L) = 0$$

into Eqs. (A.1) – (A.5):

$$p(r = R) = 0 \quad \Rightarrow \quad J_m(k_r R) = 0, \quad (\text{A.7})$$

$$p(x = 0) = 0 \quad \Rightarrow \quad D = 0, \quad (\text{A.8})$$

$$p(x = L) = 0 \quad \Rightarrow \quad k_x L = n\pi \quad \Rightarrow \quad k_x = n\pi/L, \quad (\text{A.9})$$

where L denotes the length of the cylinder. Since the Neumann function has a singularity at $r = 0$, it has to be eliminated from the solution, i.e. $B = 0$. The wave numbers in radial direction k_r^{mi} are given by the i -th zeros of the m -th Bessel function $J_m(x_{mi}) = 0$,

$$k_r^{mi} = \frac{x_{mi}}{R}. \quad (\text{A.10})$$

The first zeros of the Bessel function of order $0 \leq m \leq 3$ are listed in Tab. A.1. The resulting pressure distributions along the cross section of the cylinders for the first modes are shown in Fig. 3.28 at Page 54. The nodal lines of the radial sound field can be clearly recognized.

The wave number in x -direction can be obtained from

$$k_x^{mi} = \sqrt{k_0^2 - (k_r^{mi})^2} = \sqrt{k_0^2 - (x_{mi}/R)^2}. \quad (\text{A.11})$$

The wave number k_x^{mi} is only real above the cut-on frequency f_{mi} , i.e. for $k_0^2 > (x_{mi}/R)^2$. That means, the m, i -mode can only propagate above f_{mi} . Table A.2 shows the cut-on frequencies for the tenth cylindrical Kirchhoff's surface of the

m/i	0	1	2	3
0	*	2.404825558	5.520078110	8.653727913
1	-	3.831705970	7.015586670	10.17346814
2	-	5.135622302	8.417244140	11.61984117
3	-	6.380161896	9.761023130	13.01520072

Table A.1.: First zeros x_{mi} of the Bessel function $J_m(x)$.

m/i	0	1	2	3
0	*	1210	2777	4354
1	-	1928	3530	5119
2	-	2584	4235	5846
3	-	3210	4911	6548

Table A.2.: Cut-on frequencies f_{mi} of the tenth cylindrical Kirchhoff's surface of the HD-flame.

HD-flame, which has a radius $R_{10} = 0.1085$ m (see Tab. II in Paper IV). According to Tab. A.2 the occurrence of several eigenfrequencies can be expected in the interesting frequency range up to 4500 Hz. The eigenfrequencies of the finite cylinder are given by

$$\sqrt{k_0^2 - (x_{mi}/R)^2} = n\pi/L. \quad (\text{A.12})$$

The solution of the transcendental equation (A.12) can be found graphically or numerically, as it has been done in Fig. 3.29 at page 57.

Appendix B

Derivation of the sound intensity spectral density

In this section the derivation of the expression for the mean intensity spectral density, Eq. (3.10), is presented. The starting point is Eq. (3.7), which describes the time-averaged intensity of an arbitrary measurement sequence. The functions $\tilde{p}(t)$ and $\tilde{v}_n(t)$ are representable as sums of periodic components and an aperiodic or random component. Generally, the intensity \tilde{I}_n can be expressed as cross-correlation function of $\tilde{p}(t)$ and $\tilde{v}_n(t)$

$$\tilde{I}_n(\tau) = \lim_{T \rightarrow \infty} \frac{1}{T} \int_{-T/2}^{+T/2} \tilde{p}(t + \tau) \tilde{v}_n(t) dt. \quad (\text{B.1})$$

Eq. (3.7) represents $\tilde{I}_n(\tau)$ for $\tau = 0$. The cross-correlation function $\tilde{I}_n(\tau)$ exists, since the time-averages of $|\tilde{p}(t)|^2$ and $|\tilde{v}_n(t)|^2$ exist [77, Ch. 18.10-8],

$$\langle |\tilde{p}(t)|^2 \rangle = \lim_{T \rightarrow \infty} \frac{1}{T} \int_{-T/2}^{T/2} |\tilde{p}(t)|^2 dt < \infty, \quad (\text{B.2})$$

$$\langle |\tilde{v}_n(t)|^2 \rangle = \lim_{T \rightarrow \infty} \frac{1}{T} \int_{-T/2}^{T/2} |\tilde{v}_n(t)|^2 dt < \infty. \quad (\text{B.3})$$

The corresponding cross-spectral density is assigned by the Wiener-Khinchine relations

$$I_n(\omega) = \int_{-\infty}^{\infty} \tilde{I}_n(\tau) e^{-j\omega\tau} d\tau. \quad (\text{B.4})$$

It is defined as

$$I_n(\omega) = \lim_{T \rightarrow \infty} \frac{1}{T} p(\omega) v_n^*(\omega), \quad (\text{B.5})$$

where $p(\omega)$ and $v_n(\omega)$ are the Fourier transforms of the truncated functions $\tilde{p}(t)$ and $\tilde{v}_n(t)$,

$$p(\omega) = \int_{-T/2}^{T/2} \tilde{p}(t) e^{-j\omega t} dt, \quad v_n(\omega) = \int_{-T/2}^{T/2} \tilde{v}_n(t) e^{-j\omega t} dt. \quad (\text{B.6})$$

$p(\omega)$ as well as $\tilde{v}(\omega)$ are two-sided density spectra according to the definitions of the Fourier transform. The intensity cross-spectral density has the dimension $[\text{Wm}^{-2}\text{Hz}^{-1}]$. The expected value of N occurrences of the intensity cross-spectral density $I_n(\omega)$, Eq. (B.5), resulting from N measurement sequences, is

$$\overline{I_n^i(\omega)} = \lim_{N \rightarrow \infty} \frac{1}{N} \sum_{i=1}^N \lim_{T^i \rightarrow \infty} \frac{1}{T^i} p^i(\omega) v_n^{i*}(\omega), \quad (\text{B.7})$$

what was to be demonstrated.

Just to mention, the common formulation [71, 76], [153, Ch. 106]

$$I_n(\omega) = \frac{1}{2} \Re\{p(\omega) v_n^*(\omega)\} \quad (\text{B.8})$$

denotes the one-sided real intensity spectrum with the dimension $[\text{Wm}^{-2}]$. It can be derived from the instantaneous intensity

$$\tilde{I}_n(t) = \tilde{p}(t) \tilde{v}_n(t) \quad (\text{B.9})$$

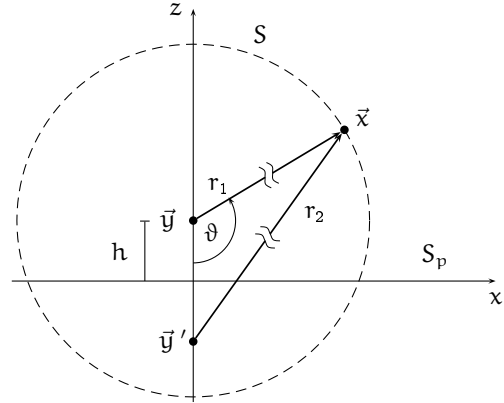
by assuming that both $\tilde{p}(t)$ and $\tilde{v}_n(t)$ are coherent, time-harmonic functions, cf. [71, p. 58].

Appendix C

Monopole source above an infinite plane

In this section an expression for the radiated sound power of a monopole source above a rigid or soft infinite plane is derived. The monopole source is located at \vec{y} , its image source at \vec{y}' . The geometry of this setting is shown in Fig. C.1. The

Figure C.1.: Geometry of a monopole source at \vec{y} above a plane S_p .



total pressure at \vec{x} is given by

$$p(\vec{x}) = A_{\text{src}} \left(\frac{e^{-j k_0 r_1}}{4\pi r_1} + R_p \frac{e^{-j k_0 r_2}}{4\pi r_2} \right), \quad (\text{C.1})$$

see Eqs. (4.8) and (4.9). In the far field, where $r_1, r_2 \rightarrow \infty$ and $h \ll r_1$, the geometrical description can be simplified:

$$r_2^2 = r_1^2 + (2h)^2 - 4r_1 h \cos(\vartheta) = r_1 - 2h \cos(\vartheta) + \mathcal{O}\left(\frac{1}{r_1}\right) \text{ for } r_1 \rightarrow \infty, \quad (\text{C.2})$$

$$\frac{r_2}{r_1} = 1 + \mathcal{O}\left(\frac{1}{r_1}\right) \text{ for } r_1 \rightarrow \infty. \quad (\text{C.3})$$

Using Eqs. (C.2) and (C.3) in Eq. (C.1) yields the approximate far field sound pressure

$$p(\vec{x}) \approx A_{\text{src}} \frac{e^{-j k_0 r_1}}{4\pi r_1} (1 + R_p e^{j k_0 2h \cos(\vartheta)}). \quad (\text{C.4})$$

The radiated sound power is obtained by the integral over the sound intensity along the surface S of a sphere in the far field, which is represented by the dashed line in Fig. C.1.

$$\begin{aligned} P_W &= \frac{1}{2} \int_S p(\vec{x}) v_n(\vec{x})^* dS_x = \frac{1}{2\rho_0 c_0} \int_S |p(\vec{x})|^2 dS_x \\ &= \int_0^{2\pi} \int_0^\pi |p(\vec{x})|^2 r_1^2 \sin(\vartheta) d\vartheta d\varphi \\ &\approx q \int_0^{2\pi} \int_0^\pi |1 + R_p e^{j k_0 2h \cos(\vartheta)}|^2 \sin(\vartheta) d\vartheta d\varphi, \quad (\text{C.5}) \end{aligned}$$

with $q = A_{\text{src}}^2 / (2\rho_0 c_0 (4\pi)^2)$. By means of the substitution $\tau = \cos(\vartheta)$, the integral in Eq. (C.5) can be easily solved and yields

$$P_W \approx 8\pi q + 8\pi q R_p \frac{\sin(k_0 2h)}{k_0 2h}. \quad (\text{C.6})$$

The plane allows the sound radiation only in the upper half-space above the plane and therefore, the actual radiated sound power is approximately the half of that given in Eq. (C.6). So, the relation of the radiated sound power of the monopole source above a rigid plane $P_{W,\text{half}}$ and of the monopole source in the unbounded three-dimensional space $P_{W,\text{free}}$ is given by

$$P_{W,\text{half}} \approx P_{W,\text{free}} \left(1 + R_p \frac{\sin(k_0 2h)}{k_0 2h} \right) \quad (\text{C.7})$$

with $P_{W,\text{free}} = 4\pi q$.

Appendix D

Gauss-Laguerre Quadrature

The Gauss-Laguerre quadrature can be applied to solve integrals of the form $\int_0^\infty x^\alpha e^{-x} f(x) dx$ by the quadrature formula

$$\int_0^\infty x^\alpha e^{-x} f(x) dx = \sum_{k=1}^n w_{nk} f(x_{nk}) + R_n, \quad (\text{D.1})$$

cf. [145, Ch.7.5]. The nodes x_{nk} are the zeros of the Laguerre polynomials $L_n^{(\alpha)}(x)$. R_n denotes the remainder. The Laguerre polynomials are defined as [154, 8.970(1)]

$$L_n^{(\alpha)}(x) = \frac{1}{n!} x^{-\alpha} e^x \frac{d^n}{dx^n} x^{\alpha+n} e^{-x} = \sum_{m=0}^n (-1)^m \binom{n+\alpha}{n-m} \frac{x^m}{m!}. \quad (\text{D.2})$$

They are orthogonal on the half-line $0 \leq x < \infty$ with respect to the weight function $w(x) = x^\alpha e^{-x}$. The corresponding Gaussian weights w_k are determined by [155, (5.12)]

$$w_{nk} = \frac{\Gamma(n+\alpha+1) x_{nk}^\alpha}{[x_{nk}^\alpha L_n^{(\alpha)'}(x_{nk}^\alpha)]^2 n!}, \quad (\text{D.3})$$

with Γ as Gamma function, which obeys $\Gamma(n) = (n-1)!$ for $n \in \mathbb{N}$ [154, 8.339(1)]. All integrands in Eqs. (4.15), (4.24), (4.25) and (4.26) can be transformed into a form $\int_0^\infty e^{-x} f(x) dx$, i.e. $\alpha = 0$ for all integrals, which are examined in this work.

Zeros and weights for the Gauss-Laguerre quadrature for $\alpha = 0$ are given for $n \leq 15$ in [32, Tab. 25.9] and for $n \leq 32$ in [145, App. C] or [146, 156].

But the available numbers were not always sufficient to solve the integrals, see for instance Fig. 4.18 of this thesis or Fig. 17.8 of Paper V. Thus, the calculation of additional zeros and weights became necessary. The calculation procedure

followed the suggestions in [155]. The zeros were found by applying a cubically convergent formulation of Newton's formula

$$x_{i+1} = x_i - \frac{f(x_i)}{f'(x_i)} \left[1 + \frac{1}{2} \left(1 - \frac{1}{x_i} \right) \frac{f(x_i)}{f'(x_i)} \right], \quad (\text{D.4})$$

where the ratio $L_n(x)/L'_n(x)$ was evaluated by a continued fraction

$$\frac{L_n(x)}{L'_n(x)} = \frac{x}{n-2} \frac{n^2}{n-1-x} \frac{(n-1)^2}{2n-3-x} \frac{(n-2)^2}{2n-5-x} \cdots \quad (\text{D.5})$$

The initial guess of the zeros was made by an incremental scanning of the range $0 < x < 400$ with a step size of $\Delta x = 5 \cdot 10^{-4}$ for $x \leq 0.1$ and $\Delta x = 0.1$ for $x > 0.1$. The found zeros were sort into an $n \times 1$ array. The weights were directly obtained by an evaluation of Eq. (D.3). The calculated zeros and weights were checked by the formulas given in [146] and [155]:

$$\sum_{k=1}^n x_{nk} = n^2, \quad (\text{D.6})$$

$$\prod_{k=1}^n x_{nk} = n!, \quad (\text{D.7})$$

$$\sum_{k=1}^n w_{nk} = 1. \quad (\text{D.8})$$

With this procedure, reliable zeros and weights up to $n = 97$ could be found. Fig. D.1 shows exemplarily the checksum for the calculated zeros of the Laguerre polynomials. For $n > 97$ the checksum deviates strongly from the reference value n^2 . The same can be observed regarding the other test functions and the

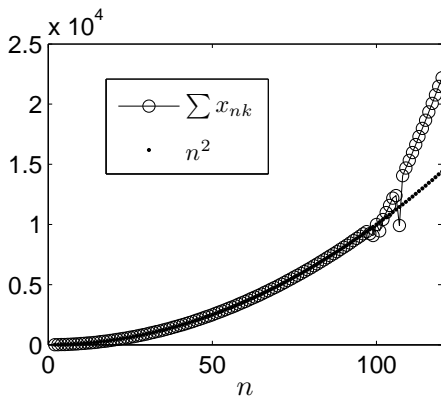


Figure D.1.: Plot of the checksum Eq. (D.6) for the calculated zeros of the Laguerre polynomials.

weights. Therefore, the application of the Gauss-Laguerre quadrature, Eq. (D.1), was limited to $n \leq 97$ throughout this thesis.

In the following the zeros and weights of the Laguerre polynomials for $n = 48, 64, 80$ and 96 are listed as they were used in the thesis.

n	Zeros	Weights
48	2.981123582996229500e-002	7.426200582855775600e-002
	1.571079906178750900e-001	1.522719498092273100e-001
	3.862650375764528100e-001	1.904090882635676400e-001
	7.175746941169671700e-001	1.866330594884085000e-001
	1.151393834026429800e+000	1.534242001357548300e-001
	1.688185823419046800e+000	1.087796928048792400e-001
	2.328527006653214200e+000	6.746073848203983100e-002
	3.073110861652640100e+000	3.688118718307163700e-002
	3.922752413046476600e+000	1.785682407915916900e-002
	4.878393355921337700e+000	7.677610259907287200e-003
	5.941108054624542100e+000	2.935535413274991900e-003
	7.112110535890734800e+000	9.987322141145620200e-004
	8.392762599091222200e+000	3.034636874249801300e-004
	9.784583184687319200e+000	8.389729707559262800e-005
	1.128925916800951900e+001	1.633273200972794800e-005
	1.290865777828552700e+001	2.885386294757852000e-005
	1.464484088320971700e+001	1.004412505133046100e-007
	1.650008142896458500e+001	3.721728298900674500e-010
	1.847688238687410900e+001	4.587510475891300400e-012
	2.057799863402220100e+001	1.957795344242331300e-013
	2.280646229052137400e+001	4.262872326151065800e-015
	2.516561215643910600e+001	4.270162725048975800e-018
	2.765912804448053200e+001	5.667902000572119600e-020
	3.029107100100856400e+001	1.251708991569934400e-021
	3.306593066249874400e+001	1.886001583608776700e-024
	3.598868132747893600e+001	1.611017536859860800e-025
	3.906484876419777000e+001	1.285482681853121700e-027
	4.230059036290309400e+001	2.487933319733643900e-029
	4.570279203851146800e+001	1.856176334946463700e-031
	4.927918638283679100e+001	1.896239876576773700e-032
	5.303849808781666300e+001	8.267290726438679600e-034
	5.699062481480447700e+001	1.974733867810212600e-033
	6.114686478614022700e+001	6.561369823951552800e-038
	6.552020692901861300e+001	1.344764749916119500e-039
	7.012570623611318900e+001	3.787862589385241200e-042
	7.498097751891131700e+001	2.000071166612331600e-044
	8.010685735032439000e+001	4.618749434942286900e-046
	8.552831111603417500e+001	1.617048659018728500e-046
	9.127570799366809200e+001	1.266246223837077200e-049
	9.738666771358153100e+001	7.808128648695307300e-052
	1.039088333571762500e+002	1.137521838806771100e-053
	1.109042208849762800e+002	8.217855213867806800e-047
	1.184564250462836400e+002	2.246627244098326800e-057
	1.266834257688858300e+002	1.181561684165349400e-057
	1.357625895778643000e+002	1.197553650708153700e-061
	1.459864327094634600e+002	5.754029077396281600e-064
	1.579156120229780000e+002	5.684037899736413700e-068
	1.729963281485596800e+002	1.300486556997111600e-074
64	2.241587414670615300e-002	5.625284233930856500e-002
	1.181225120967627900e-001	1.190239873115246400e-001
	2.903657440180280000e-001	1.574964038603987300e-001
	5.392862212279907500e-001	1.675470504213599200e-001
	8.650370046481220500e-001	1.533528558262665100e-001
	1.267814040775239200e+000	1.242210546032455200e-001
	1.747859626059432100e+000	9.034228717470778300e-002
	2.305463739307502400e+000	5.947785163049286400e-002
	2.940965156725252600e+000	3.562760491687755300e-002
	3.654752650207294500e+000	1.947758286830489700e-002
	4.447266343313100600e+000	9.773153684748453800e-003
	5.31899254496390000e+000	4.357282688581676600e-003
	6.270499046923657900e+000	2.347477872688442500e-003
	7.302370002587385200e+000	3.001017122109486300e-004
	8.415275239483021300e+000	6.468194718338064800e-004
	9.609939192796117500e+000	2.727255919042036500e-006
	1.088715038388636800e+001	1.184788931844316000e-009
	1.224776450424431000e+001	4.470506137458739500e-011
	1.369270784554750600e+001	1.469674085931901200e-013
	1.522298111152472600e+001	7.585341674247746200e-015
	1.683966365264876000e+001	6.160506024624121200e-017
	1.854391817085919000e+001	1.225520933066315100e-019

Table D.1.: Zeros and weights of the associated Laguerre polynomials for $n = 48, 64, 80$ and 96 .

n	Zeros	Weights
	2.033699594873024100e+001	3.535637405315600300e-022
	2.222024266595088800e+001	1.769333098317601600e-024
	2.419510487593325700e+001	2.781030285667655100e-026
	2.626313722711848400e+001	3.402773846369594700e-028
	2.842601052750101700e+001	6.847732063036272100e-030
	3.068552076752597200e+001	4.963819572032958300e-031
	3.304359923643782100e+001	9.353149492598748000e-033
	3.550232389114118800e+001	2.477969887040512000e-036
	3.806393216564647700e+001	4.239028331839452300e-037
	4.073083544445862000e+001	3.641705978592920500e-040
	4.350563546642152300e+001	4.693162136557847000e-042
	4.639114297861619500e+001	3.273369815880679000e-040
	4.939039902562468900e+001	1.557488885602912500e-045
	5.250669934134629800e+001	3.822206985836815500e-046
	5.574362241327836600e+001	1.191262857197502200e-049
	5.910506191901711000e+001	9.323680006297660900e-052
	6.259526440015140000e+001	7.976869273546082900e-054
	6.621887325124757200e+001	5.219071569119694000e-056
	6.998098037714683500e+001	3.904136096143558400e-058
	7.388718723248297200e+001	5.592589802340097000e-060
	7.794367743446311200e+001	7.651876828365938700e-062
	8.215730377831930300e+001	1.507973665785066200e-063
	8.653569334945652300e+001	2.321661390839127500e-065
	9.108737561313309100e+001	7.656186019990635200e-067
	9.582194001552072400e+001	4.277368680180562400e-069
	1.007502319695139800e+002	3.339714045147446100e-068
	1.058845994687999500e+002	9.625807392322787400e-073
	1.112392075244395800e+002	2.203134526676485400e-074
	1.168304450513065000e+002	6.917103195369895900e-077
	1.226774602685385800e+002	3.404613344948213900e-079
	1.288028787692376800e+002	3.504365329816201200e-081
	1.352337879495258300e+002	3.947143262826829200e-083
	1.420031214899315200e+002	2.781905740189933700e-085
	1.491516659000493800e+002	2.923788481669623300e-087
	1.567310751326711800e+002	3.295799901148357000e-089
	1.648086026551505100e+002	2.913420199028532800e-091
	1.734749468364242700e+002	3.325505601588954800e-093
	1.828582046914314700e+002	2.286265357789005500e-095
	1.931511360370729200e+002	3.017203039257350600e-097
	2.046720284850594900e+002	1.003779494336297500e-097
	2.180318519353285200e+002	3.463751662603645000e-101
	2.348095726583815400e+002	1.709355475631221600e-105
80	1.796042330070719800e-002	4.527264146762074300e-002
	9.463991299436547200e-002	9.762269113123585300e-002
	2.326228681258748500e-001	1.336585279815846700e-001
	4.319925478024092000e-001	1.493764582616732000e-001
	6.928288613520345900e-001	1.458470697926569600e-001
	1.015232556189476200e+000	1.279804694604408100e-001
	1.399327687842864700e+000	1.024036457228953300e-001
	1.84526230383863500e+000	7.534407498025813600e-002
	2.353208871609254500e+000	5.124231201767415900e-002
	2.92336468655416800e+000	3.230914852011215100e-002
	3.555952314046138900e+000	1.902216362285802400e-002
	4.251220082309900200e+000	1.053567793380848400e-002
	5.009442633620182100e+000	4.208818962240315700e-003
	5.830921538608728300e+000	3.591156083304103900e-003
	6.715985977851300200e+000	6.772205575814261800e-006
	7.664993494891755100e+000	2.508766803475241100e-008
	8.678330825167703800e+000	3.759867176165261900e-010
	9.756414805742958100e+000	1.659874637272086300e-011
	1.089969337128785700e+001	1.067114171861033800e-014
	1.210864664236568600e+001	1.008829591167663400e-015
	1.338378811277864800e+001	8.111037989221677300e-018
	1.472566594350860200e+001	8.211325623456514500e-019
	1.613486437166245900e+001	1.571557668971245800e-023
	1.761200524381443300e+001	4.242463293547919300e-026
	1.915774968424125600e+001	2.952870665760292200e-028
	2.077279990979209900e+001	2.761193306529811400e-030
	2.245790120454041100e+001	1.295356751639924600e-032
	2.421384406895865000e+001	3.83461904449760600e-034
	2.604146656016558500e+001	1.067217131732532100e-035
	2.794165684185946200e+001	6.499051587621124900e-037
	2.991535596490099300e+001	1.084026126275292000e-038
	3.196356090220893600e+001	3.214303438606540700e-042
	3.408732786472619100e+001	1.629168641582820100e-044
	3.628777592878145700e+001	1.629156873502164300e-046
	3.856609100929222900e+001	1.438200394261472300e-048
	4.092353021803128100e+001	2.635535127575644500e-051
	4.336142665173121500e+001	5.050274418147276400e-053
	4.588119466127889000e+001	2.711720765061552100e-055

Table D.1.: Zeros and weights of the associated Laguerre polynomials for $n = 48, 64, 80$ and 96 .

n	Zeros	Weights
4.848433566083317500e+001	3.336043311659626600e-057	
5.117244454460700400e+001	6.308192966767756000e-059	
5.394721678955443200e+001	4.386669111833254500e-060	
5.681045633463621400e+001	7.366544509640817400e-061	
5.976408434210994600e+001	1.249150569455572800e-063	
6.281014896392648000e+001	8.908420322799617000e-066	
6.595083625745606100e+001	6.793854132641378400e-069	
6.918848242023628400e+001	1.284310120314103800e-070	
7.252558754426334500e+001	9.705454120663609600e-073	
7.596483112786417300e+001	1.750563656508454900e-074	
7.950908962908883400e+001	5.256726686436844300e-076	
8.316145640105368400e+001	9.325733728039360500e-078	
8.692526441961563000e+001	2.172484652622407100e-077	
9.080411230094075800e+001	7.516946782002685700e-081	
9.480189421594744200e+001	1.297702308404737400e-083	
9.892283444694058400e+001	1.741262232776274400e-085	
1.031715275080391300e+002	8.519685961085303000e-088	
1.075529849775399100e+002	6.807112452098160900e-090	
1.120726904841283300e+002	1.583318314955419000e-091	
1.167366646735036700e+002	6.792847822949990100e-094	
1.215515424909526300e+002	6.841361259613952000e-096	
1.265246657965155500e+002	1.081781934882235700e-097	
1.316641952521202900e+002	1.119123325432105300e-099	
1.369792466869369900e+002	1.837578897402000600e-101	
1.424800589121616100e+002	1.959227119570111100e-103	
1.481782024550044500e+002	1.910170450806438900e-105	
1.540868422817987100e+002	3.967732895328394700e-107	
1.602210728700957200e+002	2.407522466378377200e-109	
1.665983519340539400e+002	4.817350446172285700e-111	
1.732390713342495000e+002	3.365444524362328000e-113	
1.801673230490323200e+002	2.248084507883307400e-115	
1.874119496769637900e+002	3.655607340270085300e-117	
1.950080224415329700e+002	3.305794249391232000e-119	
2.029989841950749400e+002	3.548550834729651200e-121	
2.114398704948364700e+002	1.990079747392337500e-123	
2.204023681517357400e+002	1.191354953738333200e-125	
2.299832060756799900e+002	1.163853564180680300e-127	
2.403190870558415500e+002	3.531876600593746000e-130	
2.516158793304996100e+002	5.332993059655588100e-132	
2.642138238831991000e+002	2.397135229453975000e-134	
2.787667330460045600e+002	8.214272628890142800e-135	
2.969665119956259200e+002	4.035034118907877600e-140	
96 1.498247386281096500e-002	3.787857622568759800e-002	
7.894612304879709800e-002	8.271990609731048900e-002	
1.940394361941618900e-001	1.158667991376338700e-001	
3.603184994030259000e-001	1.338323000929583200e-001	
5.778305997114303600e-001	1.364333038349365100e-001	
8.466343334083689100e-001	1.262862173442002300e-001	
1.166801575278799000e+000	1.076924233651582600e-001	
1.538417935202949400e+000	8.532454746187034800e-002	
1.961582977838271800e+000	6.314354364833571500e-002	
2.436410401398999300e+000	4.375348198808660200e-002	
2.963028219390469800e+000	2.906326439211654200e-002	
3.541578958083532400e+000	1.422949729137813400e-002	
4.172219874479179000e+000	1.654470481226620900e-001	
4.855123197087318800e+000	3.635937215398905800e-005	
5.590476391052785500e+000	4.593537356401419600e-007	
6.378482448916909000e+000	3.875523739754360400e-009	
7.219360208264735200e+000	1.561261879108512900e-009	
8.113344697561959900e+000	1.064119237782156500e-013	
9.060687511578658300e+000	7.179698765530639200e-016	
1.006165721792037200e+001	5.224038125371649200e-018	
1.111653979632728800e+001	5.335399716981233200e-021	
1.222563911256062900e+001	5.216582935449323700e-023	
1.338927742886799000e+001	1.421269396226435800e-024	
1.460779595321225700e+001	9.171164135114507300e-027	
1.588155542965692000e+001	1.238792872288592600e-028	
1.721093677253059400e+001	7.523912264270735300e-031	
1.859634174724747900e+001	5.883171929513453700e-034	
2.003819370093648200e+001	4.056129821003099700e-036	
2.153693834634003700e+001	3.497432382671259600e-038	
2.309304460278017500e+001	1.494388589964424300e-039	
2.470700549836556800e+001	5.320254815865791300e-042	
2.637933913802543600e+001	2.681216348436071500e-042	
2.811058974241968400e+001	3.230555782810911800e-045	
2.990132876328394900e+001	5.248292568929479500e-047	
3.175215608134193300e+001	1.185965527784803600e-050	
3.366370129355205900e+001	3.682504798251326200e-052	
3.563662509717134000e+001	4.178181132349400300e-053	
3.767162077891715200e+001	4.925450824988014500e-057	

Table D.1.: Zeros and weights of the associated Laguerre polynomials for $n = 48, 64, 80$ and 96 .

n	Zeros	Weights
	3.976941581840657800e+001	4.069234421113295300e-059
	4.193077361606334100e+001	1.774235923907944000e-061
	4.415649535682295100e+001	1.570851401561874700e-063
	4.644742202225501200e+001	8.680321716649747500e-066
	4.880443656518196600e+001	3.349789262178658400e-067
	5.122846626253059600e+001	2.539979521575203600e-069
	5.372048526403948200e+001	2.432677382828968200e-071
	5.628151735659689300e+001	5.621280789990370300e-073
	5.891263896644577600e+001	2.931112700354419500e-074
	6.161498242431208200e+001	7.589676011003365700e-077
	6.438973952175925300e+001	3.171113223431756100e-079
	6.723816539080927200e+001	9.564923260770186200e-081
	7.016158274319579400e+001	2.626039043173193400e-083
	7.316138651062802000e+001	1.065996689026329300e-085
	7.623904893327643600e+001	2.349606364108156100e-087
	7.939612515049825000e+001	2.185462648243589800e-089
	8.263425935578989400e+001	2.957523965241690300e-091
	8.595519158731968900e+001	1.766859347059714300e-093
	8.936076523643990300e+001	2.441095800050822600e-095
	9.285293536965613700e+001	4.839299177688167700e-097
	9.643377797507984900e+001	4.840753097602172700e-099
	1.001055002629519200e+002	2.981178270772608500e-101
	1.038704521720840100e+002	3.381966880312950900e-103
	1.077311392608829300e+002	6.926882256546050000e-105
	1.116902371940922800e+002	1.295679236785464700e-106
	1.157506080759045700e+002	1.713058909422790500e-108
	1.199153189284560000e+002	4.146969600262774500e-110
	1.241876626742425700e+002	8.066072576386799000e-112
	1.285711820547140900e+002	6.524709317187296200e-113
	1.330696970091988800e+002	1.725464563941738000e-112
	1.376873361536594600e+002	3.026493048979237900e-116
	1.424285731446393600e+002	2.505937310716265200e-118
	1.472982688996606300e+002	6.150865037950803900e-119
	1.523017208842670400e+002	3.722337758653483900e-123
	1.574447209857949600e+002	7.698524048336874200e-125
	1.627336238997838800e+002	2.105004975435383900e-127
	1.681754284920079400e+002	4.333685345664241000e-129
	1.737778753179440500e+002	4.343384059829623400e-131
	1.795495644554947900e+002	1.326181355022098900e-132
	1.855000991442821600e+002	3.081098809377627800e-134
	1.916402625884897500e+002	4.964711352385594000e-137
	1.979822379189962200e+002	3.664863478218732500e-139
	2.045398851133784300e+002	3.797192677830058200e-141
	2.113290942611680000e+002	7.250513928941797300e-143
	2.183682429565865800e+002	4.316500383513183200e-145
	2.256787985234694500e+002	2.887311341020676100e-147
	2.332861262278312300e+002	3.366992026455963600e-149
	2.412205980367763200e+002	1.568217122211036000e-151
	2.495191530625291400e+002	7.627106723856238000e-154
	2.582275608164192700e+002	4.179419163653824900e-156
	2.674038241570986000e+002	2.963101623369087900e-158
	2.771235253160818400e+002	1.182662197104633800e-160
	2.874886968264098600e+002	3.685347627611598500e-163
	2.986436136993047500e+002	7.372462276742866200e-166
	3.108056796861862400e+002	2.623189922065000300e-168
	3.243344504123146500e+002	2.292667036183474900e-171
	3.399214093107306700e+002	1.583889927212473700e-174
	3.593576199950017000e+002	3.782482022694820000e-178

Table D.1.: Zeros and weights of the associated Laguerre polynomials for $n = 48$, 64, 80 and 96.

Paper I

Modelling of combustion noise with the Boundary Element Method and Equivalent Source Method

H. Brick^{a,b}, R. Piscoya^{a,b}, M. Ochmann^a and P. Költzsch^b

^aTFH Berlin – University of Applied Sciences, FB II – Mathematics, Physics and Chemistry,
Luxemburger Str. 10, 13353 Berlin, Germany

^bTechnical University Dresden, Department of Electrical Engineering and Information
Technology, Laboratory of Acoustics and Speech Communication, 01062 Dresden, Germany

^a[brick;piscoya;ochmann]@tfh-berlin.de; ^bPeter.Koeltzsch@ias.et.tu-dresden.de

Abstract [546] The research project “Combustion Noise” concentrates on the development of methods for the prediction and minimisation of the noise generation by combustion in general and for aircraft engines in particular. In the present subproject the application of the acoustical Boundary Element Method (BEM) and Equivalent Source Method (ESM) for the prediction of noise from a free diffusion flame is investigated. These acoustical methods have been coupled with a Computational Fluid Dynamics-technique to describe the noise from the combustion process. The coupling of the BEM/ESM and the CFD-Simulation is realised on a Kirchhoff-surface. As coupling variables the normal velocity on the Kirchhoff-surface is used. The coupling was realised on different cylindrical surfaces with increasing radii around the centre of the flame. The results for the radiated sound power of the diffusion flame depending on the distance of the surfaces from the flame centre is discussed.

1 INTRODUCTION

The subject of interest, an open diffusion jet flame, is characterised by turbulent flow-fields, chemical reactions, heat transfer and the interaction of these processes. The governing equations of the combustion process are solved by a Large Eddy Simulation (LES), a powerful numerical technique from Computational Fluid Dynamics. The fluctuations of physical quantities that act as sound sources are calculated in a small computational domain around the flame with high time and spatial resolution. The sound field generated by those sources, in particular at large distances, can be computed in a faster and more efficient way by using the calculated fluctuations as input data for acoustical methods. The acoustic analogy (AA) or the linearized Euler equations (LEE) are often used as the coupling procedure to determine the sound field [3]. In the present work, the CFD domain is coupled to the radiation zone by a control surface, the Kirchhoff-surface, which must enclose all acoustical sources of the flame and has to be located in an homogeneous environment free of flow and temperature gradient. On this Kirchhoff-surface the normal velocity as Neumann boundary condition for the acoustic radiation problem is obtained from the LES calculation. This coupling is referred to as the Kirchhoff-method. The advantage of the Kirchhoff-Method is that only the surface integral on the control surface has to be evaluated to calculate the radiated sound field in the radiation zone, its possible drawback

is the requirement of no flow and no temperature gradients outside the control surface. Hence, the positioning of the control surface and the exact description of the acoustic quantities on this surface are the sensitive points of the Kirchhoff–method.

In order to examine the influence of the position of the control surface, the sound radiation of different control surfaces with varying distance from the flame centre was studied. Since flow and temperature gradient decline with increasing distance to the flame the sound radiation should converge to the true value with increasing radius of the control surface.

2 THE ACOUSTIC METHODS

While the BEM solves the Helmholtz–Integral–Equation for exterior field problems on the control surface of the structure, the ESM replaces the original sound source with a system of acoustical elementary sources inside this control surface which satisfy the wave equation and radiation condition in the ambient medium and fulfil the boundary conditions on the surface. Detailed descriptions of these acoustical methods can be found e.g. in [8], [12]. Both methods are well approved for the calculation of the sound radiation from structure–borne sound. Up to now there are only few attempts to apply these methods in the field of thermo– or flowacoustics [3].

3 COMPUTATIONAL MODEL

3.1 Flame model

The flame model is a turbulent hydrogen jet diffusion flame, combusting a highly diluted mixture of H_2 and N_2 at the volume ratio of 23 : 77. The stoichiometric mixture fraction is $f_{stoic} = 0.583$. The fuel was diluted in order to slow down the chemical reactions, i.e. to stabilise the numerical simulation. Due to the high dilution the flame burns close to its blow-off limit. The circular nozzle diameter is $D = 8$ mm and the fuel discharges with a bulk velocity of $U_{bulk} = 36.3$ m/s into air co-flowing at $U_{coflow} = 0.2$ m. The corresponding Reynolds-number is 16000. The flame was numerically and experimentally investigated in detail at the Technical University of Darmstadt [4],[5].

The Large-Eddy-Simulation (LES) of the flame was executed on a cylindrical computational domain of 48 nozzle diameters D length and radius $30D$. The numerical grid consisted of $257 \times 32 \times 60$ (axial \times circumferential \times radial) cells. The simulation based on the steady Flamelet model and the presumed-pdf method. The used numerical method assumes density to be independent of pressure (incompressibility), which is a widespread approximation within the methods of computational fluid dynamics for the considered low Mach number flow. The LES-code was developed at the Technical University Darmstadt, Institute for Energy and Powerplant Technology. More detailed information about the used LES-model for turbulent diffusion flames can be found in publications of this institute [4], [11]. For the acoustic calculations, velocity samples at spatial points on ten cylindrical surfaces with radii varying from $R = [6.7, 7.3, 7.9, 8.6, 9.3, 10.0, 10.8, 11.7, 12.6, 13.6]D$ and constant length $L = 47.8D$ were excerpted from the LES calculation within a timeframe of $0.17 \cdot 10^{-1}s$ with a sampling rate of approximately 10000 Hz. The time series of the velocity were transformed into the frequency domain by means of the Fourier transform before serving as input data for the BEM or ESM.

3.2 Acoustic model

From the point distribution given by the LES surface meshes of ten cylindrical control surfaces were generated. To save computing time and memory the number of axial points was much

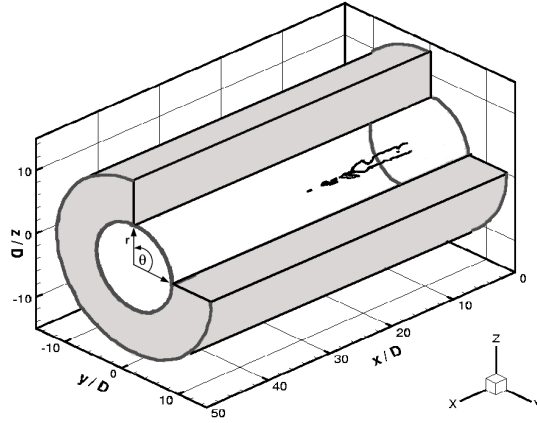


Figure 1: *Domain of the LES velocity samples at cylindrical surfaces around the flame (gray area). The black line indicates the contour of the stoichiometric mixture fraction of the flame.*

reduced to build the surface meshes, i.e. the grid of the cylindrical area was reduced to 33×32 points for the smallest cylinder with $R_1 = 6.7D$ and 19×32 points for the biggest cylinder with $R_{10} = 13.6D$. The surface mesh for the cylinder of largest radius fulfills the requirement of six grid points per wavelength up to a frequency of $f_{max} = 3000$ Hz.

BEM

The BEM for the calculation of the sound radiation of the presented Neumann problem does not have a unique solution at the characteristic eigenfrequencies of the associated interior Dirichlet problem. The CHIEF method was chosen to remedy the non-uniqueness at these eigenfrequencies. A brief description of the CHIEF method can be found in [12]. Tests showed, that ten equidistant CHIEF points at the axis of the cylinders provide satisfactory results at the occurring characteristic eigenfrequencies. More details of the used BEM application and test procedure are described in a former paper [1].

ESM

An ESM model is characterised by the distribution of acoustical elementary sources inside the control surface. For the presented problem three different distributions of the source positions were tested: a) 20 sources along the cylinder axis, b) 32 sources in parallel rings and c) 30 sources in random positions over a smaller cylindrical shell of radius $0.5R$ and length $0.6L$ (see Fig. 2). In each position, sources of zeroth, first and second order were considered, which correspond to monopoles, dipoles and quadrupoles. The results presented in this paper correspond to

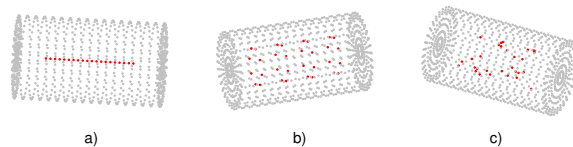


Figure 2: *The three different distributions of source positions inside the mesh of the cylindrical control surface.*

configuration a) in Fig. 2. The results obtained by the other configuration do not differ notably from this configuration.

4 RESULTS

Starting from the given normal velocity distributions at the ten cylindrical surfaces as the results of the LES, the pressure distributions at the same surfaces were calculated by the BEM and the ESM for a set of frequencies. The sound power is then computed by integrating the acoustic intensity over the control surfaces. Fig. 3 shows the radiated sound power P calculated by the BEM for each cylinder. But the curves of the sound power are hardly plausible. The expected

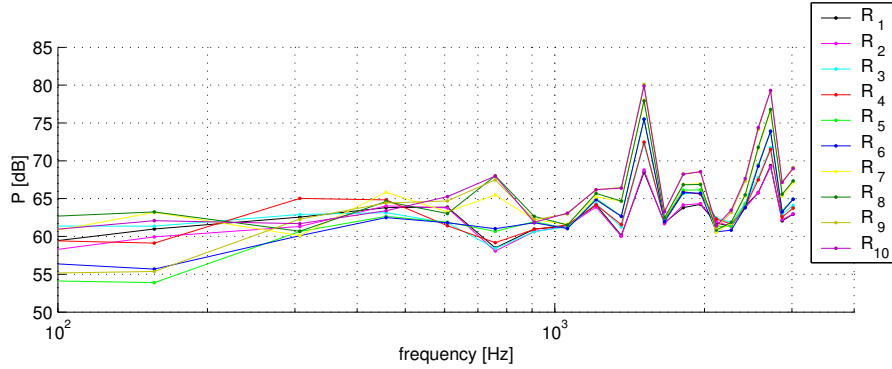


Figure 3: *Sound power radiated by the ten control surfaces around the flame*

convergence of the radiated sound power with increasing radii of the control surface can not be observed. Also, the distinctive peaks in the higher frequency range are not assumed from a real flame. Diffusion flames as the present flame should show an intense sound radiation in the lower frequency range declining with the frequency [6], [7], [9], [10]. A closer examination revealed, that the sound power radiation depends mainly on the velocity spectrum of the centre of the inflow plane. Fig. 4 shows the velocity spectrum of the centre in comparison with other points of the inflow plane. Only the spectrum of the centre point has considerable high

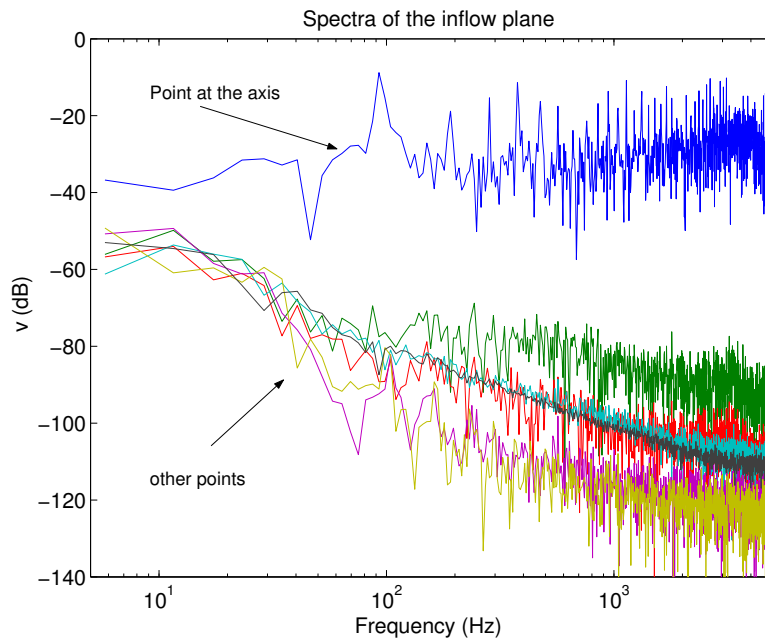


Figure 4: *Velocity spectrum of the centre and other points of the inflow plane of the cylindrical control surface*

frequency components, all other points show a strong decay with the frequency. The Large Eddy Simulation defines at this point an artificial turbulence as boundary condition. This artificial turbulence with extreme high amplitudes over the whole frequency range is an unphysical value, which obviously disturbs the acoustic approach. Fig. 5 show the sound intensity radiated by the tenth control surface in the x,z -plane at the frequency = 1511 Hz (first peak of the radiated sound power, see Fig. 3). The centre point of the inflow plane is clearly identifiable as the main sound source. In order to remedy this numerical perturbation from the inflow condition of the

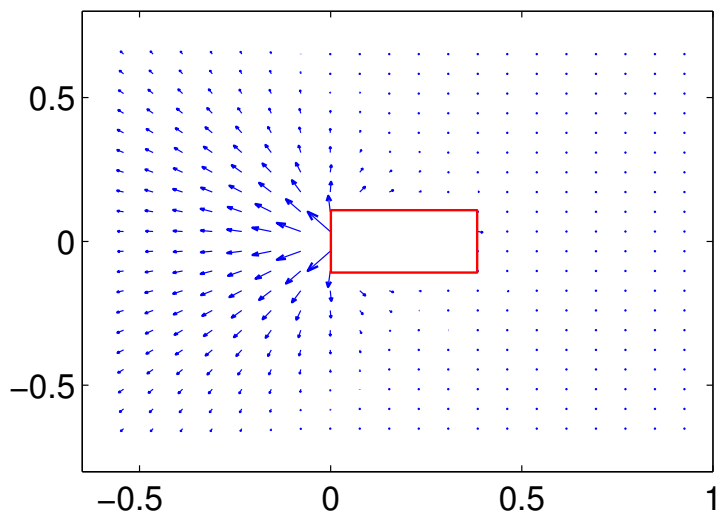


Figure 5: *Sound intensity radiated by the tenth control surface at a frequency = 2700 Hz. The centre of the inflow plane appears as main source of the sound radiation.*

LES model the normal velocity of the inflow plane was set at zero. As it can be seen in Fig. 6 the unfamiliar peaks of the radiated sound power disappear, the differences between the sound power of the different control surfaces are reduced and the radiated sound power decays with the frequency for all surfaces. Altogether, the sound power spectra in Fig. 6 seem to be a more reasonable representation of the sound radiation from an open flame than these in Fig. 3. In Fig. 7 the radiated sound intensity is plotted which results from the new condition. Here the sound is radiated mainly in direction of the flow.

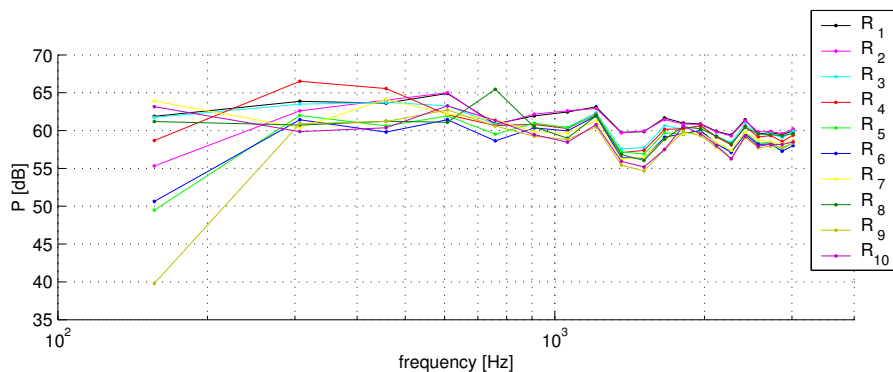


Figure 6: *Radiated sound power of the ten control surfaces with the normal velocity on the inflow plane set at zero*

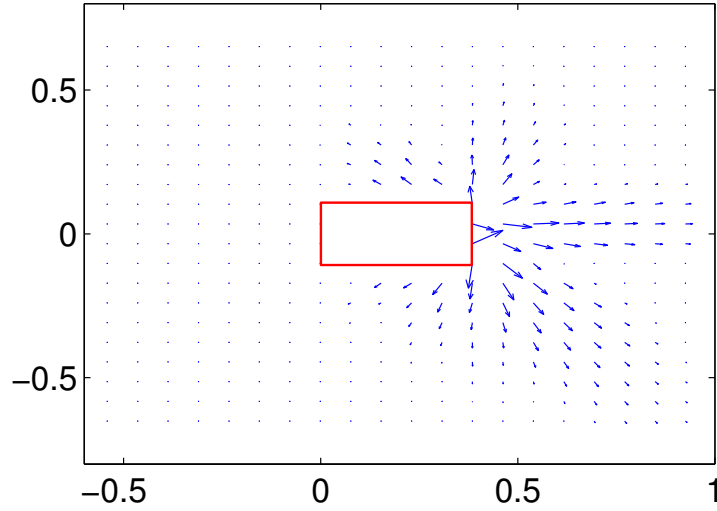


Figure 7: Sound intensity radiated by the tenth control surface at a frequency = 2700 Hz. The normal velocity at the inflow plane ($x = 0$) is set at zero.

Fig.8 shows the difference $\Delta L = L_{BEM} - L_{ESM}$ of the BEM and the ESM calculation in dB. Apart from the lowest frequencies the discrepancy of the results is marginal, though both methods follow a different approach. This result is very positive, especially in face of the future process, since both methods can approve themselves mutually.

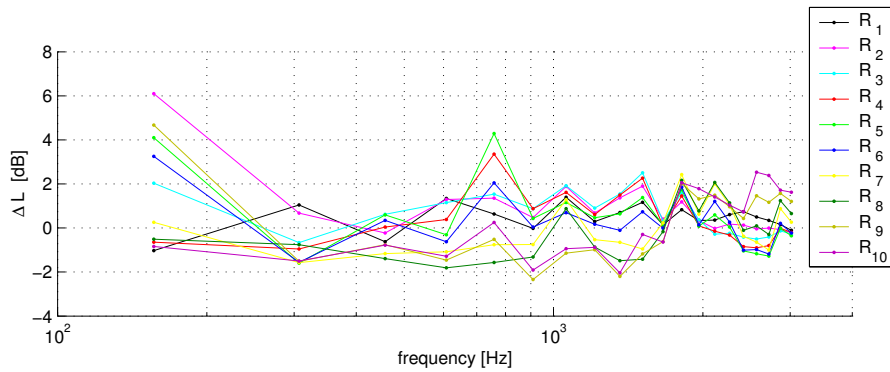


Figure 8: Difference of the radiated sound power calculated by BEM and ESM, $\Delta L = L_{BEM} - L_{ESM}$

5 CONCLUSIONS

The radiated sound power of an open diffusion jet flame was calculated by the Kirchhoff-method, which is characterised by the coupling of a Large Eddy Simulation with the Boundary Element Method or the Equivalent Source Method as acoustic methods based on the Helmholtz-equation. The BEM and the ESM calculations show nearly the same results. The influence of the position of the coupling surface was studied by varying the radius of the cylindrical surface around the centre of the flame. Beside the characteristics of the surface also the influence of the boundary conditions of the LES was examined. Especially the inflow boundary condition seems to disturb the acoustic calculations. Neglecting the velocity on the inflow plane by setting the values in this area at zero the assumed convergence of the radiated sound power for the different coupling surfaces could be shown. The transfer of boundary conditions from one

model to another has to be reviewed carefully in the further progress of the research project. The small deviations originate possibly from the flow or temperature gradients in the ambient environment of the Kirchhoff-surface. The influence of the assumption of incompressibility, implied by the LES, on the acoustic calculations has not been studied yet.

The present work does not present the Kirchhoff-Method for the calculation of combustion noise as readily elaborated, but it discusses the possibilities and difficulties of this method. The planned experimental examination of the sound radiation from a diffusion flame will be an important step for the validation of the method.

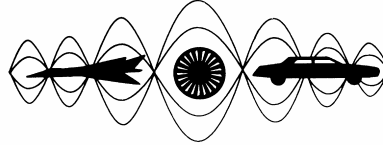
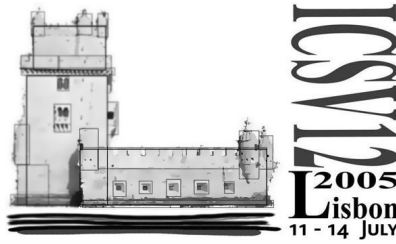
ACKNOWLEDGEMENTS

We thank Prof. Janicka and Mr. Flemming from the TU Darmstadt for the cooperation and for putting the data of the LES calculations to our disposal. This work is integrated in the research project "Combustion Noise", supported by the German Research Foundation (DFG), [2].

REFERENCES

- [1] Brick, H., Ochmann, M., Brenck, E., "Simulation of the sound radiation from wheel-like structures using the boundary element method" in *Forum Acusticum*, Sevilla, 2002.
 - [2] Combustion Noise Initiative, URL: <http://www.combustion-noise.de>
 - [3] Hüttl, T., Wagner, C., Delfs, J., LES for Acoustics, Proceedings, Göttingen, Germany, October 2002.
 - [4] Kempf, A., Large Eddy Simulation of Nonpremixed Flames, Dissertation, TU Darmstadt, 2003.
 - [5] Kempf, A., Sadiki, A. and Janicka, J., "Prediction of Finite Chemistry Effects using Large-Eddy Simulation" in *Proc. Comb. Inst. 29*, 2002.
 - [6] Klein, S. A., On the acoustics of turbulent non-premixed flames, Dissertation, Universiteit Twente, 2000.
 - [7] Lenze, B., Pauls, D., Die Entstehung und Bekämpfung von Brennergeräuschen, *gwf-gas/erdgas* **115**, (1974).
 - [8] Ochmann, M., The Source Simulation Technique for Acoustic Radiation Problem, *Acustica* **81**, pp. 512–527, (1995).
 - [9] Ohiwa, N., Tanaka, K., Yamaguchi, S., Noise Characteristics of Turbulent Diffusion Flames with Coherent Structure, *Combustion Science and Technology*, Vol. **90**, pp. 61–78, (1993).
 - [10] Stephenson, J., Hassan, H. A., The Spectrum of combustion-generated noise, *Journal of Sound and Vibration* **53**(2), pp. 283–288, (1977).
 - [11] Tacke, M., Zur Stabilität angehobener turbulenter Diffusionsflammen, Dissertation, TU Darmstadt, 1998.
 - [12] Wu, T. W., Boundary Element Acoustics: Fundamental and Computer Codes, WIT Press, Southampton, Boston, 2000.
-

Paper II



Twelfth International Congress
on Sound and Vibration

A HYBRID APPROACH FOR THE EVALUATION OF THE RADIATED NOISE FROM A TURBULENT NON-PREMIXED JET FLAME BASED ON LARGE EDDY SIMULATION AND EQUIVALENT SOURCE & BOUNDARY ELEMENT METHODS

F. Flemming¹, A. Nauert¹, A. Sadiki¹, J. Janicka¹
H. Brick², R. Piscoya², M. Ochmann³, P. Költzsch²

¹Institute for Energy and Powerplant Technology
Petersenstr. 30, D-64287 Darmstadt, Germany
Darmstadt University of Technology
flemming@ekt.tu-darmstadt.de

²Institut für Akustik und Sprachkommunikation
Helmholtzstr. 18, D-01062 Dresden, Germany
TU Dresden

³Fachbereich II, Mathematik, Physik, Chemie
Luxemburger Str. 10, D-13353 Berlin, Germany
TFH Berlin

Abstract

A hybrid approach based on large eddy simulation (LES) and the equivalent source method (ESM) as well as the boundary element method (BEM) is applied to evaluate the noise radiation of open turbulent non-premixed jet flames. Hybrid approaches are well known and often used for classical non-reacting turbulent flows. The extension to turbulent reacting flows is presented here. For an open flame there is no strong influence of the acoustic field onto the flame. This is in contrast to enclosed flames, where the acoustic waves can easily induce combustion instabilities. Therefore, the flow simulation can be decoupled from the acoustic simulation. Furthermore, the very low Mach number of turbulent jet flames allows for an efficient incompressible formulation of the LES. From the instationary flow field resulting from the LES, the required information on a control surface or interface to the

acoustic method (ESM/BEM) can be extracted. By using two separate and specialized methods for the flow simulation and the acoustic simulation the large disparity of lengthscales in this problem can be exploited and the far field noise emission of the turbulent flame can be predicted at reasonable computational cost. The hybrid approach discussed above is shown to yield good results. Diluted non premixed hydrogen flames are considered and the results are compared to measurements of the flow field, the thermodynamical state of the fluid, as well as to acoustic measurements of the radiated sound power. These extensive comparisons validate not only the different numerical methods used, but also the complete hybrid approach presented.

INTRODUCTION

Hybrid approaches for the investigation of noise resulting from flow phenomena are widely used and a well accepted approach in the area of aeroacoustics [1], [2]. Especially in low Mach number flows, the fluid dynamical and acoustical lengthscales are separated by more than an order of magnitude. This allows the application of specialized techniques for each domain, namely the source region using computational fluid dynamics (CFD) and the acoustic propagation region all the way into the far field using computational aeroacoustics (CAA). Such a hybrid approach of an incompressible large eddy simulation (LES) for the fluid part and equivalent source or boundary element methods (ESM/BEM) for the acoustic part is applied to open, non-premixed turbulent jet flames in the present contribution. Especially for open turbulent combustion systems, the low Mach number approximation is applicable and hence an incompressible simulation saves computational costs and yields good results [3].

The use of instationary CFD such as the LES method is preferable, since here the turbulent spectrum does not have to be modeled completely. Therefore, conclusions of the sound output of such configurations can directly be drawn. In the case of a stationary RANS approach for the CFD part, the turbulent spectrum and therefore also the noise producing structures have to be modeled, limiting the general applicability of the hybrid approach. Finally, a direct approach, such as DNS of the flow field is beyond any feasible computational cost for technically relevant systems.

CONFIGURATION AND NUMERICAL APPROACH

The goal of this work is to predict and describe the direct combustion noise generated by turbulent non-premixed flames. For this purpose well investigated benchmark flames are used as a first target of investigation. The so called H3 flame, a benchmark flame of the TNF Workshop [4], as well as a slightly modified version, the HD flame [5], are simulated by means of LES and ESM/BEM. The flames consist of a simple round nozzle through which the fuel jet is injected coaxially into a slow coflow of air. The different parameters of the two flames are summarized in the following table 1.

Flame	Fuel [vol%]	D [mm]	U_{jet} [m/s]	U_{coflow} [m/s]	Re	f_{stoic}
H3	50/50 H ₂ /N ₂	8	34.8	0.2	10,000	0.310
HD	23/77 H ₂ /N ₂	8	36.3	0.2	16,000	0.583

Table 1: Parameters of the two standard flames studied.

Large Eddy Simulation of the Flow Field

The well known Favre-filtered (Favre: density weighted) transport equations for mass and momentum, as well as the conserved scalar mixture fraction are solved. Here, the mixture fraction stands for a dimensionless enthalpy or element conservation equation. This is a well known approach for turbulent non-premixed combustion systems, usually called the Shvab-Zeldovich formalism [6]. The required chemical state, like the density or temperature is mapped as a function of the mixture fraction and then coupled back into the solver. Using this approach, a low Mach number approximation can be used for the reacting flow, where the density is not constant, but no function of the pressure at the same time. This is the characteristic property of an incompressible formulation with variable density.

The governing equations are solved on a staggered cylindrical grid of $513 \times 32 \times 60 \approx 1.0 \cdot 10^6$ cells in axial \times tangential \times radial direction by the incompressible LES code *FLOWSI*. The code uses a 2nd order central scheme for the spatial derivatives in combination with a non-linear total variation diminishing (TVD, here CHARM) scheme for the steep gradients in the convective scalar transport. The time integration is performed by an explicit 3rd order low storage Runge-Kutta scheme. A Smagorinsky model with the dynamic procedure by Germano is applied to model the unclosed subgrid scales [7]. The chemical system is described by a steady flamelet approach integrated in a pre-processing step with a presumed β -PDF to model turbulence chemistry interaction [6]. The mean inflow profiles are superposed by artificially generated turbulence [8], while at the outflow a Neumann condition is applied. The circumferential outer boundary is described with a simplified momentum equation to allow for entrainment of fluid. For a detailed description of the current LES approach, please refer to the following publication [9].

Simulation of the Acoustic Far Field

Based on the velocity data prescribed on a control surface, which encloses the flame source region the equivalent source method (ESM) as well as the boundary element method (BEM) are able to determine the acoustical field outside the control surface by evaluating the surface data [10], [11]. This is less computationally expensive than the evaluation of volumetric data by using Lighthill's Analogy for example.

The ESM replaces the original sound sources with a system of acoustical elementary sources inside the control surface which satisfy the wave equation and radiation condition in the ambient medium and fulfil the boundary conditions on the interface, here the given velocity in normal direction of the surface. The acoustical

field outside the control surface is described by the superposition of all the acoustical elementary sources. Details for the used ESM, like positioning and characteristics of the equivalent sources can be found in [12] and [13].

The BEM can be regarded as a special kind of equivalent source method. The equivalent sources are no longer located inside the control surface, but are moved to the surface itself. They are restricted to monopoles and dipoles. The elements of the discretized surface represent a set of a monopole and a dipole sources, respectively. By means of the Helmholtz-Integral-Equation (HIE) a system of equations can be set up for the pressure $p(x)$ on the Kirchhoff-Surface.

$$\iint_S \left[-p(y) \frac{g(x,y)}{\partial n(y)} - j\omega \rho v_{ns} g(x,y) \right] dS = \frac{1}{2} p(x); \quad x, y \text{ on the surface} \quad (1)$$

The Green's function $g(x,y)$ in the HIE is given by the fundamental solution of the wave equation in the unbounded three dimensional space,

$$g(x,y) = \frac{e^{-jkr}}{4\pi r} \quad \text{and} \quad r = r(x,y) = \|y - x\|. \quad (2)$$

After solving the system of equations the pressure and normal velocity on the Kirchhoff-Surface are known and the sound field in the ambient medium can be calculated directly from these variables [11].

Coupling the two Approaches

The coupling between the LES and the ESM/BEM methods requires the exchange of instationary velocity data. Since both acoustic techniques use a control surface to extract the appropriate source terms, the same cylindrical interface can be used. As an important restriction, the interface needs to enclose the complete source region of the flame and must be located in a flow region where no more influence of the flame takes place and hence the fluid is nearly quiescent. The spatial as well as the temporal resolution need to be matched accordingly.

In the present case samples over a real time period of approximately 0.2 s with a resolution of 10 kHz were collected from the LES. The temporal signal is converted to the frequency domain by Fast Fourier Transform (FFT), using sections of 250 samples with a 50% overlap for subsequent averaging, still maintaining a resolution of 40Hz. A detailed description of the coupling technique can be found in [14].

ACOUSTIC MEASUREMENTS

To validate the numerical results the acoustical sound power of the flames was measured. The radiated sound power was obtained by measuring and integrating the sound intensity on a surface mesh around the flames. Additionally, the sound power of the isothermal flow was quantified for comparison.

Figure 1 shows the measured sound power density for the H3 and HD flame. The combustion process turns out to be the main source of sound. The sound power of the reactive flow is around 20 dB larger than that of the isothermal flow. While the isothermal flow shows distinct peaks of higher sound radiation, the flames emit broadband noise in a wide frequency range without tonal characteristics. Due to the strong similarity of the flames, the sound power spectra of the two flames do not vary substantially.

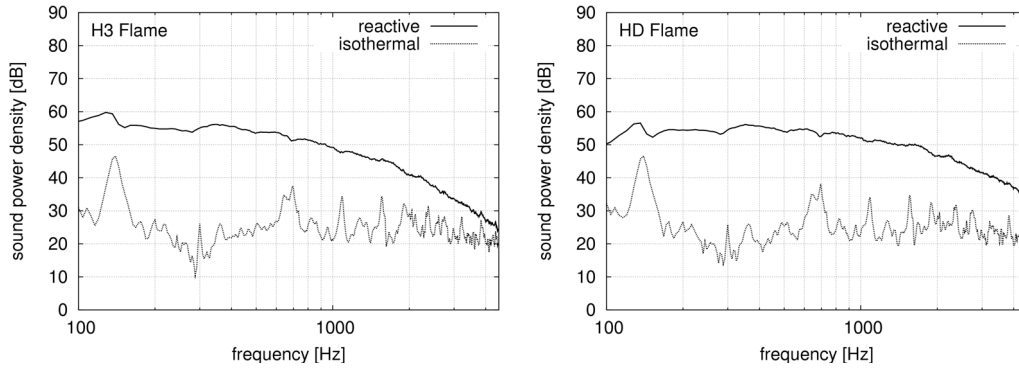


Figure 1: Measurements of the sound power density of the H3 and HD flame as well as the corresponding isothermal cases.

RESULTS

The use of LES allows the extraction of instantaneous views of the flow field. As mentioned before, this is one of the reasons, why such a simulation technique is that attractive for acoustic hybrid approaches. As an example of such fields, the mixture fraction, the temperature and the mass fraction of OH are shown in figure 2 for a single timestep. Large structures, as well as small structures can be observed.

Validation of the LES

In order to assess the quality of the LES, a detailed comparison of the statistics with experimental findings has to be performed. Here, the results of the TNF-workshop can be used to validate the flow field, as well as the distribution of chemical properties. In figure 3, the mean and standard deviation of different quantities in axial direction are presented for the H3 flame as a representative example. The agreement between experiment and simulation is evident. Only close to the nozzle, the level of velocity fluctuations is slightly overpredicted. This relates to the nozzle shear layer, which is not resolved properly by the LES. The effect is well known and reduces with grid resolution of the LES, but cannot be overcome otherwise.

Further radial comparisons at different axial positions are shown in figure 4. Mean values are presented in the left half of the graphs, while standard deviations are on the right side. Here the previous agreement of the LES is confirmed. The good

agreement of the temperature distributions is directly coupled to the mixture fraction, since only the chemistry model plays a determining role.

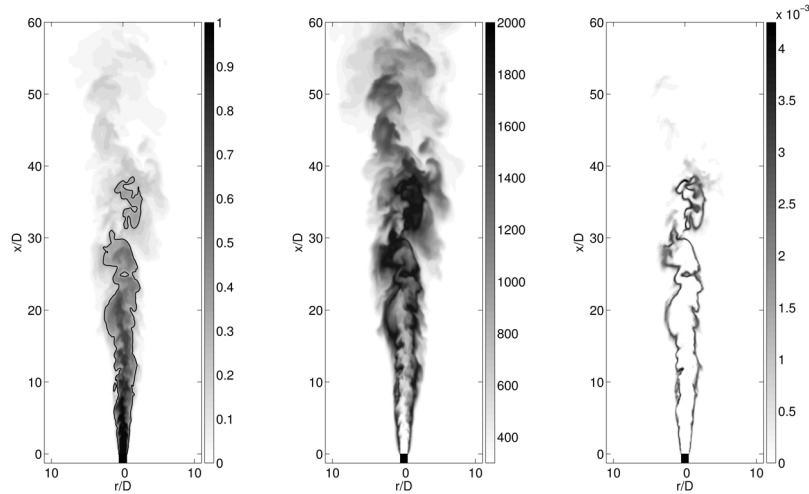


Figure 2: Instantaneous views of the mixture fraction [-] with the stoichiometric value highlighted by an iso-line, the temperature [K], and the OH mass fraction [-] as a marker for the flame front of the H3 flame.

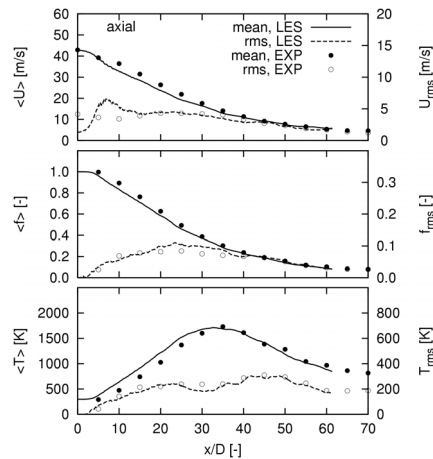


Figure 3: Axial distribution of mean and standard deviation of the axial velocity [m/s], the mixture fraction [-] and the temperature [K] for the H3 flame.

Resulting Acoustics

The calculation of the radiated sound power provides a direct comparison to the acoustical measurements. Figure 5 shows the resulting sound power density for the ESM and BEM simulations, compared to the measurements. The ESM and the BEM simulations lead to nearly the same results, only in the lower frequency range the ESM results differ slightly from the BEM results due to ill-conditioned matrices at these frequencies.

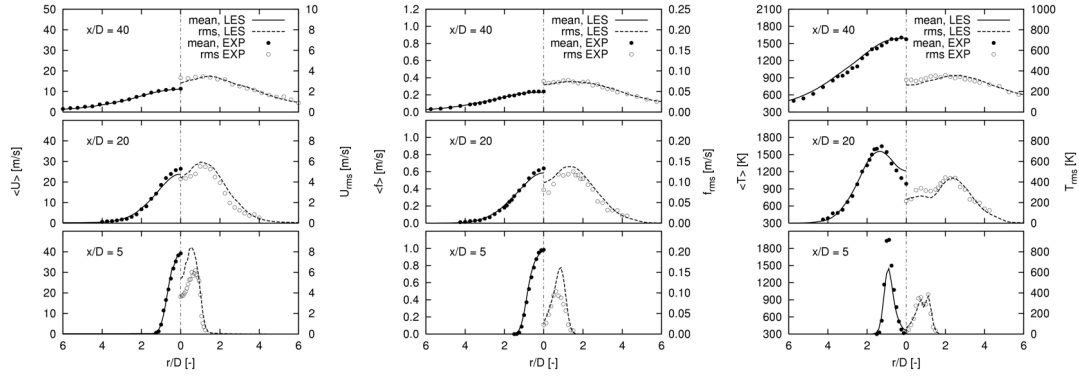


Figure 4: Radial distributions of mean and standard deviation of the axial velocity [m/s], the mixture fraction [-] and the temperature [K] at different axial positions for the H3 flame.

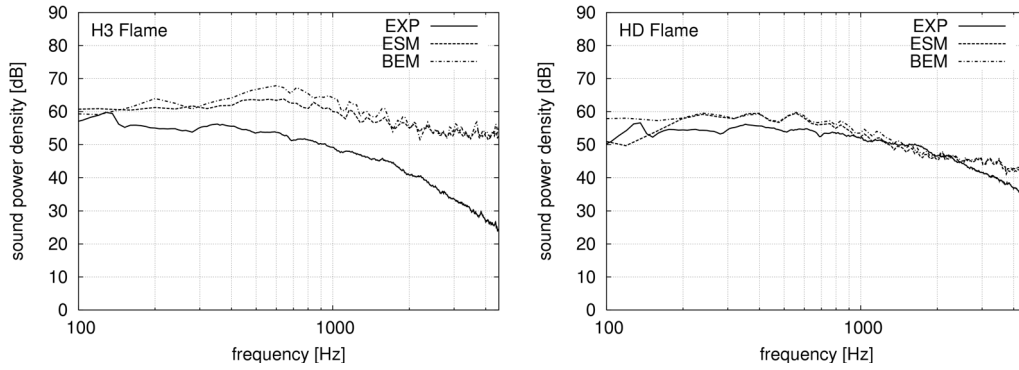


Figure 5: Comparison of the sound power density for the two configurations computed by ESM & BEM to the experimental results.

For the HD flame the resulting sound power is in good agreement with the measured spectra. The differences between simulation and measurement do not exceed 3 dB up to 2 kHz. Above 2 kHz the decrease of the sound power is not well reproduced by the simulations. In contrast the simulation results for the H3 flame differ notably from the measured spectra. The sound power is strongly overestimated in the considered frequency range. Here a turbulent velocity distribution of the closed control surface at the downstream end may disturb the acoustic simulations. The control surface encloses the entire source region, i.e. it enters the non-linear region at the downstream end of the domain. For the HD flame, which is the shorter flame, the turbulent sources have weakened sufficiently in this region. In other words, the ratio of the stoichiometric flame length to the axial extension of the LES domain was not the same in both simulations and might lead to such differences.

CONCLUSIONS

The use of a hybrid approach combining an incompressible LES with ESM and BEM was shown to yield good results for the acoustic far field of open turbulent non-

premixed jet flames. Certainly, further improvements are required in order to allow a detailed prediction of the combustion noise stemming from such configurations. Nevertheless, the approach is computationally efficient and very promising.

ACKNOWLEDGMENTS

The authors gratefully acknowledge the financial support by the German Research Council (DFG) through the Research Unit FOR 486 “Combustion Noise”.

REFERENCES

- [1] A. S. Lyrintzis, “Surface integral methods in computational aeroacoustics – From the (CFD) near-field to the (acoustic) far field”, *Int. J. of Aeroacoustics*, 2(2), 95-128 (2003)
- [2] T. Hüttl, C. Wagner, J. Delfs, (eds.), *Proceedings of the International Workshop on “LES for Acoustics”*, 7.-8. October, Göttingen, Germany (2002)
- [3] J. Janicka, A. Sadiki, “Large eddy simulation of turbulent combustion systems”, *Proc. Combust. Inst.*, 30, 537-547 (2005)
- [4] R. Barlow (ed.), *Proceedings of the TNF Workshop*, Sandia National Laboratories, Livermore, CA, www.ca.sandia.gov/TNF
- [5] M. Tacke, S. Linow, S. Geiss, E. Hassel, J. Janicka, J.-Y. Chen, “Experimental and numerical study of a highly diluted turbulent diffusion flame close to blowout”, *Proc. Combust. Inst.*, 27, 1139-1148 (1998)
- [6] W. P. Jones, “Turbulence modeling and numerical solution method for variable density and combusting flows”, *Turbulent Reacting Flows*, edited by P. A. Libbey and F. A. Williams, Academic Press, London, 309-374 (1994)
- [7] M. Germano, U. Piomelli, P. Moin, W. H. Cabot, “A dynamic subgrid-scale viscosity model”, *Phys. Fluids A*, 3(7), 1760-1765 (1991)
- [8] M. Klein, A. Sadiki, J. Janicka, “A digital filter based generation of inflow data for spatially developing direct numerical or large eddy simulations”, *J. Comput. Physics*, 186, 652-665 (2003)
- [9] A. Kempf, F. Flemming, J. Janicka, “Investigation of lengthscales, scalar dissipation, and flame orientation in a piloted diffusion flame by LES”, *Proc. Combust. Inst.*, 30, 557-565 (2005)
- [10] M. Ochmann, “The Source Simulation Technique for Acoustic Radiation Problems”, *Acustica* 81, 512-527 (1995)
- [11] T. W. Wu, *Boundary Element Acoustics: Fundamental and Computer Codes*, WIT Press, Southampton, Boston, (2000)
- [12] R. Piscoya, M. Ochmann, H. Brick, P. Költzsch, “Modelling of the combustion noise by means of the equivalent source method (ESM)”, *Proc. Joint Congress CFA/DAGA'04*, Strasbourg, France, 119-120 (2004)
- [13] R. Piscoya, H. Brick, M. Ochman, P. Költzsch, “Numerical aspects of the Equivalent Source Method applied to combustion noise”, *Proc. 12th Int. Congress on Sound and Vibration ICSV12*, Lisbon, Portugal (2005)
- [14] F. Flemming, A. Sadiki, J. Janicka, “Strategies for coupling large-eddy simulations with computational aeroacoustics”, *Proc. Joint Congress CFA/DAGA'04*, Strasbourg, France, 117-118 (2004)

Paper III

Prediction of the Sound Radiated from Open Flames by Coupling a Large Eddy Simulation and a Kirchhoff-Method

Haike Brick, Rafael Piscoya

Technical University Dresden, Institute for Acoustics and Speech Communication, 01062 Dresden, Germany, e-mail: {brick, piscoya}@tfh-berlin.de,

Martin Ochmann

TFH Berlin, FB II, Luxemburger Str. 10, 13353 Berlin, Germany, e-mail: ochmann@tfh-berlin.de,

Peter Költzsch

Technical University Dresden, Institute for Acoustics and Speech Communication, 01062 Dresden, Germany,
e-mail: Peter.Koeltzsch@ias.et.tu-dresden.de

Hybrid methods, coupling CFD codes and acoustic methods like the acoustic analogy, the linearised Euler equations and the Kirchhoff-Method are being used to predict the sound produced by turbulent combustion, since the present computational power only allows an accurate estimation of the physical quantities, in a reasonable computational time, near the source. This means that the acoustic far field cannot be determined by a direct simulation. This research attempts to show that the Equivalent Source Method (ESM) and the Boundary Element Method (BEM), which are considered as Kirchhoff-Methods, can also be used to determine the sound generated by combustion. These two methods have the advantage that only one acoustic variable must be known at a surface surrounding the source zone and that the far field can be directly computed. The sound power generated from two open diffusion flames have been calculated with both the ESM and the BEM, using the velocity distribution over cylindrical control surfaces computed with a Large Eddy Simulation. Results of the calculations are presented and compared with the measured sound power of the same flames. For one configuration good agreement between measurement and simulation at low and middle frequencies is obtained. Possible reasons for the differences for the other configuration will be discussed.

1 Introduction

In the German basic research project "Combustion noise" prediction tools for reduction of combustion noise are under development, [1]. This is an extremely complex task taking into account that it involves both the noise generation due to the processes in the reactive zone (i.e. turbulent flow and combustion) as well as the transport/radiation of noise through turbulent area to the surrounding. Due to its complexity a direct numerical simulation (DNS) is not possible and hybrid methods have to be applied. This means that the source region (reactive zone) is modelled typically with Computational Fluid Dynamic (CFD) codes, while the propagation is handled by standard acoustic methods such as the Kirchhoff-Integral or the linearized Euler equations. In this paper an approach is chosen where data are provided from incompressible Large Eddy Simulations on a defined surface around the flame. These data are then the input to a Boundary Element Model (BEM).

In the following the approach is described in detail. The results from the BEM are compared with results from the Equivalent Source Method (ESM) and measurements, which were carried out for two different flames. Additional measurements as the determination of the sound power levels of the isothermal flow as well as for varying Reynolds numbers have been made and will be also presented and discussed in this paper.

2 Numerical Approach

The numerical approach consists of three parts,

- the model of the flame which describes the processes in the source region,
- the Kirchhoff method which couples the source region to the surrounding medium and
- a BEM approach (and ESM approach respectively) predicting the radiated sound field.

These three parts are described in the following.

2.1 The flame model

The flames studied in this paper are open, non-premixed jet flames, whose properties were investigated thoroughly and documented [4, 5]. They are referred to as the HD and H3 flame. Details of the two flames can be found in Table 1. Both flames are very similar aside from different hydrogen/nitrogen ratios. To give an impression of the studied flames, Fig. 1 shows the flame front of the H3 flame, indicated by the OH-mass fraction.

The turbulent flow field and the chemical processes in the source region are simulated by Large Eddy Simula-

tion (LES). The low mach number of the jet flames allows an incompressible formulation of the LES, which is very efficient. These simulations were done by F. Fleming from the TU Darmstadt. Details of the used LES approach can be found in [3].

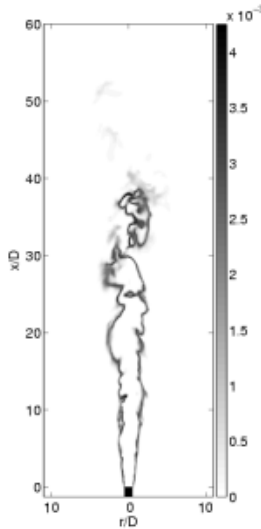


Figure 1: A snapshot of the OH-mass fraction indicating the flame front of the H3 flame, which is one of the studied jet flames

Table 1: Parameters of the studied jet flames

	HD	H3
fuel [vol%]	23/77 H ₂ /N ₂	50/50 H ₂ /N ₂
D [mm]	8 mm	8 mm
U _{bulk} [m/s]	36,3 m/s	34,8 m/s
U _{coflow} [m/s]	0,2 m/s	0,2 m/s
Re	16000	10000
f _{stoic}	0,583	0,310

fuel: hydrogen/nitrogen ratio, D: nozzle diameter, U_{bulk}: flow velocity, U_{coflow}: cowflow velocity, Re : Reynolds number, f_{stoic}: stoichiometric mixture fraction

As output from the model only the velocity field on the Kirchhoff-surface can be used. Due to the incompressible formulation of the LES pressure data could not be obtained.

2.2 The Kirchhoff-Method

The Kirchhoff-Method is based on the coupling of a non-linear source region and a homogeneous acoustical radiation zone via a control surface. The control surface has to enclose all acoustical sources. Beside this, the medium

in the acoustical radiation zone has to be sufficiently free of flow and temperature gradient as required by the homogeneous acoustical wave equation.

From the LES velocity data at sampled time steps are obtained on the control surface. These velocity distributions serve as input data for a boundary element method, which yields the pressure at the control surface. Once velocity and pressure at the control surface are known, the radiated sound power as well as the sound pressure at field points in the radiation zone can be evaluated.

Another Kirchhoff-approach is discussed in [2], where the equivalent source method is applied to the velocity data of the LES. In the present paper the results of the two approaches will be compared without giving a detailed description of the ESM approach.

2.2.1 Coupling LES and BEM

As acoustical data, samples of the flow velocity in a cylindrical domain around the flame were gathered at every s during the LES run. From the spatial distribution of the sampling positions cylindrical surface meshes with increasing radii from $6.7D$ to $13.6D$ could be formed. For the HD-Flame a total number of 1717 velocity samples at every spatial point where collected, for the H3 Flame even longer time signals of 2619 samples for every spatial point where generated. The time signals were transformed into the frequency domain by Fast Fourier Transformation.

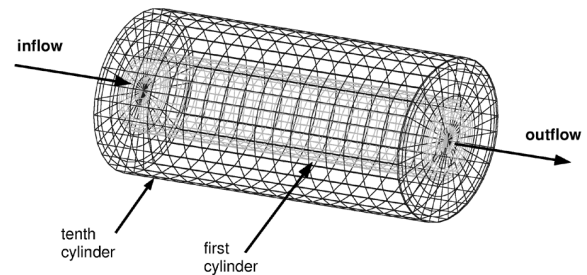


Figure 2: Meshes of the cylindrical Kirchhoff-surface, where the velocity data of the LES were sampled

The complex spectra of the normal velocity at each surface point are the input data for the BE model.

2.3 The BE model

The BE approach is a direct BEM, which solves the Helmholtz-Integral-Equation for exterior problems on the control surface. The surface elements are regarded to be constant.

Since the BEM for the presented Neumann problem does

not have a unique solution at the characteristic eigenfrequencies of the associated interior Dirichlet problem, the CHIEF method was applied to remedy the non-uniqueness at these eigenfrequencies. Ten equidistant CHIEF points at the axis of the cylinders were chosen and tests showed that thus a satisfactory regularisation of the occurring irregular frequencies in the considered frequency range could be achieved. The test method is described in [6, 7].

3 Acoustic measurement

To validate the numerical results, the acoustical sound power of the flames was measured. The radiated sound power was obtained by measuring with an intensity probe around the flames along the surface of a cube with dimensions $1\text{m} \times 1\text{m} \times 1\text{m}$. The intensity was then integrated over all sides.

3.1 Radiated sound power

Beside the sound power of the burning flames also the sound power of the isothermal flow was quantified. The measured sound power levels are shown in Fig. 3. The characteristics of the sound radiation of both flames do not differ much due to the high similarity of the flames. One can conclude that in a wide frequency range the combustion noise level is much higher than the level due to flow noise only. While the flow noise shows some distinct peaks, the reactive flow emits broadband noise, decreasing towards the higher frequency range.

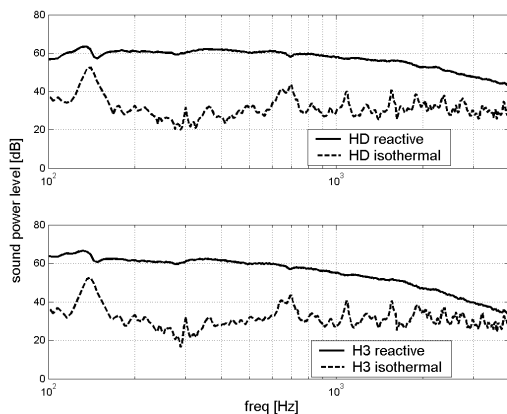


Figure 3: Measured sound power levels of HD and H3 flame for the isothermal and the reactive flow, respectively

3.2 Influence of the Reynolds number

For the H3-flame the flow velocity, which is proportional to the Reynolds number, was varied additionally to have a closer look on the noise generating mechanisms. Fig. 4 shows the respective sound power levels. Assuming an aerodynamical monopole source, the sound power should scale with U_{flow}^4 or Re^4 , respectively. In Fig. 5 the same sound power levels are plotted after normalizing the sound power with respect to the reference Reynolds number of $Re=10000$,

$$Lp_{norm} = Lp - 40 \log_{10}(Re/10000). \quad (1)$$

The results obtained in this way confirm the assumption of monopole characteristics quite well, despite for the lowest Reynolds number where the noise due to the flame is in the order or lower than the noise due to the flow. In this case the tonal parts are especially dominant at higher frequencies.

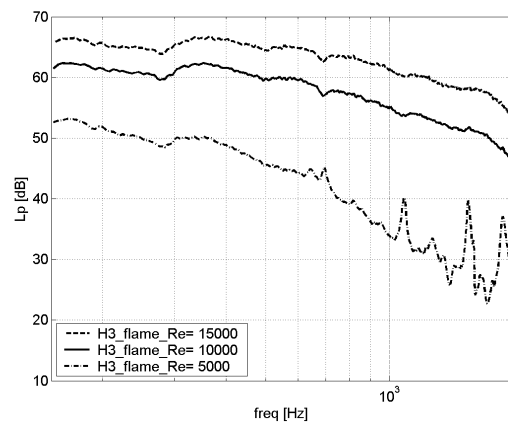


Figure 4: Sound power level of the H3 flame for varying Reynolds numbers

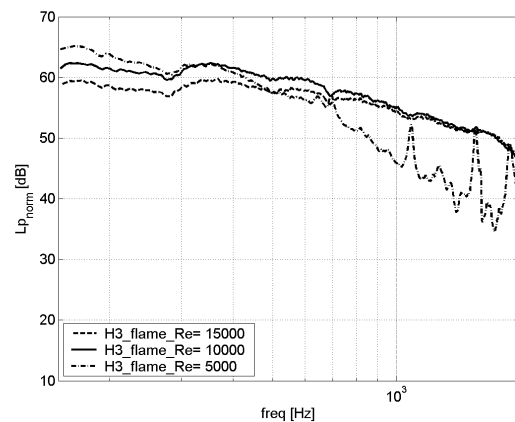


Figure 5: Sound power level of the H3-flame, normalized with respect to $40 \log_{10}(Re/10000)$

A more closely determination of the noise generating mechanisms is beyond the scope of this paper. An attempt to find corresponding equivalent acoustical sources to describe the sound generation of the flames can be found in [2].

4 Simulation results

After obtaining the BEM solution for the pressure distribution p on the control surface, the radiated sound power P of the flames was calculated from this pressure distribution p and the normal velocity v_n , integrated over the control surface S ,

$$P = \frac{1}{2} \int_S \Re\{pv_n^*\} dS. \quad (2)$$

In Fig. 6 and 7 the calculated and measured spectra of sound power level are shown for the two flames. Beside the resulting sound power of the BEM simulation also the results for the sound power calculated with the ESM approach (see [2]) are plotted. Firstly it can be recognized, that both approaches give very similar results. Only in the lower frequency range the deviations can be detected for the HD flame, which may be caused by instabilities of the ESM in this frequency range.

For the HD flame the simulated and the measured sound power are in relative good agreement. The measured sound power is slightly overestimated by the simulations with 3-5 dB. In the higher frequency range above 2000 Hz, the simulated curves do not follow the further decrease of the measured sound power level. In case

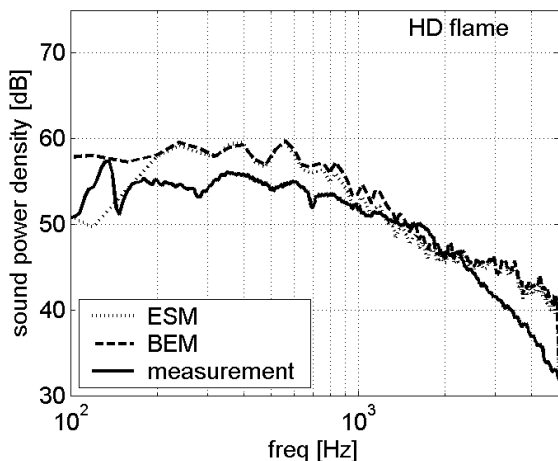


Figure 6: Simulated and measured sound power density level of the HD flame

of the H3 flame this good agreement cannot be found (Fig. 7). The frequency response of the measured and

simulated sound power level deviates much and the measured level is highly overestimated with at least 9 dB. For a further investigation of this deviation the intensity

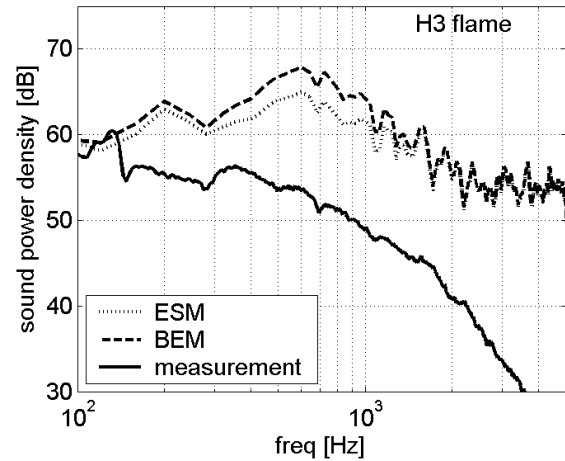


Figure 7: Simulated and measured sound power density level of the H3 flame

level was calculated at some selected measuring points and compared to the measured intensity level at these points. Fig. 8 shows the position of the measuring points P3, P6 and P7; the arrows indicate the direction of the intensity vector. The dashed box represents the location of the Kirchhoff-surface in this setting. In Fig. 9 the mea-

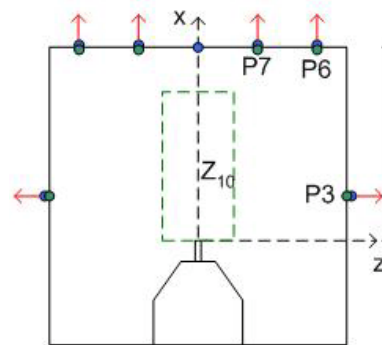


Figure 8: Position of the measuring points P3, P6 and P7

sured and simulated sound intensity level at these points are plotted. Both curves match well for P3 (upper plot). Point P3 has the largest distance from the flame axis as well as the largest distance from the outflow plane of the Kirchhoff-surface. The measured and simulated sound intensity levels at the other two points differ strongly. The difference at point P7, which is located more close to the flame axis, is higher than at point P6. From these evaluations it can be concluded that the velocity field of the outflow plane of the Kirchhoff-surface disturbs the acoustical simulations, especially near the flame axis.

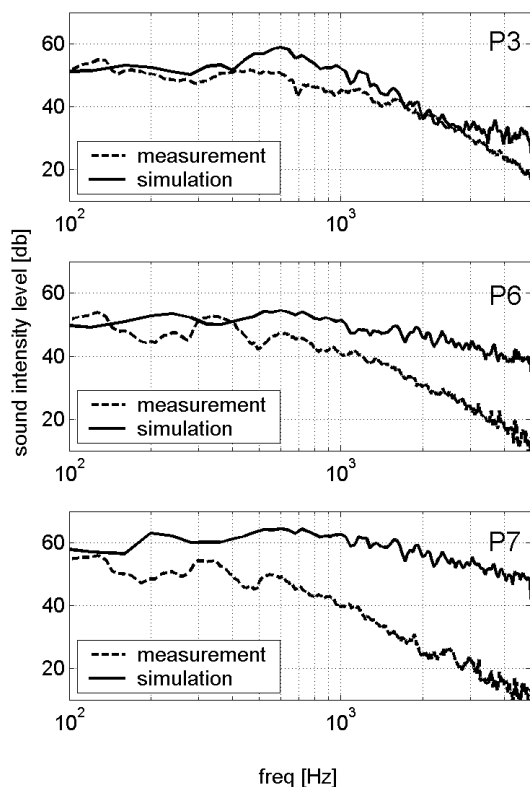


Figure 9: measured and simulated sound intensity level of the H3 flame at the measuring points P3, P6 and P7

5 Conclusions

It could be shown, that the Kirchhoff-method, here realised as a coupling of a incompressible Large Eddy Simulation and a Boundary Element Method, is a powerful tool for the simulation of the noise, generated by open, non-premixed jet flames.

Two different flames were investigated, which differ mainly with respect to their fuel ratio. Regarding the obtained results for the two flames, it can be concluded that for one case (HD) the presented approach is able to predict the sound radiation of open, non-premixed jet flames with high quality. Here, the agreement between calculations and measurement is good over a wide frequency range.

For the second case (H3) the approach fails clearly for the medium and high frequency range. This seems to be mainly due the difference in the field at the outlet of the cylinder. There, the calculated intensity flow was much higher than the one through the sidewalls of the cylinder. This does not agree with measurements of the intensity, since the measured intensity flow through all surfaces is of similar magnitude.

A comparison of the mean density and temperature at the top of the Kirchhoff-surface between the two flames shows lesser variation from the room density and temperature for the HD flame than for the H3 flame. This suggests that the Kirchhoff-surface was probably not large enough for the H3 flame. A new calculation of the H3 flame with a longer cylinder is planned.

Various measurements have been carried out to determine the sound power level of the flames, but also the sound power level of the isothermal flow and for varying Reynolds numbers. Scaling with a typical Reynolds number leads to very similar results for flames with different Reynolds numbers Re , assuming that the sound generation is proportional to Re^4 . This indicates that volume sources due to the combustion processes are responsible for the noise generation.

References

- [1] Combustion Noise Initiative, URL: <http://www.combustion-noise.de>
- [2] R. Piscoya et al., 'Numerical aspects of the Equivalent Source Method applied to combustion noise', *Proc. ICSV12*, Lisbon, Portugal (2005)
- [3] F. Flemming et al., 'A hybrid approach for the evaluation of the radiated noise from a turbulent non-premixed jet flame based on Large Eddy Simulation and equivalent source & boundary element methods', *Proc. ICSV12*, Lisbon, Portugal (2005)
- [4] R. Barlow (ed.), *Proceedings of the TNF Workshop*, Sandia National Laboratories, Livermore, CA, www.ca.sandia.gov/TNF
- [5] M. Tacke, S. Linow, S. Geiss, E. Hassel, J. Janicka, J.-Y. Chen, 'Experimental and numerical study of a highly diluted turbulent diffusion flame close to blowout', *Proc. Combust. Inst.*, 27, 1139-1148 (1998)
- [6] H. Brick, M. Ochmann, E. Brenck, 'Simulation of the sound radiation from wheel-like structures using the boundary element method', *Proc. Forum Acusticum*, Sevilla, (2002)
- [7] M. Ochmann, A. Osetrov, 'Construction of analytical solutions for the error estimation of acoustical boundary element solvers', *Proc. Forum Acusticum*, Sevilla, (2002)

Paper IV

R. Piscoya, H. Brick, M. Ochmann & P. Költzsch.
Equivalent source method and boundary element method for calculating combustion noise. *Acta Acustica united with Acustica*, 94(4):514–527, 2008.

available at:

<http://www.ingentaconnect.com/content/dav/aaua/2008/00000094/00000004/art00002>

Paper V

M. Ochmann & H. Brick.

Acoustical radiation and scattering above an impedance plane.

In S. Marburg and B. Nolte (editors), *Computational Acoustics of Noise Propagation in Fluids. Finite and Boundary Element Methods*. Chapter 17, 459–494, Springer-Verlag, Berlin, 2008.

available at:

<http://www.springerlink.com/content/t4881434501wm424/?p=76e8e9f1fab7498a8a34aa39aa60ee38&pi=0>

Paper VI



A half-space BEM for the simulation of sound propagation above an impedance plane

H. Brick^a and M. Ochmann^b

^aTFH Berlin - University of Applied Sciences, FB II, Mathematics - Physics - Chemistry,
Luxemburger Str. 10, 13353 Berlin, Germany

^bTechnische Fachhochschule Berlin, Univ. of Applied Sciences, Luxemburger Str. 10, 13353
Berlin, Germany
brick@tfh-berlin.de

The Boundary-Element-Method is a powerful tool for the simulation of sound radiation and scattering. Classically, it was developed for the free 3D-space, but it can be modified easily for half-space solutions as long as the half-space is delimited by a perfectly rigid or soft plane. In this case, the Green's function, the core of the BEM, can be derived from a simple image source ansatz, which however cannot be used for a more general impedance boundary condition. In this presentation, an appropriate Green's function will be studied, which is able to describe the sound propagation above an impedance plane and is suitable for an implementation into a BEM code. It bases on the superposition of sound sources with complex source points. The numerical evaluation of this Green's function will be presented along with several test cases. The computational costs of the developed "Complex-Source-Point-BEM" (CBEM) in comparison with a classical BEM together with a discretisation of the impedance plane will be discussed.

1 Introduction

The purpose of the present work is to calculate the sound field, which is radiated by a vibrating structure in presence of an infinite plane, which is characterized by its normal impedance. The boundary element method (BEM) is well suited for the calculation of the sound radiation of complex structures, but the presence of an impedance plane represents a serious difficulty for the application of the BEM. The infinite plane can be approximated by an additional discretized structure. Apart from the low accuracy, which can be gained with this approach, the supplementary structure enlarges the set of equations considerably. Another way is to incorporate an appropriate Green's function into the BEM formulation, which fulfills the boundary conditions on the impedance plane automatically. In literature there can be found numerous solutions for the Green's function describing the sound propagation above an impedance plane, e.g. [1], [2], [3]. Unfortunately, all those solutions have singularities for an impedance with springlike reactance and special source-receiver geometries. They are not suited for an implementation in a BEM code for the simulation of outdoor sound propagation, since most of real ground surfaces show springlike impedance characteristics [4]. Also, in [5], which directly focuses on the BEM, a sufficient solution for this configuration could not be found. Ochmann presented in [6] a Green's function, which seems suitable for an incorporation into a BEM code, since it does not have any limitations considering the impedance characteristics of the plane or the placement of source and receiver. In the following work this Green's function and its implementation in a BEM code will be discussed. At first a brief survey of the theoretical background will be given, followed by details about the numerical implementation of the function. Two test cases will be presented to verify the implementation. The paper concludes with a investigation of the accuracy and effectiveness of the new CBEM formulation in comparison with an indirect BEM and a discretized impedance plane.

2 Theory

The basis for the BEM is the Helmholtz-Integral-Equation (HIE), here for exterior problems,

$$C(\vec{x})p(\vec{x}) = \int_{S_Q} \left(p(\vec{y}) \frac{\partial g(\vec{x}, \vec{y})}{\partial \vec{n}_y} - \frac{\partial p(\vec{y})}{\partial \vec{n}_y} g(\vec{x}, \vec{y}) \right) dS_y \quad (1)$$

with

$$C(\vec{y}) = \begin{cases} 1 & \vec{x} \text{ in the exterior domain,} \\ \frac{1}{2} & \vec{x} \text{ on the surface } S_Q, \\ 0 & \vec{x} \text{ in the interior domain.} \end{cases}$$

The core of the HIE is the Green's function $g(\vec{x}, \vec{y})$. As solution of the wave equation it describes the sound propagation between the source point $\vec{y} = (x_s, y_s, z_s)$ and the receiver point $\vec{x} = (x, y, z)$ and has to fulfill the boundary condition on the surface as well as Sommerfelds radiation condition at infinity. For the free-space case the Greens function is given by

$$g(\vec{x}, \vec{y}) = \frac{e^{-ikR_1}}{4\pi R_1} \quad (2)$$

with $R_1 = \sqrt{(x - x_s)^2 + (y - y_s)^2 + (z - z_s)^2}$. k is the wavenumber $k = \omega/c_0$ with ω as angular frequency and c_0 the speed of sound in the acoustic domain. The time dependence $\exp(i\omega t)$ is omitted.

Regarding a half-space problem, the three-dimensional space is separated by an infinite plane S_p , see Fig. 1. The boundary condition on the plane is given by the plane's normal impedance Z

$$\frac{p}{v_n} = Z \quad \text{on } S_p. \quad (3)$$

As long as the $Z = \infty$ or $Z = 0$, which corresponds to a perfectly rigid and soft plane, respectively, the appropriate Green's function is given by an image source ansatz

$$g(\vec{x}, \vec{y}) = \frac{e^{-ikR_1}}{4\pi R_1} + R_p \frac{e^{-ikR_2}}{4\pi R_2} \quad (4)$$

with

$$R_p = \begin{cases} +1 & Z = \infty, \\ -1 & Z = 0. \end{cases} \quad (5)$$

In [6] a Green's function was presented, which are able to fulfill any impedance boundary condition on the plane S_p and has no restrictions relating to the position of \vec{x} and \vec{y}

$$G(\vec{x}, \vec{y}) = \frac{e^{-ikR_1}}{4\pi R_1} + \frac{e^{-ikR_2}}{4\pi R_2} + \frac{i\gamma}{2\pi} \int_{-\infty}^0 \frac{e^{-ik\sqrt{\rho^2 + (z+z_s+i\zeta)^2}}}{\underbrace{\sqrt{\rho^2 + (z+z_s+i\zeta)^2}}_{\hat{g}(-z_s-i\zeta)}} e^{-i\gamma\zeta} d\zeta, \quad (6)$$

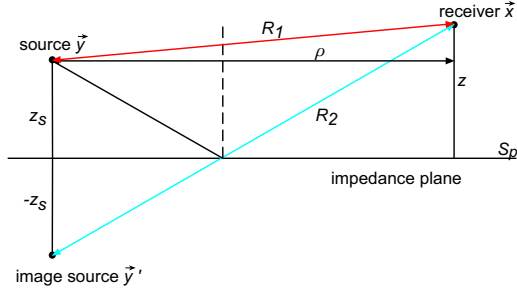


Figure 1: Sketch of source \vec{y} and receiver \vec{x} above an infinite plane

where $\rho = \sqrt{(x - x_s)^2 + (y - y_s)^2}$ is the horizontal distance between \vec{x} and \vec{y} . γ follows from the plane's normalized impedance, $\gamma = ik/Z_0$ mit $Z_0 = Z/(\rho_0 c_0)$ with $\rho_0 c_0$ as impedance of the ambient fluid. The integral in (6) can be interpreted as line integral over image sources with a complex source point, $\hat{g}(-z_s - i\zeta)$. A more detailed presentation of the theoretical background of (6) and its derivation and the characteristics of point sources with complex source points can be found in [6] and [7]. Eq. (6) does not have any singularities, apart from grazing incidence when $z + z_s = 0$, i.e. source and receiver position must not be directly located on the plane. The integral is convergent for masslike and springlike reactive parts of the plane impedance. Its drawback is that it is an improper integral over a fluctuating kernel, which can show a narrow peak at $\zeta = -\rho$.

3 Numerical Evaluation

Due to the difficult kernel in the integral of Eq. (6) an evaluation of the integral can be quite tedious. A very reliable method is the adaptive multigrid quadrature, which is presented in [8]. This quadrature method requires the determination of a lower integration limit. The integrand $\Psi(\zeta)$ can be separated into a decaying envelope $\Psi_E(\zeta)$ and a oscillating term $\Psi_O(\zeta)$

$$\begin{aligned} \Psi(\zeta) &= \frac{e^{-ikr}}{r} e^{-i\gamma\zeta} \\ &= \underbrace{1/|r| e^{(k \operatorname{Im}\{r\} + \operatorname{Im}\{\gamma\}\zeta)}}_{\Psi_E(\zeta)} \underbrace{e^{-i(k \operatorname{Re}\{r\} + \phi + \operatorname{Re}\{\gamma\}\zeta)}}_{\Psi_O(\zeta)} \end{aligned} \quad (7)$$

with $r = \sqrt{\rho^2 + (z + z_s - i\zeta)^2}$. $\operatorname{Re}\{\}$ and $\operatorname{Im}\{\}$ denote the real and imaginary part of the quantity in brackets, respectively. Since $\operatorname{Im}\{\gamma\}$ represents the damping of the ground, $\operatorname{Im}\{\gamma\}$ must be equal or greater than zero and the exponent in $\Psi_E(\zeta)$ is negative for all $\zeta \in (-\infty, 0]$. This decaying envelope ensures the convergence of the integral in (6) on one hand and it provides the possibility of defining a lower limit on the other. We decide to terminate the integration at ζ_l where $\Psi_E(\zeta) < 10^{-6}$. Fig. 2 shows the kernel of the integral and the components of the envelope $\Psi_E(\zeta)$ for $z + z_s \ll 0$, i.e. for \vec{x} and \vec{y} close to the plane. For the implementation of the quadrature algorithm the program package "mlquad" from "CodeLib" was used and the code was adapted to

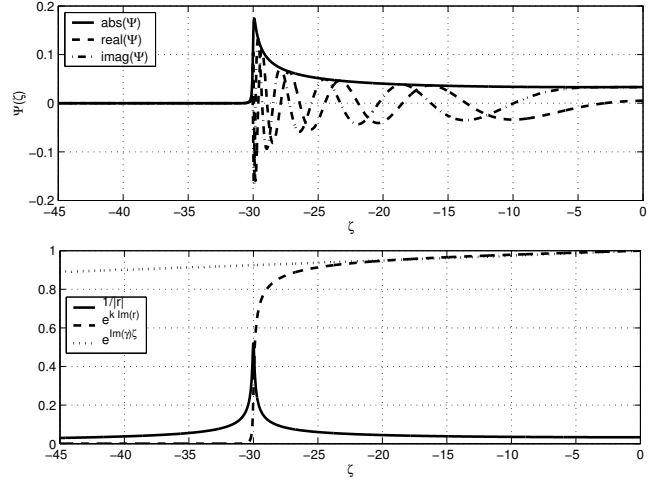


Figure 2: Upper panel: Curve of $\Psi(\zeta)$ in case $z + z_s \ll 1$ for $\rho = 30$ m, $\gamma = 0.0026 + i0.0026$ m $^{-1}$, $z + z_s = 0.06$ m, $k = 1$ m $^{-1}$. Lower panel: Components of the envelope $\Psi_E(\zeta)$.

the present integral. "CodeLib" is a collection of algorithms of the Konrad-Zuse-Zentrum für Informationstechnik Berlin [9].

In case $\operatorname{Im}\{\gamma\} > 1$, the Gauss-Laguerre quadrature can be applied to solve the integral in (6). This leads to an enormous acceleration of the calculation. The Gauss-Laguerre quadrature is defined as

$$\int_0^\infty f(\eta) e^{-\eta} d\eta = \sum_{i=1}^n w(i) f(\eta(i)). \quad (8)$$

By means of a variable transformation with $\eta = -\zeta \operatorname{Im}\{\gamma\}$ the integral in (6) can be converted into the appropriate form,

$$I = \frac{i\gamma}{2\pi \operatorname{Im}\{\gamma\}} \int_0^\infty \underbrace{\frac{e^{-ik\tilde{r}}}{\tilde{r}} e^{i\eta \operatorname{Re}\{\gamma\}/\operatorname{Im}\{\gamma\}} e^{-\eta}}_{f(\eta)} d\eta \quad (9)$$

with $\tilde{r} = \sqrt{\rho^2 + (z + z_s - i\eta/\operatorname{Im}\{\gamma\})^2}$. The number of quadrature points n depends on the curve of the integral kernel. Our investigations showed, that the sum of the heights of source and receiver location has the most influence on the necessary number n . The closer source and receiver are located to the plane, the more quadrature points are necessary to solve the integral correctly.

The expression for $f(\eta)$ contains also an exponentially decaying term, namely $\exp(k \operatorname{Im}\{\tilde{r}\})$. In case the decay of the term $\exp(k \operatorname{Im}\{\tilde{r}\})$ is considerably more steep as the decay of $\exp(-\eta)$, the integral can not be solved by the Gauss-Laguerre quadrature. From this it follows that this quadrature formula can only be applied for $\operatorname{Im}\{\gamma\} > 1$. However, in this case the Gauss-Laguerre quadrature is observed to solve the integral correctly and very fast. A resistance of $\operatorname{Im}\{\gamma\} > 1$ can be found for soft grounds in the higher frequency range.

4 Test cases

4.1 Soft ground

The test configuration is given by a small cube with edge length of 1 m, whose surface is driven by a virtual monopole source in its center [10], [11]. The surface mesh consists of 54 four-noded quadrilateral elements. The center of the cube is located 3 m above the infinite impedance plane, which is located in $z = 0$, see Fig. 3. The perfectly soft plane impedance is approximated by a very high admittance of $|\gamma| = \sqrt{2} \cdot 10^{-3}$. Both a masslike ($\text{Re}\{\gamma\} > 0$) and a springlike ($\text{Re}\{\gamma\} < 0$) plane impedance are investigated. Fig. 3 shows the BEM results for the sound pressure in field points in a distance of 3 m around the center of the cube, see Fig. 3, for the image-source Green's function BEM (IMBEM), Eq. (4), and the complex Green's function BEM (CBEM), Eq. (6). The sound pressure was normalized to $\rho_0 c |\bar{v}_n|$, with $|\bar{v}_n|$ as absolute value of the mean surface velocity of the pulsating object. For the illustrated benchmark configuration the results of the CBEM formulation match very well the results of the IMBEM.

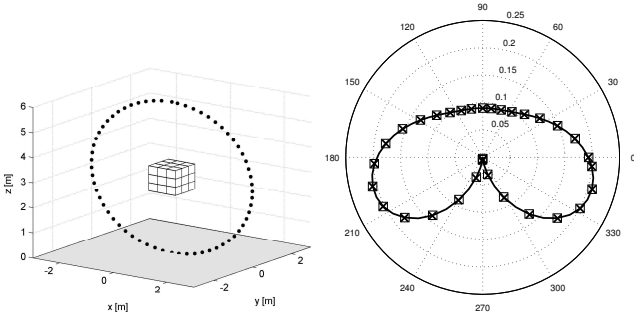


Figure 3: *Left panel:* Test geometry: Field points around the radiating cube above an impedance plane.

Right panel: Normalized sound pressure in the field points: — calculated with IMBEM in case of a perfectly soft plane ($R_p = -1$); \square calculated with the CBEM for a soft plane with masslike impedance ($\gamma = 10^3 + i10^3 \text{ m}^{-1}$) and \times for a soft plane with springlike impedance ($\gamma = -10^3 + i10^3 \text{ m}^{-1}$)

4.2 Perpendicular incidence

In case, source and receiver are arranged one above the other on a vertical axis ($\rho = 0$), there exists a exact solution for Eq. (6)

$$G_{\text{exakt}}(\vec{x}, \vec{y}) = \frac{e^{-ikR_1}}{4\pi R_1} + \frac{e^{-ikR_2}}{4\pi R_2} - \frac{ik}{2\pi Z_0} e^{ik(z+z_s)/Z_0} E_1 \left(ik(z+z_s) \left(1 + \frac{1}{Z_0} \right) \right). \quad (10)$$

For field points far above the impedance plane, where $k(z+z_s)$ is large, Eq. (10) can be simplified to a "plane wave"-approximation [12]

$$G_{\text{plane}}(\vec{x}, \vec{y}) = \frac{e^{-ikR_1}}{4\pi R_1} + \frac{Z_0 - 1}{Z_0 + 1} \frac{e^{-ikR_2}}{4\pi R_2}. \quad (11)$$

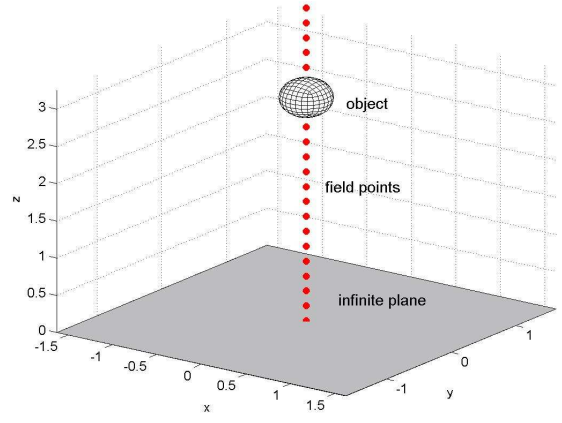


Figure 4: Vibrating sphere above an impedance plane, the field points are located on a vertical line at

$$\vec{x}_{\text{FP}} = (0, 0, z)$$

The geometry of the test configuration can be seen in Fig. 4. A sphere of radius 0.25 m is located above an impedance plane with $\gamma = 1 + 0.5i$. The sphere's center is located at $(0, 0, 3\text{m})$, the wave number is $k = 1 \text{ m}^{-1}$. The sphere's surface is build up by 296 quadrilateral and triangular elements. The field points are arranged on a vertical line below and above the sphere's center at $\vec{x}_{\text{FP}} = (0, 0, z)$. The sphere vibrates with a normal velocity distribution, which is determined by a virtual monopole source in the center of the sphere at \vec{y} . Due to the presence of the impedance plane the velocity v_n is not uniform, but can be obtained by means of Eq. (6). Thus, the normal velocity v_n of the nodes \vec{x} of the sphere are given by

$$v_n(\vec{x}) = \frac{i}{\omega \rho_0} A_p \frac{\partial G(\vec{x}, \vec{y})}{\partial \vec{n}_x}. \quad (12)$$

A_p is the source strength of the virtual monopole source in the interior of the sphere.

From Gl. (10) follows the exact sound pressure at the field points p_{exact} . The error E is a measure for the deviation of the field point sound pressure from the exact solution

$$E_i = \sqrt{\frac{|p_i - p_{\text{exact}}|^2}{|p_{\text{exact}}|^2}}, \quad (13)$$

with p_i as sound pressure at the field points coming from the "plane wave"-approximation and the CBEM-solution. Fig. 5 shows the error curves. The error of the monopole test E_{disc} is additionally plotted. E_{disc} represents the general discretization error of the numerical solution, as it was described in [10]. It can be seen, that the error of the CBEM-solution E_{CBEM} is in the order of magnitude of the discretization error at around 1%. As expected, the error of the "plane wave"-approximation is very high for field points in proximity to the plane. For field points at larger z , the error decreases and the approximation converges to the exact solution. This test verifies the implementation of the Green's function (6) into the BEM-application and shows, that the CBEM is able to approximate excellently the radiated sound field above an impedance plane.

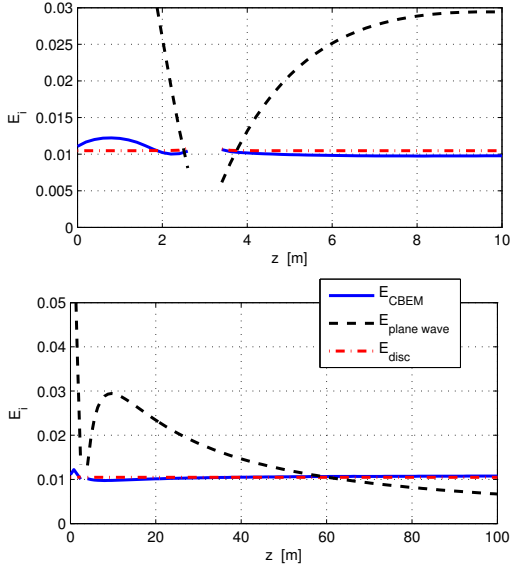


Figure 5: Error E of the "plane wave"-approximation and of CBEM-solution as well as the discretization error

5 Application of the CBEM

In a first step we investigate the accuracy of the the multigrid quadrature and the Gauss-Laguerre quadrature within a CBEM simulation and later on we compare the CBEM results to results of an indirect BEM, where the infinite impedance plane is represented by a discretized plane model.

The geometrical configuration can be found in Fig. 6. The center of the vibrating sphere, which was already introduced in Sec. 4.2, is now located at $(0, 0, 1\text{m})$ above the impedance plane with $\gamma = -1.41 + i1.66$ at $f = 400$ Hz (forest floor). 100 field points are located on a horizontal line at $\vec{x}_{\text{FP}} = ([0.5 : 300]\text{m}, 0, 1\text{m})$. Fig. 7

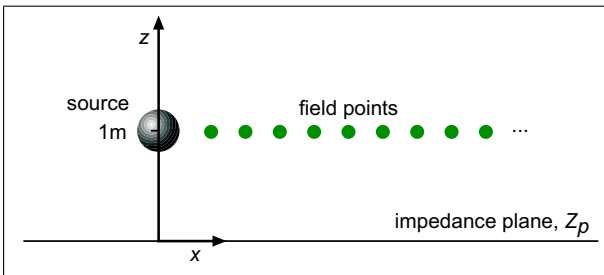


Figure 6: Vibrating sphere above an impedance plane, the field points are located on a horizontal line at $\vec{x}_{\text{FP}} = (x, 0, 1\text{m})$

shows the error E , Eq. (13), of the CBEM-solution for this configuration calculated with the multigrid quadrature $E_{\text{CBEM-mlquad}}$ and the Gauss-Laguerre quadrature $E_{\text{CBEM-GL}}$, respectively. Here, p_{exact} is the field points pressure, calculated with Eq. (6) by means of a multigrid quadrature of the integral term. The discretization error E_{disc} is additionally plotted. Again, the error of both CBEM-solutions, $E_{\text{CBEM-GL}}$ and $E_{\text{CBEM-mlquad}}$, is in the order of magnitude of the discretization error of 2.5 % over a wide range of the horizontal distance x .

At very far distances, for $kx > 400$ some peak-shaped deviations from this error level occur. The cause of this deviations could not be ascertained so far. It seems, that there occur numerical instabilities for some selected geometrical configurations, provided that the field points are very far away from the source.

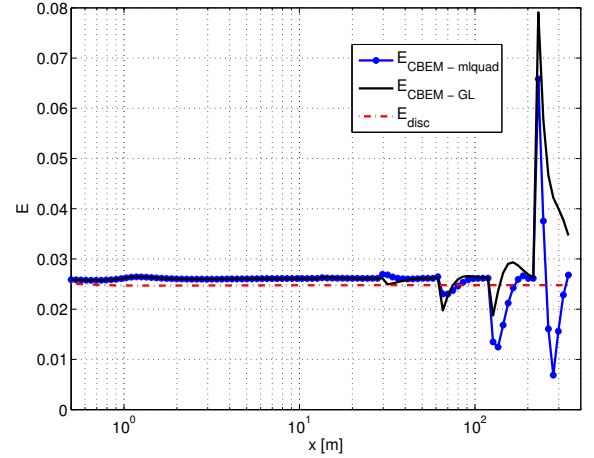


Figure 7: Error of the CBEM-solution with multigrid quadrature $E_{\text{CBEM-mlquad}}$ and with Gauss-Laguerre quadrature $E_{\text{CBEM-GL}}$ as well as the discretization error E_{disc}

In the next step, the impedance plane in Fig. 6 is represented by a set of planar quadrilateral elements, see Fig. 8. We investigate two measures of the discretized plane, 6×6 m with 2304 elements and 12×12 m with 9216 elements. Since the plane does not have a closed surface the indirect BEM has been used. The calculation was carried out with LMS Virtual.Lab Rev.7B. Fig. 9 shows the error of the field points pressure for the two planes in comparison with the previously discussed $E_{\text{CBEM-GL}}$. It can be clearly seen, that outside the discretized plane areas the error becomes huge (the edges of the planes are indicated by the arrows, labeled with 3m and 6m). With increasing x the sound field becomes more and more the sound field of an monopole source in free space, therefore the enormous deviations from the exact solution occur at the outlying field points. But also at the field points above the plane model a large error is detected, even near the middle of the planes. The increased edge length of the greater plane does not enhance the results much. The error curves show, that the CBEM simulates the radiated sound field above an impedance plane with a very high grade of accuracy, which can not be reached by using a discretized plane model. The cost for the different simulation approaches

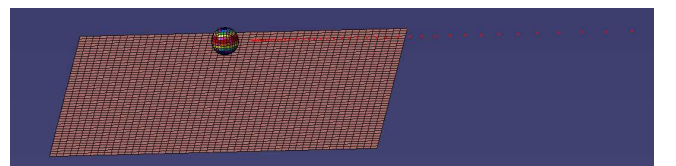


Figure 8: Vibrating sphere above a discretized impedance plane

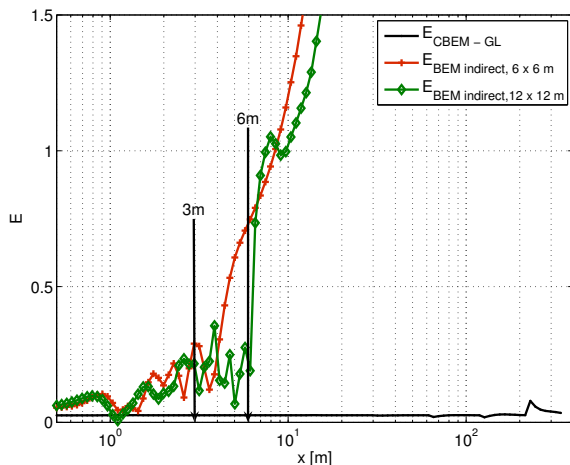


Figure 9: Error of the sound pressure at the field points for the different simulations

can be found in Tab. 1. All calculations were done on a desktop PC with Intel Pentium D Dualcore, running at 3.20 GHz, equipped with 2.00 GB RAM, OS Windows XP. BEMLAB is our in-house Matlab-based BEM code, described in [7], [13]. The multigrid quadrature

Method	Software	Time needed
CBEM-mlquad	BEMLAB	4 h
CBEM-GL	BEMLAB	0.5 min
indirect BEM, 6×6 m	Virtual.Lab	5 min
indirect BEM, 12×12 m	Virtual.Lab	1.5 h

Table 1: Costs for the different simulation methods

(CBEM-mlquad) of the integral term of Eq. (6) has comparatively high costs. At present the CBEM in combination with a Gauss-Laguerre quadrature (CBEM-GL) is the most favorable approach regarding quality and speed of the BEM-calculation.

6 Summary

A Green's function, which describes the sound propagation above an impedance plane, was successfully implemented in a BEM-code. Due to the characteristics of the Greens' function there does not exist any limitation for the applicability of the resulting CBEM. Hence, the impedance planes are allowed with masslike as well as springlike reactive parts. All arrangements of source and receiver points are possible. It could be shown, that the quality of the CBEM-solution is much higher than of a comparable indirect BEM-model. Thus, the presented CBEM represents a very valuable extension of the classical BEM-formulation for the description of more realistic models considering outdoor sound propagation.

References

- [1] K. Attenborough, S. I. Hayek, and J. M. Lawther. Propagation of sound above a porous half-space. *J. Acoust. Soc. Am.*, 68(5):1493–1501, 1980.
- [2] S-I. Thomasson. Asymptotic solution for sound propagation above an impedance boundary. *Acustica*, 45:122–125, 1980.
- [3] D. Habault and P. J. T. Filippi. Ground effect analysis: Surface wave and layer potential representations. *Journal of Sound and Vibration*, 79(4):529–550, 1981.
- [4] M. Ögren and H. Jonasson. *Measurement of the Acoustic Impedance of Ground*. SP Swedisch National Testing and Research Institut, SP Report 1998:28, 1998.
- [5] W. L. Li, T. W. Wu, and A. F. Seybert. A half-space boundary element method for acoustic problems with a reflecting plane of arbitrary impedance. *Journal of Sound and Vibration*, 171(2):173–184, 1994.
- [6] M. Ochmann. The complex equivalent source method for sound propagation over an impedance plane. *J. Acoust. Soc. Am.*, 116(6):3304–3311, 2004.
- [7] M. Ochmann and H. Brick. Acoustical radiation and scattering above an impedance plane. In S. Marburg and B. Nolte, editors, *Computational Acoustics of Noise Propagation in Fluids. Finite and Boundary Element Methods*, chapter 17, pages 459–494. Springer Verlag, Berlin, 2008.
- [8] P. Deuffhard and A. Hohmann. *Numerische Mathematik I - Eine algorithmisch orientierte Einführung*, chapter 9.7, pages 343–351. de Gruyter, Berlin, New York, 1993.
- [9] P. Deuffhard and A. Hohmann. Numerical analysis and modelling—CodeLib. <http://www.zib.de/Numerik/numsoft/CodeLib>.
- [10] M. Ochmann and A. V. Osetrov. Construction of analytical solutions for the error estimation of acoustical boundary element solvers. In *Proc. of the Forum Acusticum*, pages 1000–1004, Sevilla, 2002.
- [11] A. V. Osetrov and M. Ochmann. A fast and stable numerical solution for acoustic boundary element method equations combined with the Burton and Miller method for models consisting of constant elements. *Journal of Computational Acoustics*, 13(1):1–20, 2005.
- [12] M. A. Nobile and S. I. Hayek. Acoustic propagation over an impedance plane. *J. Acoust. Soc. Am.*, 78(4):1325–1336, 1985.
- [13] H. Brick, M. Ochmann, and E. Brenck. Simulation of the sound radiation from wheel-like structures using the boundary element method. *Forum Acusticum, Sevilla*, 2002.